KU LEUVEN

ARENBERG DOCTORAL SCHOOL
Faculty of Engineering Science

Flexible Piezoelectric Micromachined Ultrasound Transducers (PMUTs) towards Imaging Applications

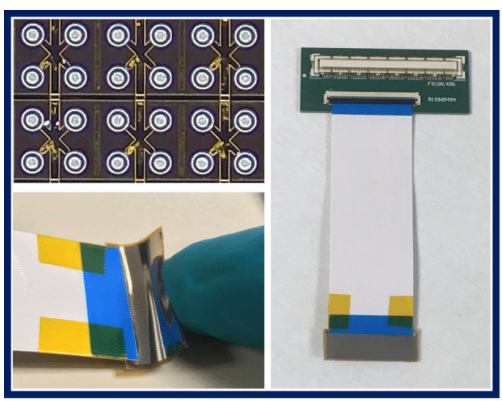

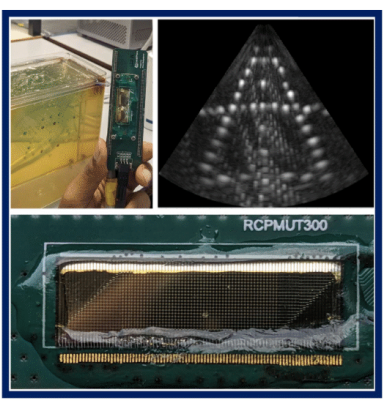

Sanjog Vilas Joshi

Supervisors:
Prof. dr. Michael Kraft
dr. Sina Sadeghpour

Dissertation presented in partial fulfillment of the requirements for the degree of Doctor of Engineering Science (PhD): Electrical Engineering

December 2024

Flexible Piezoelectric Micromachined Ultrasound Transducers (PMUTs) towards Imaging Applications

Sanjog Vilas JOSHI

Examination committee:
Prof. dr. Adhemar Bultheel, chair
Prof. dr. Michael Kraft, supervisor
dr. Sina Sadeghpour, supervisor
Prof. dr. Filip Tavernier
Prof. dr. Ingrid De Wolf
Prof. dr. Jan D'hooge
Prof. dr. Ashwin Seshia
(University of Cambridge)

Dissertation presented in partial fulfillment of the requirements for the degree of Doctor of Engineering Science (PhD): Electrical Engineering

December 2024

© 2024 KU Leuven – Faculty of Engineering Science
Uitgegeven in eigen beheer, Sanjog Vilas Joshi, Celestijnenlaan 200A box 2402, B-3001 Leuven (Belgium)

Alle rechten voorbehouden. Niets uit deze uitgave mag worden vermenigvuldigd en/of openbaar gemaakt worden door middel van druk, fotokopie, microfilm, elektronisch of op welke andere wijze ook zonder voorafgaande schriftelijke toestemming van de uitgever.

All rights reserved. No part of the publication may be reproduced in any form by print, photoprint, microfilm, electronic or any other means without written permission from the publisher.

Preface

The journey of completing this Ph.D. thesis has been one of the most challenging and rewarding experiences of my academic career. It is with great pleasure that I present this work on the development of flexible PMUTs, a MEMS device.

MEMS, or Micro-Electro-Mechanical Systems, are extremely tiny devices that combine mechanical structures and electrical circuits to perform various tasks. One can think of them as mini robots that can sense things like movement, pressure, or temperature and can also move tiny parts. Accelerometers, used in smartphones to detect screen orientation, and gyroscopes, used in drones and gaming controllers to sense rotation are the typical MEMS devices, we all know. PMUT stands for Piezoelectric Micromachined Ultrasonic Transducer. It is a MEMS device that can send and receive ultrasound waves, similar to how a speaker can produce sound and a microphone can capture sound. Just this sound is non-audible, that is why is called ultrasound. A flexible PMUT is simply a version of this device that can bend or flex, unlike traditional rigid ones. Imagine a very thin, bendable material with special properties that allow it to produce and detect ultrasound waves even when it's not flat or straight. The device can be used for medical sensors that can nicely conform to the body, providing more accurate readings and being more comfortable for patients. Also, there is a possibility to use the device to do ultrasound imaging, imagine a sonography machine turned into a patch mounted on a body which provides real-time images. At the heart of this device, there consists about a micron-thick piezo-electric thin film. Piezo-electrics are a special class of materials that can change shape when an electric voltage is applied to it. Conversely, it can generate an electric voltage when it is squeezed or stretched. The word micromachining refers to the process of creating extremely small mechanical structures, such as circular or square shapes on the surface or trenches or pillars inside the material. It's like miniaturizing machines so tiny that they can fit on a chip, like the ones in the phone or computer. This micromachining process to fabricate flexible PMUTs has been carried out on a silicon wafer using lithography techniques. Silicon wafers are thin, flat discs made from silicon,

which is a common material found in sand. These wafers are the foundation on or in which the tiny structures are created. Again, one can think of them as blank canvases that will be turned into works of art using the lithography technique. Lithography simply means patterning and is a bit like printing or photography but on a microscopic scale. During lithography, a light-sensitive material called photoresist is applied to the silicon wafer. A pattern is projected onto the wafer using light, similar to how an image is projected onto a screen. The light changes the properties of the photoresist wherever it hits. The wafer is then washed in a special solution, called a developer, which removes either the exposed or unexposed photoresist, leaving behind a microscopic pattern on the wafer. All these processes are done inside a cleanroom. A cleanroom is a specially designed room where the air is extremely clean. Imagine a place where there's almost no dust or dirt floating around. This is crucial because even a dust particle can ruin the microscopic components being made. I hope this background is clear and interests you to delve deeper into this research endeavor.

The motivation for this research stems from some of the work carried out during my master's on wearables and MEMS. During the last year of my master's, I made the decision to pursue doctoral studies in the area of MEMS. Although I had little to no understanding of what PMUT is, I found the flexible PMUT on SOI safer fabricated by Sina quite interesting. I am quoting here a few lines from the email I wrote to Michael for the PhD position. "The reason why I am attempting to write this email is that I am very much interested in your research. I came across your recent publication 'Bendable Piezoelectric Micromachined Ultrasound Transducer (PMUT) Arrays Based on Silicon-On-Insulator (SOI) Technology' and was intrigued by the design and SOI-based fabrication approach using silicon springs to realize conformal array device. In your research group, I would also love to learn about microelectrode arrays, MEMS devices, and sensors." Thanks to Michael and Sina, I was lucky enough to have offered the topic for the PhD to be 'flexible PMUTs' with the challenge of performing ultrasound imaging with the developed technology for the first time. Although I do not think that I have reached the destination, the journey has been and will be enjoyable.

The completion of this thesis would not have been possible without the support and encouragement of many individuals. First and foremost, I would like to express my deepest gratitude to my advisor, Prof. Michael Kraft. His calm demeanor and the freedom he provided allowed me to explore and grow independently, fostering a sense of confidence in my work. Prof. Kraft consistently facilitates and promotes interaction with colleagues. Moreover, I enjoyed being a part of an international and diverse research group. This environment of collaboration and inclusivity has been instrumental in shaping

this research and my development. Beyond just technical guidance, he helped refine my papers and presentations, meticulously pointing out minor mistakes such as extra spaces and inconsistencies. His leadership, characterized by trust, empowerment, and attention to detail, has truly made a difference.

Secondly, I would also like to extend my heartfelt thanks to my co-supervisor, Dr. Sina Sadeghpour, whose technical guidance and collaboration were invaluable. Sina's extensive knowledge across disciplines such as electrical, materials, and mechanical engineering greatly enriched this work. His assistance with facilities he developed since his PhD and for the Lucidwave meant I did not have to spend extra time on setup, allowing me to focus on improving and fabricating innovative devices. Sina's expertise and clear directions ensured the Ph.D. journey went smoothly, and his enthusiasm for this subject was a constant source of motivation for me. Always just a message away for any technical difficulty or for paper review with stringent deadlines, Sina's involvement was irreplaceable to the success of this research.

I am also profoundly grateful to the members of my dissertation committee. Starting with the accessors, I thank Prof. Filip Tavernier and Prof. Ingrid De Wolf for providing valuable feedback on my work. Also a big thanks to the other members of the committee, jury member, Prof. Jan D'hooge, who also guided me in the ID-N collaboration project on knee assessment with PMUTs. His knowledge depth along with positivity, and inventiveness during our monthly meetings have made a significant impact on my work. Prof. Ashwin Seshia, external jury member, thank you for thoroughly reading my thesis manuscript and providing constructive feedback. I am fortunate to have a jury member from my alma mater, IITB. Thank you Prof. Adhemar Bultheel for being the chairperson of my jury and for guiding my defences.

To my colleagues at the MNS group, thank you for creating an enjoyable work environment where helping each other is considered self-evident. I want to thank in particular Michel, Frederik, and Thomas, you have been always there for technical support when it comes to cleanroom equipment. Your knowledge of fabrication and instrumentation has enabled many parts of the research in my thesis. I would also like to particularly thank Rudi and Donald from MICAS group, for wire-bonding challenging (imperfect) chips. Aojie, Milad, and Kinga, thanks for training sessions and being always available for help with the tools, simulations, and so on. Chen and Nadia, thanks for your input on my writing. Rui, and Yangyang, kudos to our collaborations. Maria, and Mitty, thanks for being amazing officemates. Momina, we all are fortunate to have you in our group. You are always available for relaxing long chats, and on a serious note, Madhavi and I found a close friend in Leuven. Chenxin, Chenxi, Catarina, Bernardo, Filippo, Batist, Masoumeh, Linlin, and Xinyu, thank you for your companionship and support throughout this journey. I have

truly enjoyed working, learning, and growing alongside you.

I owe a special debt of gratitude to my wife who has most closely seen my journey since we were teens and since then, has been a partner in my ups and downs. Without her constructive support, on and off the work field, the PhD would not have been possible. You are also the reason for whatever disciplines I have and came in handy for PhD and still inculcating many more incredible qualities from you, in the coming years of this life journey. It is worth mentioning that she graciously took the time to rehearse my important presentations with me. Special gratitude goes to my parents and elder brother for their invaluable guidance in shaping my academic pursuits during my childhood to high school years and in later years, for their unwavering trust and support in allowing me to choose this career path. I would like to mention that, while I wrote my thesis, they were in Belgium and also our workload at the house was much more relaxed. Just after finishing my first draft of the thesis, I had a European highlights trip with my in-laws and also parents and it was a nice gift for the efforts of the first draft. I thank my in-laws for this comforting retreat and without them, such a plan would not have existed. My entire family's unconditional love, encouragement, and patience, belief in my abilities have been a constant source of motivation, and their support has been invaluable in helping me navigate the challenges of this journey. Also my friends and music community around Leuven, and my tabla (One of the integral percussion instruments played in India and around) teacher from Mumbai, Shri. Rashmin Bhagwat had a significant role in relieving stress levels and helped to revive me through Indian classical music and allied genres.

Finally, I would like to acknowledge the funding and support provided by ID-N and the Lucidwave project from KU Leuven, without which this research would not have been possible. Also, their support and collaborators' inputs and feedback have allowed me to pursue my academic goals and keep the PhD on the right track.

In presenting this thesis, I hope that it not only contributes to the academic community but also inspires future research in this area. The process of experimentation, discovery, and learning has been immensely fulfilling, and I am excited to share the outcomes of this endeavor.

Use of Generative AI

I did use the generative AI assistance tools, namely, ChatGPT

***Generative AI* was used for short-form input assistance**. Apart from language assistance to improve readability in some instances in the thesis, ChatGPT was used as a communication aid to explain some of the terms highly fundamental to my PhD research area, such as MEMS, ultrasound, cleanroom, etc. in simplified terms for better introductory accessibility for non-specialists. After substantial editing, these explanations were incorporated into the preface.

The text/code/ images in this thesis are my own (unless otherwise specified) and generative AI has only been used in accordance with the KU Leuven guidelines and appropriate references have been added. I have reviewed and edited the content as needed and I take full responsibility for the content of the thesis.

Abstract

This dissertation discusses the design and fabrication of polyimide membrane-based flexible as well as rigid PMUT technology. The 2D arrays are developed towards ultrasound imaging applications to establish proof of concept.

Ultrasound technology has shown remarkable benefits in the bio-medical field and healthcare, aiding diagnostics and disease prevention. One area where it has proven highly valuable is medical imaging based on rigid ultrasound probes typically working with thickness mode piezoelectric vibration. However, they face performance limitations arising mainly from associated fabrication techniques, for instance, mechanical dicing limits the interelement pitch. This has given rise to micromachined alternatives, namely piezoelectric micromachined ultrasound transducer (PMUT) with a piezoelectric thin film in flexural mode and capacitive micromachined ultrasound transducer (CMUT) also in the flexural mode with electrostatic forces. MUTs benefit from a small form factor, reduced power consumption, batch fabrication, and the possibility of CMOS integration.

In parallel, plenty of applications have also paved the way for the advancement of flexible ultrasound transducers. Flexible ultrasound transducers broaden the application areas of ultrasonic medical imaging by providing 1) conformal contact to the skin, 2) user-friendliness with an opportunity for continuous monitoring and reduced operator variability, and 3) increased angular coverage compared to rigid planar transducer probes with the possibility of power efficient mechanical focusing. Considering these advantages, the PhD project aimed at developing a flexible PMUT array device towards imaging applications as the area is an unexplored territory in the modern history of flexible PMUTS.

The developed technology obviates the need for expensive silicon-on-insulator (SOI) wafers. The SOI-free process and a custom-made lead-zirconate-titanate (PZT) solution for depositing PZT thin films have resulted in low-cost fabrication. A custom-made PZT solution is prepared in 0.4 M concentration in a methanol solvent, with 15% excess lead, and 0.05 gm Polyvinylpyrrolidone (PVP) polymer, a porogen, per millimole (mM) of PZT. About 0.8-2 µm thick PZT thin film is deposited by the sol-gel process. The film is characterized using X-ray diffraction (XRD) and Double Beam Laser Interferometer (DBLI) methods. 1 µm film has [111] orientation, 60 pm/V d_{33} and 4 C/m^2 e_{31} respectively.

After piezoelectric characterization, the rigid PMUTs are fabricated by deposition of polyimide membrane passive layer and etching cavities to realize membranes. The cavities are etched in silicon for rigid PMUTs. For flexible PMUTs, the cavities are in polyimide for which thicker multistep polyimide deposition is followed and an additional release step is performed. A fabrication process flow is developed starting with common fabrication steps which are adapted to realize rigid as well as flexible devices with slight modification. The PMUT cells have 5-14 µm thick polyimide membranes in total including active layers. The membranes have 100-160 µm diameter. Initially, a small fully addressed array is fabricated to prove the fabrication concept. Later, the fabrication strategy is extended to a row-column (RC) addressed PMUT with a larger aperture.

The fabrication processes have enabled the realization of novel 2D array designs with a pitch ranging from 500 µm to as low as 300 µm for ultrasound imaging applications. The polyimide-membrane-based rigid and flexible arrays are aimed at around 1.5 MHz operation frequency in water medium to counter lower expected sensitivities by lower medium attenuation at lower frequencies. For comparison, an RC-addressed array is also fabricated on an SOI substrate aimed at around 5 MHz in water. The resonance frequencies in-air for rigid and flexible arrays with polyimide membranes are around 3 MHz and 2 MHz, respectively. Surprisingly, the rigid PMUTs with polyimide resulted in a very similar in-air sensitivity of around 0.5 m/s/V as the one with silicon membrane on an SOI substrate. Just the frequency of the SOI-based array is about 6.7 MHz in air (4.2 MHz in water) with the same 100 µm membrane size as that of polyimide. The sensitivity of flexible PMUT in-air is however about 25-fold lower and about 20 mm/s/V. The sensitivities are measured always with a 5V DC bias which enhances the performance. Underwater, the sensitivity of flexible devices is around 3-fold lower than that of rigid ones (not 25-fold lower). To give some numbers, per channel, rigid devices generated 400 Pa/V at 5 mm whereas flexible ones generated about 120 Pa/V. The 10 dB difference has turned out to be a limitation for imaging with flexible PMUTs. The acoustic pressures more or less follow an inverse relation with distance.

The rigid arrays are wire-bonded to custom-made printed circuit boards (PCBs) whereas the flexible ones are integrated with PCB using a flexible flat cable (FFC) which is connected to the array using anisotropic conductive glue. The arrays are connected to the Verasonics transceiver using adapters and connectors on custom-made PCBS. Moreover, To make the arrays applicable for imaging, waterproof sealing is achieved using polyimide and epoxies for rigid PMUTs. Parylene-C is used as an encapsulation material on flexible PMUTs. Rows of the RC-addressed arrays are grounded to use it as a linear array. Ultrasound images of metal wire as well as tissue-mimicking phantoms are captured using the rigid RC PMUT arrays at voltages as low as $10V_{DC} + 10V_{AC}$.

Beknopte samenvatting

In dit proefschrift worden het ontwerp en de fabricage van flexibele en rigide PMUT-technologie op basis van polyimidemembranen besproken. De 2D-arrays zijn ontwikkeld voor de toepassing van echografie om een bewijs van concept te leveren.

Echografietechnologie heeft opmerkelijke voordelen laten zien in het biomedische veld en de gezondheidszorg, en helpt bij diagnostiek en ziektepreventie. Een specifiek gebied waar het zeer waardevol is gebleken, is medische beeldvorming die is gebaseerd op rigide echografiesondes die doorgaans werken met diktemodus-piëzo-elektrische trillingen. Ze hebben echter te maken met prestatiebeperkingen die voornamelijk voortkomen uit bijbehorende fabricagetechnieken, bijvoorbeeld beperkt mechanisch snijden de interelement-pitch. Dit heeft geleid tot microgefreesde alternatieven, namelijk piëzo-elektrische microgefreesde echografietransducer (PMUT) met een piëzo-elektrische dunne film in flexurale modus en capacitieve microgefreesde echografietransducer (CMUT) ook in de flexurale modus met elektrostatische krachten. MUT's profiteren van een kleine vormfactor, lager stroomverbruik, batchfabricage en de mogelijkheid van CMOS-integratie.

Tegelijkertijd hebben tal van toepassingen ook de weg vrijgemaakt voor de vooruitgang van flexibele echografietransducers. Flexibele ultrasone transducers verbreden de toepassingsgebieden van ultrasone medische beeldvorming door 1) conform contact met de huid, 2) gebruiksvriendelijkheid met een mogelijkheid voor continue bewaking en verminderde operatorvariabiliteit, en 3) verhoogde hoekdekking in vergelijking met rigide planaire transducersondes met de mogelijkheid van energiezuinige mechanische focussering. Gezien deze voordelen was het PhD-project gericht op de ontwikkeling van een flexibel PMUT-arrayapparaat voor beeldvormingstoepassingen, aangezien het gebied een onontgonnen gebied is in de moderne geschiedenis van flexibele PMUTS.

De ontwikkelde technologie maakt dure silicium-op-isolator (SOI) wafers overbodig. Het SOI-vrije proces en de op maat gemaakte lood-zirconaat-titanaat (PZT) oplossing voor het afzetten van dunne PZT-films hebben geresulteerd in een goedkope fabricage. Op maat gemaakte PZT-oplossing wordt bereid in een concentratie van 0,4 M in een methanoloplosmiddel, met 15% overtollig lood en 0,05 g polyvinylpyrrolidon (PVP)-polymeer, een porogeen, per millimol (mM) PZT. Ongeveer 0,8-2 µm dikke PZT-dunne film wordt afgezet door het sol-gelproces. De film wordt gekarakteriseerd met behulp van röntgendiffractie (XRD) en Double Beam Laser Interferometer (DBLI)-methoden. 1 µm-film heeft respectievelijk [111]-oriëntatie, 60 pm/V d_{33} en 4 C/m^2 e_{31}.

Na piëzo-elektrische karakterisering worden de rigide PMUT's vervaardigd door depositie van polyimidemembraan passieve laag en etsholtes om membranen te realiseren. De holtes worden geëtst in silicium voor rigide PMUT's. Voor flexibele PMUT's zijn de holtes in polyimide waarvoor dikkere multistap polyimide depositie wordt gevolgd en een extra loslaatstap wordt uitgevoerd. In principe wordt een fabricageprocesstroom ontwikkeld die begint met algemene fabricagestappen die is aangepast om zowel rigide als flexibele apparaten te realiseren met een kleine aanpassing. De PMUT-cellen hebben in totaal 5-14 µm dikke polyimidemembranen inclusief actieve lagen. De membranen hebben een diameter van 100-160 µm. In eerste instantie wordt een kleine volledig geadresseerde array vervaardigd om het fabricageconcept te bewijzen. Later wordt de fabricagestrategie uitgebreid naar een rij-kolom (RC) geadresseerde PMUT met een grotere opening.

De fabricageprocessen hebben de realisatie van nieuwe 2D-arrayontwerpen mogelijk gemaakt met een pitch variërend van 500 µm tot zo laag als 300 µm voor echografietoepassingen. De op polyimide-membraan gebaseerde rigide en flexibele arrays zijn gericht op een bedrijfsfrequentie van ongeveer 1,5 MHz in watermedium om lagere verwachte gevoeligheden door lagere mediumverzwakking bij lagere frequenties tegen te gaan. Ter vergelijking: een RC-geadresseerde array is ook gefabriceerd op een SOI-substraat gericht op ongeveer 5 MHz in water. De resonantiefrequenties in de lucht voor rigide en flexibele arrays met polyimidemembranen zijn respectievelijk ongeveer 3 MHz en 2 MHz. Verrassend genoeg resulteerden de rigide PMUT's met polyimide in een zeer vergelijkbare gevoeligheid in de lucht van ongeveer 0,5 m/s/V als die met siliciummembraan op een SOI-substraat. Alleen al de frequentie van de SOI-gebaseerde array is ongeveer 6,7 MHz in lucht (4,2 MHz in water) met dezelfde 100 µm membraangrootte als die van polyimide. De gevoeligheid van flexibele PMUT in de lucht is echter ongeveer 25 keer lager en ongeveer 20 mm/s/V. De gevoeligheden worden altijd gemeten met een 5V DC bias die de prestaties verbetert. Onder water is de gevoeligheid van flexibele apparaten ongeveer 3 keer lager dan die van stijve apparaten (niet 25 keer lager). Om wat

getallen te geven, per kanaal, stijve d-apparaten genereerden 400 Pa/V bij 5 mm, terwijl flexibele apparaten ongeveer 120 Pa/V genereerden. Het verschil van 10 dB bleek een beperking te zijn voor beeldvorming met flexibele PMUT's. De akoestische druk volgt min of meer een omgekeerde relatie met de afstand.

De stijve arrays zijn met draad verbonden aan op maat gemaakte printplaten (PCB's), terwijl de flexibele arrays zijn geïntegreerd met PCB's met behulp van een flexibele platte kabel (FFC) die met behulp van anisotrope geleidende lijm met de array is verbonden. De arrays zijn met behulp van adapters en connectoren op op maat gemaakte PCB's met de Verasonics-transceiver verbonden. Bovendien wordt, om de arrays geschikt te maken voor beeldvorming, waterdichte afdichting bereikt met behulp van polyimide en epoxy's voor stijve PMUT's. Parylene-C wordt gebruikt als een inkapselingsmateriaal op flexibele PMUT's. Rijen van de RC-geadresseerde arrays worden geaard om het als een lineaire array te gebruiken. Echografiebeelden van metaaldraad en weefselnabootsende fantomen worden vastgelegd met behulp van de stijve RC PMUT-arrays bij spanningen zo laag als $10V_{DC} + 10V_{AC}$.

List of Abbreviations

Al-ScN aluminum scandium nitride. 30

AlN aluminum nitride. 17

BCB benzo-cyclobutene. 10

BOE buffered oxide etch. 44

CMOS complementary metal oxide semiconductor. 3

CMUT capacitive micromachined ultrasound transducers. 3

DBLI double beam laser interferometry. 35

DRIE deep reactive ion etching. 9

DUT device under test. 8

FOM figure of merit. 25

FOV field-of-view. 86

ITO indium tin oxide. 10

KNN potassium sodium niobate. 30

LDV laser doppler vibrometer. 7

LILFU low-intensity, low-frequency ultrasound. 7

MUT micromachined ultrasound transducers. 3

NDE nondestructive evaluation. 2

PDMS polydimethylsiloxane. 8

PET polyethylene terephthalate. 8

PMMA polymethyl-methacrylate. 17

PMUT piezoelectric micromachined ultrasound transducers. 3

POC proof of concept. 96

PVDF polyvinylidene fluoride. 18

PVP polyvinylpyrrolidone. 31

PWC plane wave compounding. 86, 91

PZT lead zirconate titanate. 4

RIE reactive ion etching. 16

RTA rapid thermal annealing. 32

SiN silicon nitride. 10

SLT single-line transmission. 86

SNR signal-to-noise-ratio. 4

SOI silicon-on-insulator. 10

TRT thermal release tape. 17

UV ultraviolet. 17

ZnO zinc oxide. 18

Nomenclature

γ	ratio of the top electrode radius to the PMUT radius
Γ_1	piezoelectric coupling factor
μ	mass per unit area
ν_{ij}	Poisson's ratio for strain in the i-direction due to stress in the j-direction
$\overline{z_p}$	distance from the middle of the piezoelectric layer to the neutral axis
ρ	density of the medium
ε	permittivity (matrix)
a	radius of the membrane
A_{e1}	area of the acoustic domain
c	stiffness matrix
C_0	capacitance of the piezoelectric layer
D	electric displacement vector
D	flexural rigidity
d	piezoelectric strain coefficient (matrix)
d_{tx}	displacement sensitivity
E	electric field vector
e	piezoelectric stress coefficient (matrix)
E_i	Young's modulus in the i-direction
$e_{31,f}$	effective thin-film piezoelectric coefficient

F_{a1}	force in the acoustic domain
F_{p1}	force generated by the piezoelectric effect
$f_{r,\text{air}}$	resonance frequency in air
$f_{r,\text{water}}$	resonance frequency in water medium
G_{ij}	shear modulus in the ij plane
i	current through the PMUT circuit
K_1	mechanical compliance
L_{r1}	acoustic radiation inductance
M_1	membrane mass
P_1	pressure in the acoustic domain
R_1	mechanical resistance related to the material damping
R_d	damping resistance
R_e	electrical resistance at the input
R_{r1}	acoustic radiation resistance
S	strain tensor
s	compliance matrix
T	stress tensor
t	thickness of the material
U	volume velocity output in the acoustic domain
u_1	velocity at the membrane centre
V_1	voltage across the piezoelectric material
v_z	Poisson's ratio at position z
V_{in}	input voltage
Y_z	Young's modulus at position z
z_0	neutral axis position
c	velocity of sound in the medium
k	wave number in the medium

Contents

Abstract vii

Beknopte samenvatting xi

List of Abbreviations xvi

Nomenclature xviii

Contents xix

List of Figures xxiii

List of Tables xxv

1 Introduction 1
- 1.1 Background . . . 1
  - 1.1.1 Flexible MUT Technology Background . . . 4
  - 1.1.2 PMUT Theory . . . 12
  - 1.1.3 Flexible PMUT: State of the Art . . . 15
- 1.2 Objectives and Organization of the Dissertation . . . 23
- 1.3 Oraganization of the Dissertation . . . 26

2 Material Development and Characterization 27
- 2.1 Basics of Piezoelectricity . . . 27
- 2.2 Piezo-electric Material Comparison for PMUTs . . . 30
- 2.3 PZT Sol-Gel Process . . . 30
  - 2.3.1 Solution Preparation . . . 30
  - 2.3.2 Thin Film Deposition . . . 32
- 2.4 Fine Tuning the Sol-gel Process . . . 32
  - 2.4.1 Effect of Changing Solvents . . . 32
  - 2.4.2 Effect of Solvent Dilution . . . 32

2.4.3 Effect of Excess Lead Percentage . . . 33
2.4.4 Effect of Pt Seed Layer Thickness . . . 34
2.4.5 Effect of Adding Polymer . . . 34
2.5 Thin Film Characterization . . . 35
2.5.1 Sample Preparation with the Developed Recipe . . . 35
2.5.2 DBLI Method for d_{33} and e_{31} Characterization . . . 35
2.5.3 Characterization Results and Discussion . . . 36
2.6 Conclusion . . . 38

3 Low Cost Rigid PMUT Technology 39
3.1 Background . . . 39
3.2 Fully Addressed 8×8 Rigid PMUT Array Design . . . 40
3.3 PMUT Fabrication . . . 42
3.3.1 Substrate Preparation . . . 42
3.3.2 Active Layers' Deposition and Patterning . . . 42
3.3.3 Passive Layer Deposition and Patterning . . . 43
3.3.4 Final Release Procedures . . . 44
3.4 Characterization Results and Discussion . . . 45
3.4.1 Material and Electrical Characterization . . . 45
3.4.2 Laser Doppler Vibrometer (LDV) Measurements . . . 47
3.4.3 Underwater Acoustic Characterization . . . 48
3.5 Conclusion . . . 50

4 Flexible PMUT Development 51
4.1 Background . . . 51
4.2 Design-Fabrication Scheme . . . 52
4.3 Preliminary Characterization Results . . . 56
4.4 Conclusion . . . 58

5 Row-Column (RC) Addressed PMUT Development 59
5.1 Background . . . 59
5.2 COMSOL Simulation . . . 60
5.3 Design-Fabrication Scheme . . . 62
5.4 Results . . . 65
5.5 Device Fabrication on the SOI Wafer . . . 68
5.6 Conclusion . . . 70

6 Flexible Row-Column (RC) Addressed PMUT Array 71
6.1 Background . . . 71
6.2 Design-Fabrication Scheme . . . 72
6.3 Results . . . 77
6.4 Updated Design of the Flexible RC PMUT . . . 81
6.5 Conclusion . . . 84

7 Ultrasound Imaging using PMUTs **85**
7.1 Background . . . 85
7.2 Pulse-echo Ultrasound Imaging Basics . . . 86
7.2.1 Imaging Modes . . . 86
7.2.2 Imaging Strategies . . . 86
7.2.3 Image Reconstruction . . . 87
7.3 Experimental Setup . . . 89
7.4 Imaging with the SOI PMUT . . . 91
7.5 Imaging with PMUT on Conventional Wafer . . . 92
7.6 Challenges while Imaging with Flexible PMUT . . . 95
7.6.1 Low Sensitivity . . . 95
7.6.2 Other Operational Challenges . . . 97
7.7 Conclusion . . . 98

8 Summary and Future Work **99**
8.1 Key Contributions . . . 99
8.1.1 PZT Material Developemnt . . . 99
8.1.2 Rigid and Flexible Fully Addressed Arrays . . . 100
8.1.3 Imaging with Rigid Row-Column (RC) Addressed PMUT on a Conventional Silicon Substrate . . . 100
8.1.4 PZT-based Flexible Row-Column Addressed PMUT . . . 101
8.2 Future Work Directions . . . 102
8.2.1 Modeling and Simulations of Flexible PMUT . . . 102
8.2.2 Quality Assessment and Improvement to Enable Imaging with Flexible PMUT . . . 102
8.2.3 3D Imaging with Rigid PMUT . . . 106
8.2.4 Circuit Development and Optimzation . . . 107
8.2.5 Biocompatible and Environmentally-Sustainable Material Development . . . 108
8.3 A Concluding Perspective . . . 108

Bibliography **111**

List of Publications **129**

List of Figures

1.1 Landscape of flexible MUTs . . . 3
1.2 Flexible MUT background . . . 6
1.3 Overview of reported flexible CMUT devices . . . 11
1.4 Electrical model of the PMUT . . . 15
1.5 Overview of flexible PMUT fabrication . . . 16
1.6 Overview of flexible PMUT designs . . . 19
1.7 Overview of reported flexible PMUT devices . . . 20
1.8 Already established rigid SOI based linear PMUT array technology 25

2.1 PZT sol-gel process schematic . . . 31
2.2 PZT thin film process development . . . 33
2.3 1 µm PZT thin film DBLI characterization . . . 37
2.4 PZT thin film $e_{31,f}$ wafer map . . . 38

3.1 Design of a fully addressed 8 × 8 rigid PMUT array . . . 41
3.2 A novel rigid PMUT device fabrication process . . . 43
3.3 Material and electrical characterization of rigid PMUT device . 46
3.4 Characterization of rigid PMUT device with LDV . . . 47
3.5 Underwater transmit characterization of rigid PMUT device with hydrophone . . . 48
3.6 Underwater receive characterization of rigid PMUT . . . 50

4.1 Flexible PMUT schematic . . . 53
4.2 Bendable PMUT fabrication process schematic . . . 54
4.3 Optical microscope images taken during flexible PMUT fabrication 55
4.4 Images of flexible PMUTs on SU8 and polyimide substrates . . 57
4.5 LDV measurements of a flexible PMUT element . . . 58

5.1 COMSOL simulation of a single rigid PMUT element . . . 61
5.2 Row-column (RC) addressed PMUT design . . . 63
5.3 Fabrication steps for the row-column addressed PMUT device . 64

5.4 RC addressed PMUT assembly and characterization setup . . . 65
5.5 LDV characterization of RC addressed PMUT 66
5.6 Underwater characterization of RC addressed PMUT 67
5.7 RC addressed PMUT on SOI wafer 69

6.1 Schematic of a flexible PMUT on polyimide 72
6.2 Flexible RC addressed PMUT design 73
6.3 Flexible RC addressed PMUT fabrication steps 75
6.4 Release and packaging of the flexible RC addressed PMUT array 76
6.5 LDV characterization of RC addressed PMUT 79
6.6 Hydrophone measurements demonstrating the flexible RC addressed PMUT as a transmitter 80
6.7 Flexible RC addressed PMUT as a receiver 80
6.8 Results obtained with an updated design of the flexible RC PMUT 82

7.1 Accessing the columns of the RC PMUT array 89
7.2 Ultrasound imaging setup 89
7.3 Cross sections of the phantoms used 90
7.4 Ultrasound images obtained using SOI PMUTs 92
7.5 Characterizations using tissue-mimicking phantom 93
7.6 Ultrasound imaging using rigid PMUTs with polyimide membranes 94

8.1 64 x 64 row-column addressed PMUT array 106
8.2 11 x 11 fully addressed PMUT array 107

List of Tables

1.1 Quantitative summary of reported flexible MUTs 24

2.1 State of the art piezo-electric thin films 30

3.1 Details of the materials used for the rigid PMUT technology . . 44

4.1 Details of the materials used for the flexible PMUT technology 56

6.1 Lateral dimensions for the flexible row-column (RC) PMUT . . 73
6.2 Comparison with flexible PMUT state of the art 84

7.1 Comparison with state of the art PMUTs for imaging 96

Chapter 1

Introduction

This chapter is adapted from a previously published article: Joshi et al. Flexible micromachined ultrasound transducers (MUTs) for biomedical applications. Microsyst Nanoeng 11, 9 (2025). [1].

1.1 Background

Recently, the healthcare and biomedical device market has seen a shift towards continuous monitoring. Flexible sensor technology has a significant potential to improve diagnostic quality by enabling continuous monitoring while in conformal contact with skin or tissue. This technology can reduce operator variability in medical diagnosis. Moreover, it presents a user-friendly solution because of its biocompatible interface with skin. As more healthcare services shift towards personalized medicine, adhesive smart patches for remote diabetic or heart patient monitoring (some key players are Abbott, Dexcom, iRhythm, and Medtronic) could be as commonplace as Fitbits and Smartwatches. Devices like smart patches are made flexible using substrates such as elastomers, plastics, and hydrogels, allowing for stiction, stretching, or wrapping [2,3]. These devices are typically multilayered integrated systems consisting of flexible or stretchable substrates, active materials, electrodes-interconnects, electronics, and packaging materials. The advantages of these devices, such as being wearable, conformal, light, thin, without being fragile, and cost-effective for large-area applications, make them highly desirable. Various reports discuss the concepts, material-design challenges, and possible applications [4–8]. Moreover, a lot of development has been made in flexible ultrasound transducers for biomedical applications.

Ultrasound technology has been extensively used in various fields such as nondestructive evaluation (NDE) and structural monitoring [9], ultrasonic cleaning and material processing [10], underwater communication [11], particle and cell manipulation [12], and object recognition [13]. Ultrasound is also desirable for low-power consumer applications with spatial bandwidth sharing due to its limited propagation distance in the air and unregulated sound spectrum beyond the audible range [14]. Moreover, ultrasound technology has been extremely useful in healthcare, especially medical imaging based on rigid ultrasound probes, which stands out for diagnostics and disease prevention. However, continuous monitoring and biomedical sensing in mobile settings have been impossible due to the bulkiness of the rigid probes and instrumentation. In comparison with rigid counterparts, flexible ultrasound technology can offer added advantages due to its conformal contact and compact user-friendly design. These advantages enabled the applications of flexible ultrasound transducers, which have already been demonstrated by the classical thick film piezoelectric technology, such as continuous imaging of internal organs, cardiac assessment [15] including blood pressure monitoring [16], and tissue elastography [17]. Conformal contact is also advantageous for a wide variety of applications such as retinal stimulation [18], fetal heart monitoring [19] and needle guidance procedures [20]. Flexible transducers can mechanically focus ultrasound without additional electrical energy, mimicking a parabolic antenna to concentrate waves. In ring-array ultrasound computed tomography (USCT), elevational focusing can be accomplished with an acoustic lens with parabolic curvature attached to the front surface of a flat transducer [21]. This method can be suitable for applications like tissue warming to enhance blood flow, where broad focusing is sufficient, minimizing the need for electronic corrections. This can also be useful in neuromodulation [22], bone injury treatment [23], haptics [24], remote surgeries if combined with gesture recognition [25]. However, more investigation is needed to uncover new applications. Furthermore, flexibility widens the field of view which is useful for Intravascular [26] and transurethral [27] ultrasound with the transducer cylindrically wrapped around a catheter.

Ultrasound transducers generate ultrasound waves utilizing acoustic pressure wave vibration [28] using various methods such as the piezoelectric effect [29], electrostatic actuation [30], magnetostriction [31], and the photoacoustic effect [32]. Conventional machining is typically used for the fabrication of ultrasound transducers involving non-cleanroom techniques [33]. In a classical piezoelectric transducer, the piezoelectric material is utilized as thick piezoelectric ceramic (Bulk piezoelectric) in thickness mode vibration [34]. However, they face performance limitations arising mainly from associated fabrication techniques such as interelement pitch limitations introduced by mechanical dicing. For instance, an 8 MHz transducer operating in a tissue medium has a half-wavelength pitch requirement of less than 100 µm [29]. Besides array pitch, it is

challenging to reduce the power consumption and form factor due to constraints imposed by bulky design. Furthermore, they have limited design flexibility because the resonance frequency is related only to the device's thickness. Another foreseen concern is that most traditional materials used for these transducers are lead-based, which poses environmental hazards.

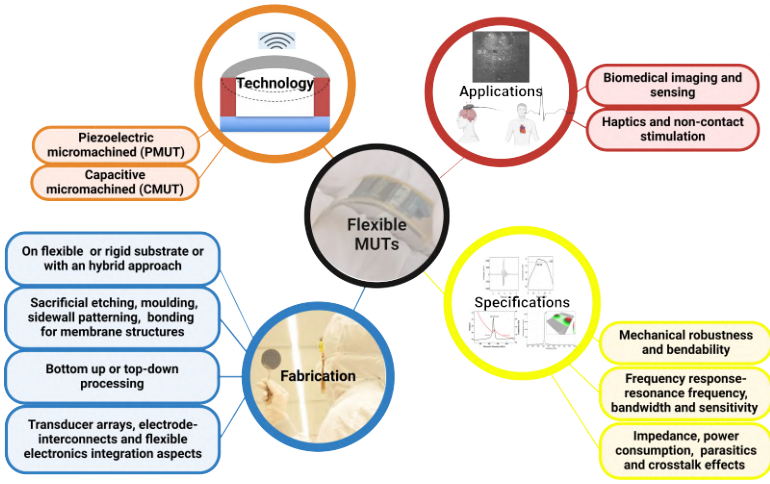

Figure 1.1: Landscape of flexible MUTs.

Nowadays, micromachining techniques play a crucial role in improving the fabrication of ultrasonic devices (MUTs) with considerable performance enhancement [35]. This enhancement can be attributed to small feature sizes, batch fabrication, and the possibility of integration with complementary metal oxide semiconductor (CMOS) technology. MUTs are ultrasonic devices with membrane structures fabricated using micromachining and can be classified into two types. In a piezoelectric micromachined ultrasound transducer (PMUT), a piezoelectric thin film in the membrane actuates the device in flexural mode [36]. On the other hand, a MUT based on the electrostatic principle is called capacitive MUT or CMUT where the capacitor involves an air gap. These transducers also work in a flexural vibration mode with their vibrations set up with electrostatic forces between electrodes [37, 38]. Also, note that there is a fundamental difference between piezoelectric and electrostatic transduction regarding the electromechanical coupling aspect. In the piezoelectric type of transducers, the typically low electromechanical coupling coefficients associated with the piezoelectric materials limit the energy conversion from the electrical to the mechanical domain. Hence, the piezoelectric material technology revolves around exploiting the energy density of the piezoelectric material to push

the electromechanical coupling limit to a higher value [39–41]. However, CMUT membranes can theoretically couple all the energy resulting in an ultra-high bandwidth [42]. The reader is referred to the reported literature for further details on bulk piezoelectric transducers [28], PMUTs [36], and CMUTs [37,38]. Although bulk piezoelectric transducers provide key insights for MUT technology advancement regarding applications, array schemes, and interconnects, fundamentally, flexible MUT devices are fabricated based on the technology pillar of micromachining and MEMS processing. It is basically a PMUT or a CMUT fabrication with a membrane structure combined with various approaches to render them flexible, for instance, the assembly of a piezoelectric such as a thin film of lead zirconate titanate (PZT) on a polyimide substrate [43]. The landscape of flexible MUTs (Fig. 1.1) is uncovered next.

1.1.1 Flexible MUT Technology Background

Need of flexible MUTs and potential applications

A potential application of flexible ultrasound is in biomedical imaging [44]. In ultrasound imaging, a propagating ultrasound wave (pulse) interacts with tissue structures, generating echoes through both reflections and scattering. Reflections provide strong echoes but only from specific large, smooth boundaries (e.g., organ surfaces, bones). Within organs, submillimeter structures make scattered ultrasound a valuable source of information about their internal texture. Although scattered echoes are significantly weaker than those from reflections, modern ultrasound equipment allows this scattered data to be effectively used [45]. The echoes are measured as a function of time and processed to form an image. A few things to consider while optimizing the transducer system for imaging are as follows: (1) For acquiring an image with a superior quality, the transducer should not exhibit ringing. In other words, it should have high bandwidth to effectively shorten the pulse duration and thus increase the imaging resolution. (2) The pulse duration can also be shortened by increasing operation frequency. (3) Additionally, the echo intensity drops drastically with the propagation distance or imaging penetration depth, also resulting in a decreased signal-to-noise ratio (SNR). The transducer is mounted either on the skin or placed inside the body depending on the target organ for imaging and transducer technology. Typically, if the target entities are situated close to the skin, the transducers can be mounted on the skin. In such cases, rigid ultrasound transducers [46,47] with flat bases cannot achieve solid interfacial contact with irregular nonplanar surfaces, for instance during capturing the movement of the knee while exercising. Air gaps at these interfaces lead to significant acoustic energy reflections and wave distortions, creating

imaging artifacts [48]. The ultrasonic gel used to remove the air gaps causes significant canceling of small response echoes and also transmission loss. This problem can be solved by flexible ultrasound transducers, which can achieve conformal contact in an epidermal scheme (as shown in Fig. 1.2a) and has been demonstrated by various research groups. Wong et al. designed a flexible CMUT at 4 MHz for abdominal imaging [49]. They imaged a Gammex 403GS Phantom, which provided visualization of the circular cyst, and successfully reported liver and kidney images (Fig. 1.2a-right). In ultrasound imaging, phantoms are physical objects with a controlled medium for scanning used to test and calibrate ultrasound equipment. Furthermore, at a less mature stage, there are also a few more reported MUTs being developed for medical imaging of other targeted organs. A CMUT reported by Omidvar et al. can operate at up to 15 MHz targeted at musculoskeletal imaging [50]. The CMUT design can be particularly suited for visualizing anatomical structures situated within elongated and curved regions, such as limbs. They demonstrated pulse-echo functionality at 4 MHz. Such flexible (MUT) transducers present a potential solution for continuous monitoring without obstacles, by serving as conformal patches that are comfortable and easily applicable. These wearable devices possess mechanical properties like skin and boast an ultrathin profile that adapts over time, enabling real-time data acquisition. It presents great possibilities such as tracking muscle activity during exercise sessions and transmitting information wirelessly. Moreover, large-area wearable transducers can negate the need for expertise in manually scanning and positioning rigid transducers.

To image internal body parts that are possibly difficult to image with a transducer on the skin, a catheter can be used to put the transducer inside the body. A prominent example is intravascular ultrasound imaging (IVUS) where flexible transducers cover a specially designed catheter, which is put in the arteries [30, 51]. It is needless to say that such applications require an extremely small bending radius, typically a millimeter. IVUS allows seeing the inner wall of blood vessels in living individuals, especially the arteries, where it is used to determine the amount of atheromatous plaque built up leading to stenosis or narrowing of the artery and in turn, heart attacks. The advantage of flexible transducers in such applications is that they can enable signal transmission and detection with increased angular coverage in comparison with rigid probes. A cylindrical transducer can see a 360° view, unlike a rigid planar transducer (see the illustration in Fig. 1.2b). Zhuang et al. demonstrated a conformal CMUT array with a submillimeter bending radius for sideways wrapping a catheter which potentially could enhance the IVUS system by simplifying diagnostics and also the surgical procedures [3]. Another study from Caronti et al. demonstrated pulse-echo characterization of a 10.7 MHz flexible CMUT with high flexibility and curvatures required in convex endocavity probes (scanning inside of the body for rectal or vaginal exams with shallow depth and wider field) [47, 52].

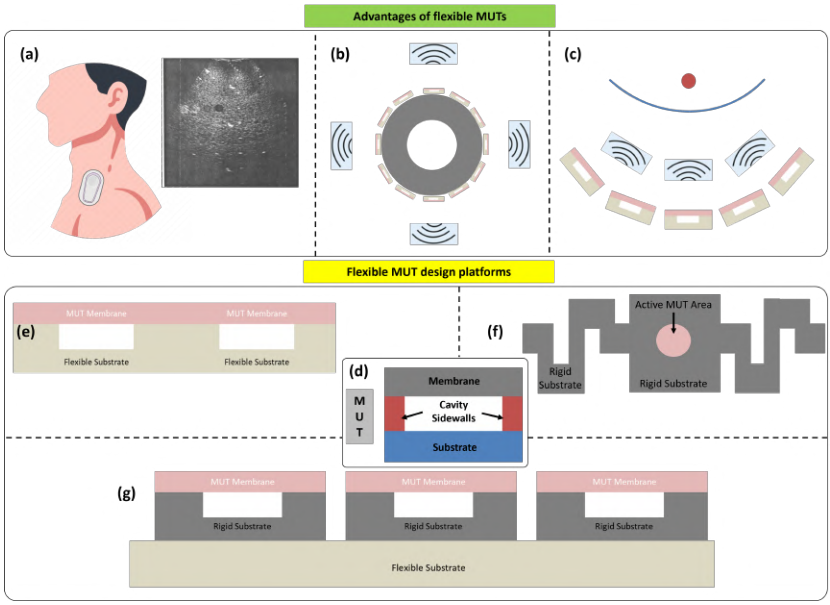

Figure 1.2: Flexible MUT background: (a) An illustration of a flexible ultrasound transducer patch conformally attached to the human neck [16] and ultrasound imaging of Gammex 403GS phantom on the right (adapted with permission) [49]. (b) Schematic showing 360° angular coverage of a cylindrical ultrasound transducer [3] (c) Conceptual objective diagram for mechanical focusing using a flexible ultrasound transducer [53]. (d) Schematic of a MUT, which could be, a PMUT or a CMUT (both contain a membrane, a cavity, and a substrate with a difference in constituent layers). (e) MUT on a flexible substrate [50]. (f) MUTs connected by springs, both fabricated out of rigid substrate [54], (g) Rigid MUTs joined using flexible substrates 2,56 [3, 53]. Schematics are not drawn to scale.

Flexible ultrasound transducers, with variable curvature and focal length within a specific range, function as a curved lens and provide mechanical focusing that reduces the power required for electronic focusing in phased array actuation (illustrated in Fig. 1.2c). This feature is particularly advantageous for haptics and non-contact stimulation applications. Haptics technology utilizes local ultrasound pressure fields to create virtual pressure objects that can stimulate nano-receptors in the fingertip after down-modulation to frequencies below 500Hz. Interuniversity Microelectronics Centre (IMEC) has demonstrated display-compatible polymer-based large-area PMUTs at 400 kHz frequencies [55]. This effectively serves as carrier frequencies for mid-air haptic feedback at

around 1 cm from the source when trading off resolution with attenuation. They recently demonstrated an acoustic twin-trap with mid-air micro-manipulation and levitation [56] as well as a gesture recognition platform [57]. Combining haptics technologies with gesture recognition based on pulse-echo measurements could have interesting implications for remote surgeries. Beyond haptics, the ability to mechanically focus ultrasound with flexible transducers can be used for neuromodulation applications due to non-invasiveness, and strong penetration. Focused ultrasound technology can be used as a treatment for movement disorders, such as Parkinson's disease by targeting specific brain regions, and specifically, low-intensity, low-frequency ultrasound (LILFU) with carrier frequencies between 250 kHz and 500 kHz has been shown to modulate neuronal activity [58, 59]. As a development in this direction, flexible PMUTs have shown promising acoustic pressures suitable for neuromodulation using low-intensity ultrasound [53].

Flexible MUT specifications

Because an ultrasound transducer is a resonant device, its performance is greatly dependent on its resonance behavior which can be understood from characteristics such as resonance frequency, bandwidth, and sensitivity. These specifications (the relevant specifications can be understood from Table 1.1) are determined by performing various characterizations based on targeted applications. For instance, to use a transducer for knee imaging, the following specifications are identified (This application is discussed in-depth later in this chapter): 1) 1.5 - 8 MHz center frequency and 50-100% relative bandwidth, 2) Output pressure of 250-500 Pa/V per channel at 1 cm, Receive sensitivity of 0.2-0.5 mV/kPa, combining both yields round-trip channel sensitivity of > 50 µV/V at 1 cm 3) Flexible and reliable with up to 2 cm bending radius.

Towards characterization for such imaging applications, a pulse-echo experiment can be performed underwater as the water medium has closer acoustic properties to the tissue medium [50]. The echo signal combines transmit and receive response and has information about the transducer resonance frequency and bandwidth. Furthermore, the combined (transmit and receive) sensitivity can be determined from the received signal amplitude in terms of signal attenuation. The signal attenuation directly affects the SNR. The transmit and receive sensitivities can also be measured individually in various ways. For instance, MUTs can be measured at the transducer surface with in-air transmit response recorded by a laser Doppler vibrometer (LDV). Transmit pressure sensitivity can also be noted at a targeted distance using a microphone in-air or hydrophone underwater, while receive sensitivity can be measured using a calibrated transducer that generates a pressure wave with a known amplitude

that can be received at the device under test (DUT) and measured in terms of voltage (details in Ref. [35]). Electrical impedance is another important specification of an ultrasound transducer that indicates its resonance frequency through the peak of the phase response [60], allows the calculation of the coupling coefficient- an important metric of the efficiency of the transducer for electrical-mechanical energy conversion [61], and is important for electronic instrumentation, impedance matching, and transducer power considerations [62].

These performance metrics are the result of various interlinked design considerations involving structure geometry as well as materials and hence present a complex optimization problem. For instance, a factor that affects the transducer's impedance is its intrinsic capacitance. The capacitance depends on the piezoelectric film thickness and dielectric constant for a PMUT whereas on the gap in a CMUT. Moreover, it is also related to the lateral dimensions of the transducer defined by geometry and array design. The lateral and longitudinal dimensions of the constituent layers along with material properties also affect the resonance frequency [62]. Furthermore, the interelement distance (pitch) between the cells or elements becomes critical as a design parameter in imaging applications as a half-wavelength pitch condition should be met to avoid side lobes while performing medical imaging [29]. Pitch together with an active transducer area defines one more parameter called fill factor which shows the effective area of the transducer affecting acoustic pressure [63]. One more key aspect of a flexible transducer design is its flexibility. A specific bending radius range is typically demanded by the application, and the transducer is mechanically designed to meet the bending radius criteria. The bending radius depends on the used materials and transducer assembly.

Flexible MUT material design and assembly

The schematic of a MUT is shown in Fig. 1.2d marked by the presence of a membrane, a cavity, and a substrate. The substrate is typically the thickest part of the transducer assembly and affects the flexibility of the devices. On the other hand, active and structural materials for these transducers are typically thin films. Based on the substrate material flexibility and the way transducer elements are assembled three categories of flexible, meta-rigid, and hybrid platforms for the flexible MUTs can be explained.

Fig. 1.2e shows the most common flexible transducer design approaches, transducer on a flexible substrate (referred to as 'flexible substrate-based approaches' in the next sections), which could be stretchable such as polydimethylsiloxane (PDMS) [64], or just bendable like polyimide [50], polyethylene terephthalate (PET) [65]. In such designs, low-modulus materials

like polymers make up most of the transducer to ensure local flexibility. High-modulus materials such as silicon, its compounds, other piezo-ceramics, metal foil substrates, or thin metal/ceramic films forming interconnects or active layers are typically not more than a few µm in thickness to maintain flexibility throughout. However, these devices suffer from low performance because of several reasons: 1) low modulus structural layers limit the resonance frequency of devices; 2) often these structures, are associated with higher material damping and hence strongly dampen the vibrations reducing the sensitivity.

In contrast, the silicon MEMS technology has demonstrated quite promising performance. Sadeghpour et al. (design concept in Fig. 1.2f) demonstrated an approach for flexible ultrasound transducers using rigid silicon springs as flexible links [54]. This interesting way to modify a rigid structure to a flexible one by adding a spring as a compliant structure is referred to here as the meta-rigid approach where the link between the transducers constitutes compliant structures made out of stiff material. Moreover, the complete device processing can be done on a silicon wafer using standard micromachining techniques with the benefits of high performance, reliability, cost-efficiency, and the possibility of CMOS integration. However, fill factors and flexibility of the transducer array are limited due to complicated steps in the fabrication process, especially deep reactive ion etching (DRIE), and also the compliant link. In the context of array design, such a design allows for limited space for interconnects. This worth researching approach has not further been explored in the literature and requires further study to mature and address the aforementioned problems. In a word, flexible substrates allow for better flexibility and possibilities for electronics integration while devices built on rigid silicon substrates tend to have better transducer performance metrics, such as transmit sensitivity.

The tradeoff between flexible substrate technologies and silicon MEMS can be partially overcome by the hybrid approach, which involves fabricating devices that are partly flexible and partly rigid [66]. This approach is becoming increasingly popular in flexible ultrasound technology, where both flexibility and high performance are important. In ultrasound transducers, the hybrid approach involves rigid transducer elements joined through flexible links (referred to as 'hybrid approaches' later as well). For instance, Lee et al. fabricated a silicon-based array of transducers and then bonded them to a thick PDMS matrix. Next, the wafer is thinned followed by element dicing (design concept in Fig. 1.2g) [53]. The transducers on the rigid silicon substrate have shown high acoustic pressures while the link between the transducers with low Young's modulus structures allowed the flexibility of the complete transducer array. However, low fill factors and electronics integration again present challenges. Interconnect design and electronics integration is easier with a relatively flatter and continuous topography throughout the array on flexible substrates.

Flexible CMUT state of the art: An overview

Among MUTs, electrostatically actuated CMUTs have shown improved coupling coefficients and bandwidths [67]. A CMUT element (in Fig.1.5a) has a capacitor structure with a rigid metalized substrate and a thin metalized insulating membrane, over a cavity. Upon applying a DC voltage across these electrodes, the electrostatic forces and membrane's inherent rigidity counterbalance, and ultrasound is generated from the membrane oscillations with an AC input.

Along with the rigid CMUT developments towards applications including imaging [67], various studies report flexible CMUT fabrication, which can be divided into silicon-based and polymer-based. Wong et al, fabricated flexible CMUTs using sacrificial etching followed by thinning-down silicon (Fig. 1.3a) [49]. A hybrid approach from Zhuang et al described the filing of trenches etched in silicon-based CMUTs with PDMS to make it bendable (Fig. 1.3h) [3]. Another notable work used double silicon-on-insulator (SOI) wafer bonding to fabricate CMUT which were eventually transferred to PDMS, a peculiarity of the design being row-column-addressable for 3D imaging (Fig. 1.3j) [68]. An alternative strategy presented by Caronti et al. encapsulated reverse fabricated CMUTs between an epoxy backing layer and a silicone elastomer coating (Fig. 1.3i) [52]. Yet another recent paper reported the dicing of rigid CMUT fabricated by adhesive wafer bonding using benzo-cyclobutene (BCB) and filling the tranches using PDMS, targeted towards photoacoustic imaging [69]. However, these technologies are prone to high residual stress, cracking, or handling difficulties. Alternatively, researchers explored using polymers for simpler and cost-effective production. The initial innovation, termed "sonic paper", utilized sacrificial layer etching for CMUT fabrication and reported a 3 mm bending radius (Fig. 1.3b) [70]. Another notable invention was the introduction of concave bottom electrodes by Cheng et al, and Shi et al, employing silicon nitride (SiN) and PDMS (Fig. 1.3g) structural materials, respectively [64, 71]. Moreover, Electrode-structural material combinations such as ITO-SU8 (Fig. 1.3f) and titanium-polyimide (Fig. 1.3c) are introduced considering transparency and biocompatibility aspects, respectively [72, 73]. Recently, Omidvar et al. presented advanced characterizations of their flexible CMUT including pulse-echo and durability while bending, and reliability for continuous operation (Fig. 1.3d) [50]. More recently, yet another process modification has been reported which uses SiN structural layer instead of SU8 and presents scalable electrical characterization methods involving an impedance analyzer along with automatic probing and Python scripts to detect the pull-in voltage and resonance frequency, which can be used to assess yield and uniformity (Fig. 1.3e) [74]. However, CMUTs required high DC bias (>50 V).

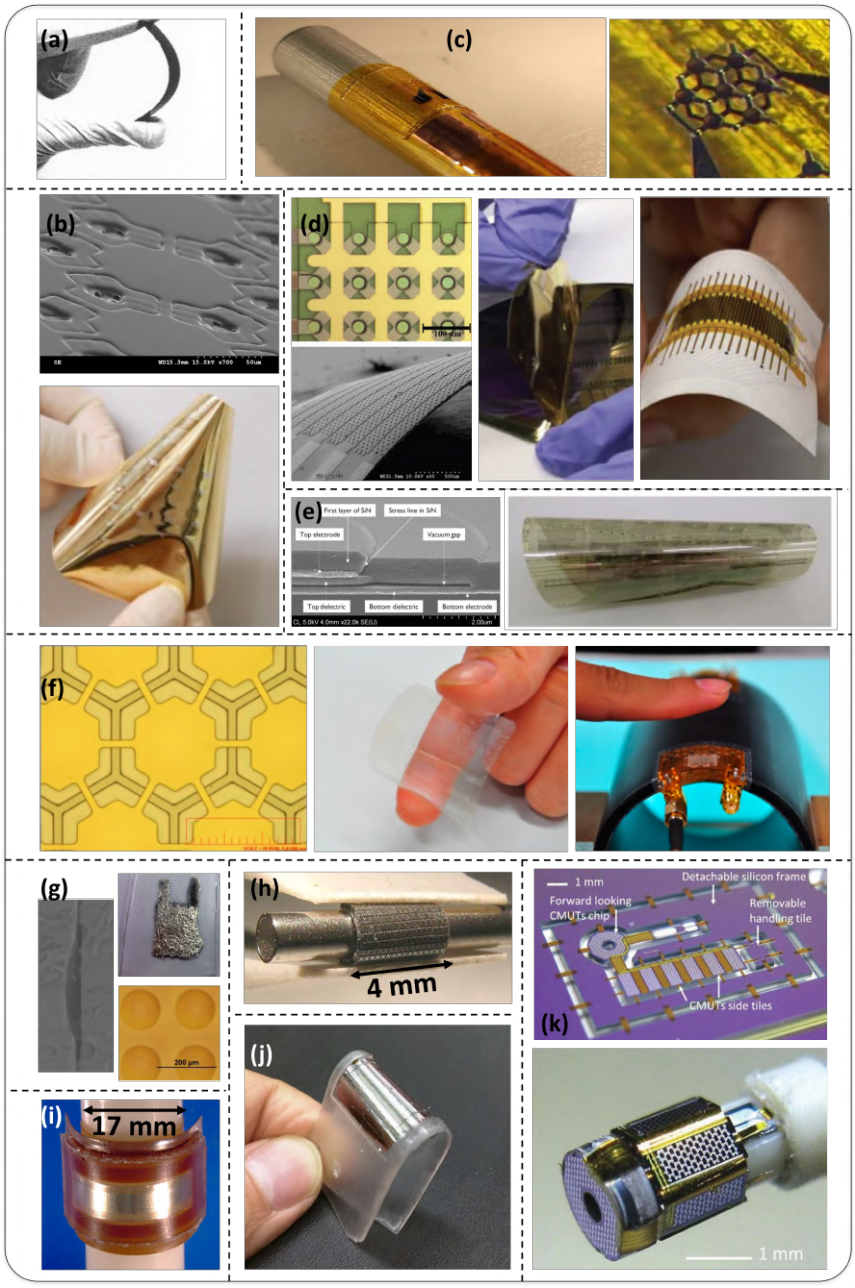

Figure 1.3: Overview of reported flexible CMUT devices:

Sacrificial layer etched CMUTs. (a) CMUT with thinned-down silicon [49]. (b) SEM image of a polymer membrane with opened vias (top) and released 'Sonic Paper' CMUT arrays (bottom) [70]. (c) Polyimide-based CMUT wrapped around a cylinder with a bending radius of 2.5 mm (left) and optical image of the curved CMUT with the 7 membranes of the device under test [73]. (d) Microscope (top left) and SEM (bottom left) images of 'polyCMUT' on a polyimide substrate, flexible substrate release from the silicon wafer carrier (middle), and optical images of released device on a flexible PCB (right) [50]. (e) Laser-released CMUTs on polyimide with SiN structural layer along with SEM image [74]. (f) SU8 CMUT realized using lamination process- Optical microscope image on the left, transparency shown in the middle, and flexibility on the right [72]. (g) CMUT on PDMS with a liquid metal electrode and concave cavity [64]. (h) Flexible substrate fabricated by refilling through-wafer trenches in silicon with PDMS [3]. (i) Photographs of a flexible (hybrid) CMUT array after bending around a cylinder with a radius of 8.5 mm [52]. The same is fabricated by the reverse fabrication process. (j) Row-column CMUT fabricated out of 2 bonded SOI wafers [68]. (k) CMUT device attached in silicon frame using polyimide tabs (top). Forward and side-looking hybrid CMUTs at the tip of 2-mm diameter catheter [75]. All pictures have been adapted with permission.

1.1.2 PMUT Theory

PMUT (schematic in Fig. 1.5a) consists of a membrane with a piezoelectric thin film and operates in flexural mode. The membrane typically contains a patterned layer stack of active layers (electrodes and piezo-electric thin film) along with a passive layer. The membrane is driven by applying an excitation voltage between the top and bottom electrodes. The applied electric field forms transverse stress in the active piezoelectric layer, which causes the membrane to displace out-of-plane, generating a pressure wave in the outer medium. The resonance frequency of the PMUT, because of the flexural mode, is mainly defined by the geometry and materials as they influence the mechanical stiffness and mass density of the membrane [61]. However, residual stress in the membrane developed during fabrication can drastically affect the resonance frequency and this is one of the main reasons why practical PMUTs usually perform differently than their theoretically expected performance. Also, this makes membrane structure fabrication challenging.

The resonance frequency of the PMUT in the air can be given by Equation (1.1) below. Here, D is the flexural rigidity of the membrane and a is the radius of the membrane. μ is mass per unit area. ρ_i and t_i are the densities and thicknesses of the materials used in the membrane stack. k is the proportionality constant depending on the mode of vibration and can be chosen as 10.4 for

the first mode [63]. Flexural rigidity, D, is the cubic function of membrane thickness that can be shown as an integral (in Equation (1.3)) where z_0 is the neutral axis position calculated using Equation (1.4). In a PMUT, the neutral axis is the plane within the vibrating membrane where bending-induced stress transitions from tensile to compressive. It plays a critical role in determining the strain experienced by the piezoelectric layer during vibration. For optimal performance, the piezoelectric layer (e.g., PZT) is positioned away from the neutral axis to maximize strain, thereby enhancing the piezoelectric coupling and energy conversion efficiency. The location of the neutral axis is influenced by the thicknesses and material properties (e.g., Young's modulus) of the membrane's layers, as seen in Equation (1.4). Y_z and v_z are Young's modulus and Poisson's ratio of the material present at the z position. The linear mass density is in the denominator of the equation (1.1) and is a linear function of thickness (in Equation (1.2)). Equation (1.5) shows that the water medium reduces the resonance frequency in comparison with the air medium [63].

$$f_{r,air} = \frac{1}{2\pi} \cdot \frac{k}{a^2} \sqrt{\frac{D}{\mu}} \propto \frac{t}{a^2} \tag{1.1}$$

$$\mu = \sum_i \rho_i \cdot t_i \tag{1.2}$$

$$D = \int_0^t \frac{Y_z (z - z_0)^2}{1 - v_z^2} \, dz \tag{1.3}$$

$$\int_0^t Y_z (z - z_0) \, dz = 0 \tag{1.4}$$

$$\frac{f_{r,\text{water}}}{f_{r,\text{air}}} = \frac{1}{\sqrt{1 + 0.84 \cdot \frac{\rho_{\text{water}} \cdot a}{\mu}}} \tag{1.5}$$

A more detailed description of the working of a PMUT can be given using the electrical model, briefly explained next. In a PMUT electrical model, several key components and parameters are used to describe its behavior (follow Fig. 1.4). V_{in} is the voltage applied to the system. R_e represents the resistance due to cables and interconnects. C_0 indicates the PMUT's intrinsic capacitance and it depends on the piezo-electric material's dielectric constant and thickness, as well as electrode area. Note that, R_e and C_0 form a low pass filter, and

hence, for efficient working of the device, the resonance frequency of the PMUT should be designed well below the cutoff. Since, C_0 itself is dependent on lateral dimensions, the resonance frequency, for instance, can be tuned by choosing an appropriate passive layer thickness for the membrane. For high-frequency operations, R_e and C_0 should be individually minimized. Additionally, it is needless to say that the contribution of parasitics in the C_0 should be minimized. R_d refers to the dielectric losses in the piezoelectric layer and they depend on the quality of piezo-electric material. V_1 is the potential difference measured across the piezoelectric layer. i is the current through the circuit. F_{p1} is the mechanical force produced by the piezoelectric material when it is subjected to voltage, related to the latter by the piezoelectric coupling factor Γ_1 and is given by [60]:

$$\Gamma_1 = 4\pi(\gamma^2)(\gamma^2 - 1)e_{31,f}\overline{z_p} \tag{1.6}$$

Here, γ is the ratio of the top electrode dimensions to the PMUT membrane dimensions, $e_{31,f}$ is the effective thin-film piezoelectric coefficient, and $\overline{z_p}$ is the distance between the center of the piezoelectric layer and the neutral axis.

In the mechanical model, K_1, R_1, and M_1 represent the membrane stiffness, the mechanical damping, and the membrane mass for the first mode. Stiffness and mass can be calculated as follows [63]:

$$K_1 = \frac{64\pi D}{3a^2}, M_1 = \frac{\pi a^2 \mu}{5} \tag{1.7}$$

Moreover, displacement sensitivity d_{tx} can be calculated as follows [76]:

$$d_{tx} = \Gamma_1 Q / K_1 \tag{1.8}$$

The resonance frequency can be given by

$$f_r = \frac{1}{2\pi}\sqrt{\frac{K_1}{M_1}} \tag{1.9}$$

u_1 describes the velocity at the center of the membrane. The force F_{p1} induces vibration velocity u_1 in the mechanical domain, generating force F_{a1} between the membrane and the medium. Acoustic pressure P_1 can be linked to F_{a1} via the effective PMUT membrane area A_{e1} and is one-third of the circular PMUT area. From the acoustic domain, the acoustic impedance Z_a of a clamped radiator can be expressed as [63]:

$$Z_a = R_{r1} + j\omega L_{r1} \tag{1.10}$$

where R_{r1} is the acoustic radiation resistance and L_{r1} is the acoustic radiation inductance. From the acoustic impedance, The imaginary part, $j\omega L_{r1}$, can be looked at as an additional mass to the PMUT membrane mass by transferring it to the mechanical domain [62]. R_{r1} and L_{r1} can be expressed as: ρc times the respective coefficient obtained from the graph in Fig. 1.4. Here, k is the wave number in the medium. The acoustic domain right end is shorted for a PMUT during transmission.

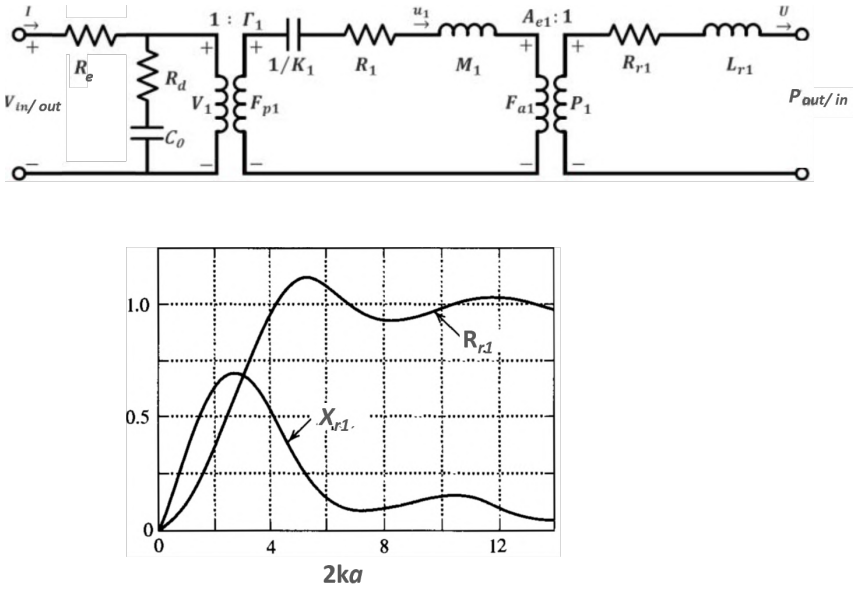

Figure 1.4: Electrical model of the PMUT on the top with electrical, mechanical, and acoustic domains from left to the right (separated by the transformers) [60] and radiation impedance coefficients on the bottom [77].

1.1.3 Flexible PMUT: State of the Art

The following discussion is about various approaches to fabricating flexible PMUTs. The fabrication processes are schematically shown in Fig.1.5. Fig. 1.6 and Fig. 1.7 present schematics and images of reported flexible PMUTs, respectively.

During the fabrication of MUTs, a membrane, and a cavity will be produced on a substrate as illustrated in Fig.1.2d. For cavity fabrication, the following processes are typically performed: (1) subtractive processing of sidewall material where normally, dry etching, either reactive ion etching (RIE) or DRIE, laser machining or photo-patternable epoxy development processes are performed. This is common for PMUTs where it is usual to not have a separate substrate layer. (2) sacrificial layer etching where first, a sacrificial layer is patterned on a substrate. Then, membrane and cavity sidewalls are deposited. Finally, the sacrificial layer is etched to form a MUT cavity, which is a common method of CMUT fabrication.

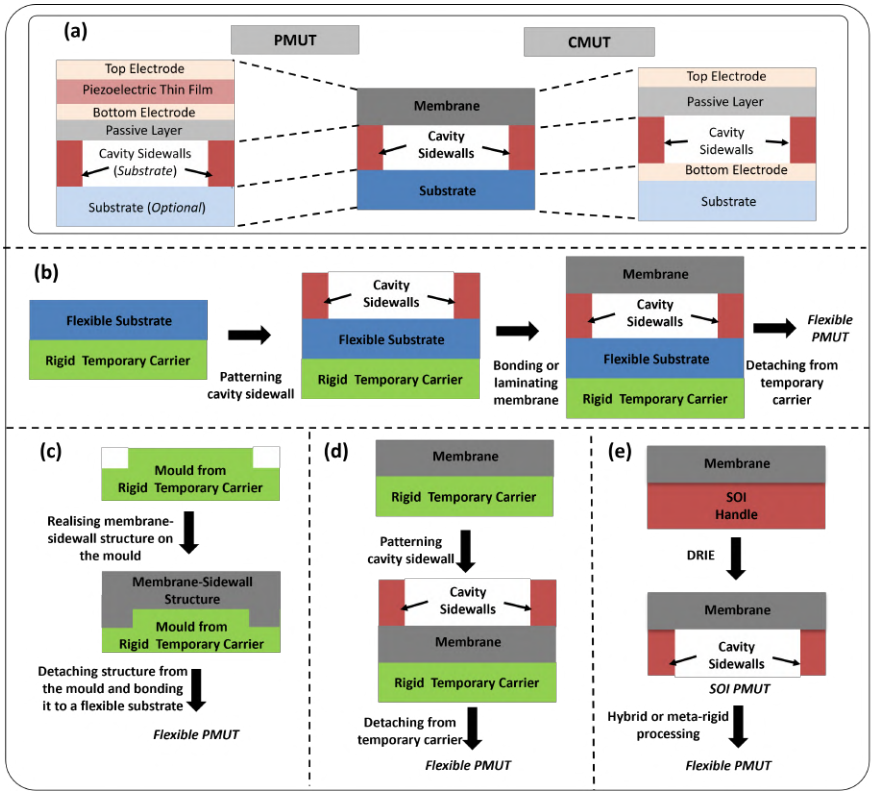

Figure 1.5: Overview of flexible PMUT fabrication: (a) Schematic of a PMUT [36]. (b) Bonding or lamination process [78]. (c) Molding for cavity fabrication in PMUTs followed by bonding to a flexible substrate [79]. (d) Top-down fabrication for PMUTs [43]. (e) SOI PMUTs followed by hybrid or meta-rigid processing [53, 54]. The schematics are not drawn up to scale.

Beyond realizing a cavity, the flexible MUT fabrication can often involve more process steps, listed next: (3) bonding procedures of a membrane with the cavity sidewalls or bonding of cavity sidewall to a substrate or both. This can be achieved with a simple thin film coating or lamination or complicatedly, by transferring a layer realized on a temporary carrier, involving the carrier wafer bonding and release. (4) Release of flexible structures from temporary carriers (the use of rigid temporary carriers like silicon or glass is very common). Moreover, it is also possible to perform the above processes in reverse order where first, membrane structures followed by cavity sidewalls are realized on a temporary carrier in a top-down scheme. Optionally, they are bonded to a flexible substrate. Finally, the temporary carrier is released to complete the fabrication. A complete flexible MUT fabrication process flow will typically involve a combination of these processes which are analyzed in detail for PMUTs.

Flexible substrate-based approaches

Sun et al. reported a process for flexible aluminum nitride (AlN) PMUTs (see Fig. 1.5b for the fabrication schematic, Fig. 1.6a for the device schematic, and Fig. 1.7a for images of the fabricated device) [80]. The bottom electrode layer is used as the structural layer to reduce the input impedance. This could be advantageous for resonance behavior as well, but this could reduce the device flexibility meriting careful considerations of the design. During fabrication, the PMUT active layers were first fabricated on a temporary silicon carrier with an oxide sacrificial layer. Polyimide was deposited on another silicon carrier with polymethyl-methacrylate(PMMA) as a sacrificial layer. This polyimide serves as a flexible substrate and sidewall material for the flexible PMUT. The polyimide was etched for realizing sidewalls. The next step is to bond the membrane. To achieve this, another carrier, a PDMS stamp, was introduced to transfer the membrane on the sidewall structure. After the removal of the sacrificial layer, the structure was transferred to the PDMS stamp. The membrane was then aligned with a sidewall structure. At this point, the flexible PMUT is attached to a silicon carrier from one side and PDMS from the other. With an appropriate move rate, the device was separated from PDMS, and acetone was used to dissolve PMMA to release the device from the silicon. Note that, here, controlling adhesion forces between the donor, the structure, and the receiver is done through sacrificial layers, and additional surface treatments such as ultraviolet (UV) exposure, or oxygen (O_2) plasma. Moreover, multiple carriers can increase the cost and inconvenience during manufacturing.

Studies by Liu et al. introduced thermal release tape (TRT) instead of sacrificial layers on a rigid carrier [65, 79, 81]. TRT is a tape with tunable adhesion and is widely used in graphene transfer processes [82]. After heating to $90 - 100^{o}$C,

the adhesion vanishes permanently. This makes the transfer printing process simple. It takes out additional complex processes such as surface treatments in the case of PDMS stamps, and vias for sacrificial release, which improves the micromachining stability. However, TRT cannot support high-temperature fabrication. One of their studies demonstrated a one-side silver (Ag) coated commercial polyvinylidene fluoride (PVDF) sheet along with the silver pasted top electrode as a thick PMUT membrane (fabrication scheme in Fig. 1.7d) [81]. A PVDF film, apart from piezoelectricity (and dielectricity), provides high bandwidth along with sensitivity, transparency, and high bendability [83]. For patterning top Ag, laser-patterned polyimide tape (Kapton) is used as a shadow mask. This membrane assembly is inverted and pasted on a temporary carrier. Next, polyimide was spun on top of a PVDF film having two functions: passive and adhesion layer. A thick polyimide (Kapton) sheet patterned by laser micromachining served as a flexible substrate and cavity sidewalls. The substrate was aligned-bonded on PVDF film without extra pressure. Such fabrication process can be extended to the use of alternative materials for substrates and sidewalls such as PET (schematics in Fig. 4b and images of the fabricated array in Fig. 1.7b) [65]. The paper also demonstrated that a laser-processed substrate can be used as an adhesive. However, this fabrication lacks a passive layer which is instrumental in improving the sensitivity of the PMUT device by pushing the neutral axis away from the piezoelectric [84]. A recently published study demonstrated another possibility with a similar design- to structure the membrane to be curved which is shown schematically in Fig. 1.6c [85]. This resulted in performance enhancement by a factor of 2 in comparison to the flat counterpart. For the fabrication, the multilayer membrane film (PET passive layer, PVDF piezo-electric, and gold (Au) electrodes) is inserted between the casting mold made up of copper (Cu) and then hot-pressed for 5 min at a temperature of 95°C under a 2-bar pressure. The alignment of active layers on the cavity sidewalls during the bonding process as demonstrated in previous designs is either prone to inaccuracies or needs specialized equipment which is especially critical for designs with very small features.

Yet another work from Liu et al. demonstrated a PMUT based on flexible and transparent mica substrates (Fig. 1.5c shows the fabrication schematic and Fig. 1.6d shows device schematic) [79]. This avoided alignment during the bonding procedure and is achieved using a molding process, aligning membranes and sidewalls during molding, which simplifies the process of realizing the membranes. The fabrication started with a silicon mold, which defines the membrane cavity, formed by standard photolithography and DRIE. Then, the polyimide passive layer followed by piezo-electric zinc oxide (ZnO) placed between Aluminum (Al) electrodes was deposited. In parallel, a thin PDMS layer was spun onto the mica substrate as an adhesive, which was partially cured. Using TRT, the silicon mold structures were then transferred onto the mica-PDMS assembly.

Subsequently, thermal treatment was applied to complete the curing process of the adhesive while simultaneously removing the TRT. Lastly, the mica was mechanically exfoliated to achieve a final thickness of 25 µm. (due to its unique two-dimensional layer structure) which achieved the desired transparency as well as flexibility. However, the process still involves some complications due to multiple carriers and stack transfer.

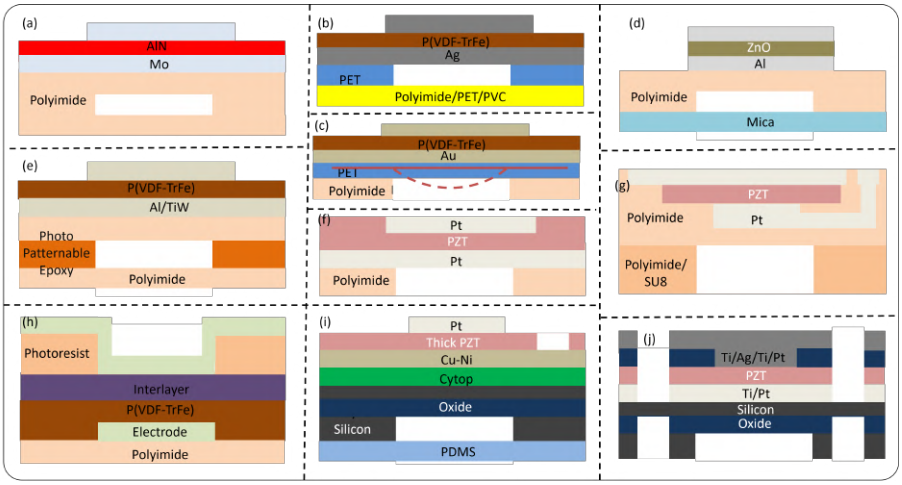

Figure 1.6: Overview of flexible PMUT designs: (a) Schematic of a PMUT realized using a sacrificial release and transfer process [80]. (b) Schematic of a PMUT realized using laser micromachining and TRT [65]. (c) Flexible PMUT with the membrane being curved via hot-processing [85]. (d) PMUT on Mica substrate using DRIE silicon mold and adhesive bonding [79]. (e) Released PMUT fabricated using bottom-up processing on a single temporary carrier [78]. (f,**g**,h) Flexible PMUTs realized using a top-down process flow in combination with sacrificial membrane release and mechanical release, respectively [43, 86]. (i,j) Hybrid and meta-rigid approaches on SOI wafers [53, 54].

In a flexible PMUT platform developed at IMEC, the fabrication was entirely carried out on a single temporary carrier (follow Fig. 1.5b for the fabrication schematic, Fig. 1.6e for the device schematics, and Fig. 1.7c shows the fabricated device images) [78]. They coated an epoxy resin on top of polyimide deposited on a glass substrate and patterned it by photolithography, to create the sidewalls of the membrane. A polyimide film was then laminated onto the top surface of the support layer through adhesive bonding, serving as a passive layer for the subsequent formation of electrodes and PVDF layers. Finally, the initial polyimide foil was detached from the carrier glass substrate, allowing for

flexibility. Carrying out all the processing on a single rigid temporary carrier wafer with a final release step is comparatively easier. This approach has been followed also in various reported top-down flexible PMUT processes.

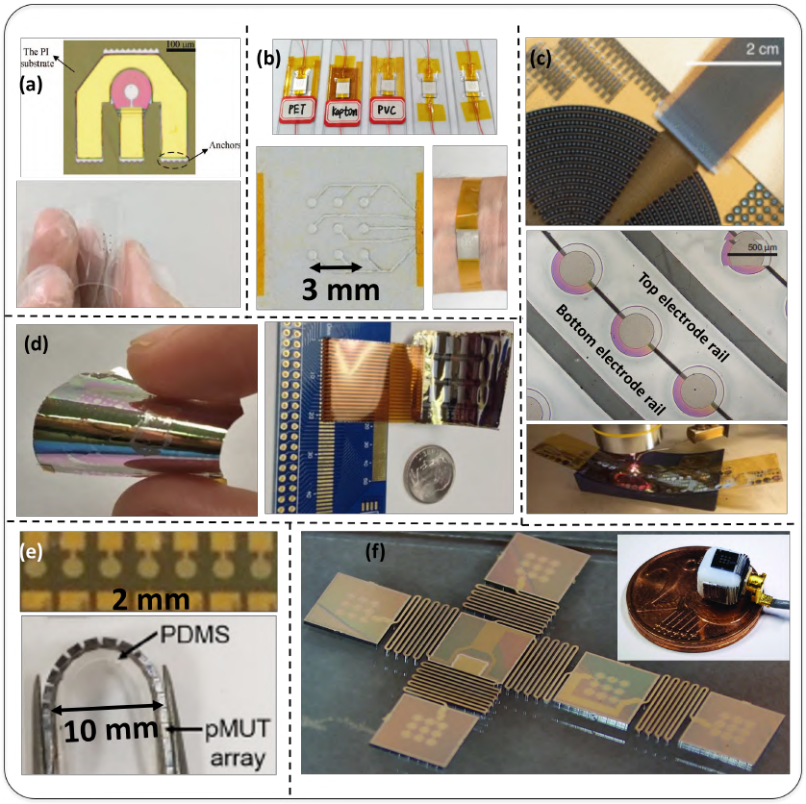

Figure 1.7: Overview of reported flexible PMUT devices: (a) Optical microscope image of flexible PMUT membrane transferred on a polyimide substrate (top) and released device (bottom) [80]. (b) PMUT assembled on various flexible substrates (top left), view of the patterned Ag top electrodes (bottom left), and device wrapped around the wrist (bottom right) [87]. (c) Polymer-based PMUTs fabricated using Bottom-up processing. Image of the annular array (top), magnified image using an optical microscope (middle), and flexible device being characterized (bottom) [56, 78]. (d) Released PZT-based PMUTs using a top-down process, under bending (left) and with ACF connections (right) [43]. (e) Optical microscope image (top) and flexibility (bottom) of SOI-based hybrid PMUT [53]. (f) SOI-based meta rigid PMUT released and flexed (inset) [54]. All pictures have been adapted with permission.

In a top-down process, layers are stacked in a reverse manner. The most critical part of the device, the membrane, is processed first followed by sidewall stacking, and can be released without having a separate PMUT substrate layer. Peter et al. introduced such an inverted flexible PMUT configuration (see Fig. 1.5d for the fabrication schematic and Fig. 1.6h for the device schematic) [86]. The transducers were monolithically fabricated on top of a thick polyimide substrate, which also formed a part of the membrane as a structural layer, on a glass carrier. The polyvinylidene fluoride-trifluoroethylene (PVDF-TrFE) layer was used as a piezoelectric material along with electrode patterning. To prevent the layer diffusion of photoresist into piezoelectric, a thin inorganic layer was introduced on the (PVDF-TrFE). Next, a thick layer of photoresist is applied via spin coating to minimize the damping of membrane vibrations. The membrane is realized by an opening in the photoresist layer. Following this step, the transducers are detached from the glass either mechanically or using laser assistance. Alternatively, a sacrificial layer can facilitate the release process. Liu et al. introduced a transfer technique enabling PZT thin films on a substrate with a high-temperature growth process to be transferred to thin flexible polyimide [88]. Using the same, the group demonstrated PMUTs fabricated on polyimide substrates using released PZT films (see Fig. 1.5d for fabrication schematic, Fig. 1.6f for the device schematic, and Fig. 1.7d for the images of fabricated devices) [43]. A ZnO sacrificial layer was used on a silicon wafer, whereas aluminum oxide served as a diffusion barrier between ZnO and PZT. PZT had 2% niobium (Nb) doping. Next, polyimide was patterned to form cavity sidewalls (also serves as substrate) before the sacrificial layer release. Authors claimed superior electrical properties of the released PZT films compared to the ones on rigid substrates due to declamping from the substrate. However, as the membrane consists of only the PZT and electrodes, lacking a structural layer, hence is fragile. Moreover, the resonance frequency is very low.

Hybrid and meta-rigid approaches with silicon On insulator (SOI) fabrication

SOI technology is becoming a mature and convenient PMUT fabrication technique, because of the easy realization of membranes with the already built-in passive silicon device layer. Hence the fabrication involves the deposition of active layers on the silicon device layer of the SOI wafer. The device layer also acts as the passive layer of the membrane. DRIE is performed on the patterned backside which etches the silicon handle completely to form PMUT membranes. Buried oxide acts as an etch stop. This is briefly demonstrated in Fig. 1.5e. Lee et al. demonstrated a hybrid approach for a flexible PMUT array using SOI PMUTs (device schematic in Fig. 1.6i and images of the fabricated device in Fig. 1.7e) [53]. Then the ultrasound transducer array was bonded to PDMS using an O_2 plasma treatment and was diced to achieve flexibility. However, mechanical

dicing limited the element density. Moreover, it becomes difficult to interconnect array elements due to topographical discontinuity. Another shortcoming is that a 50 µm thick PZT sheet resulted in 80 Volts of the actuation voltage. In contrast to this, Sadeghpour et al. demonstrated SOI flexible PMUTs with a PZT thin film and silicon springs structures (device schematic in Fig. 1.6j and images of the fabricated device in Fig. 1.7f) [54]. The silicon springs (acting as hinges) are fabricated by DRIE, and mechanical dicing was avoided. The arrays are electrically connected through metal tracks on top of the hinges. The proposed flexible PMUT array benefits from a high-performance PZT thin film with a small actuation voltage of the PMUT elements in comparison with the previous hybrid design and also demonstrates excellent flexibility. However, due to the introduction of springs and the DRIE process, the fill factor is compromised. The other challenge is that very small space (on the springs) is available for interconnects. This makes it difficult to access PMUTs individually and scale them up for applications such as biomedical imaging.

To summarize, attributing to the advantages due to micromachining and bendability, various flexible PMUTs have been developed and reported in the literature. These approaches are silicon-based or polymer-based. silicon-based devices provide high acoustic pressures and hence satisfactory output performance. To make a silicon-based device bendable, there are mainly three possibilities: 1) Island-spring-based designs where the transducers reside on islands and interconnecting spring structures render bendability [54]. This approach suffers from a limited bending radius, interconnect area, and fill factor. 2) silicon-based transducers on islands, connected by flexible link structures made from low-modulus materials such as polyimide or PDMS [53]. Here also, low fill factors and electronics integration present challenges. Interconnect design and electronics integration is easier with a relatively flatter and continuous topography. This can be achieved with the third silicon-based approach which is 3) by thinning down silicon to easily bend it and mount it on curved substrates or fixtures [49]. However, such a design is fragile. If silicon is replaced with polymer-based materials such as polyimide, even the thin designs are quite robust while providing excellent opportunities for interconnects and electronics with better bendability. A drawback of the polymer-based approach is that the devices suffer from low sensitivities and resonance frequencies because of the low rigidity modulus of the materials [65].

Note that, flexible PMUT state-of-the-art devices have to date only been reported with sub-MHz resonance frequencies thus making them unsuitable for ultrasound imaging (US). There are no reported 2D flexible PMUT arrays for medical imaging due to the trade-offs and limitations briefly described above. Table 1.1 provides a detailed overview of flexible PMUTs and CMUTs, revealing the need for further development to meet specific application requirements (for

instance, knee assessment requires 8 MHz center frequency, Output pressure of 250-500 Pa/V per channel at 1 cm, Receive sensitivity of 0.2-0.5 mV/kPa, and 2 cm bending radius). No flexible PMUT exists yet for imaging applications because of their lower reported frequency and insufficient array size.

The application of knee assessment with flexible PMUT technology focuses on the development of a specialized, non-invasive ultrasound tool for planning and monitoring soft-tissue balance (proper alignment and tension in the tissues, minimizing complications like instability or implant failure) during joint replacement surgeries like total knee arthroplasty (TKA) [89]. This can leverage the bendability of ultrasound transducers to conform to complex anatomical surfaces, such as the knee joint, to enable high-resolution imaging of ligaments, tendons, and muscles. Imaging allows for the creation of strain maps through methods like speckle tracking, which analyzes the motion of natural acoustic patterns, called speckles, within tissue. By providing real-time, dynamic information, this technology can facilitate pre-surgical planning, allowing surgeons to assess and optimize ligament balance and implant positioning. During surgery, this can offer continuous feedback to ensure soft tissue balance. Post-operatively, the tool aids in monitoring soft tissue healing and adaptation, enhancing patient recovery and satisfaction. With the potential to reduce revision surgeries and improve surgical outcomes, this technology can represent a significant advancement in precision medicine and personalized healthcare for joint replacement procedures.

1.2 Objectives and Organization of the Dissertation

This PhD project is carried out in collaboration (IDN/19/033) with UZ Leuven. The overall aim of this IDN project has been to bring the necessary know-how present at KU Leuven together to enable knee assessment based on novel flexible ultrasound transducer (PMUT) technology. More specifically, the original objectives of this project were: 1. Develop a flexible ultrasound matrix array transducer building upon the ESAT-MNS piezoelectric micromachined ultrasound transducer (PMUT) technology. 2. Develop algorithms to reconstruct volumetric ultrasound images of the knee at high spatiotemporal resolution using this conformable array. 3. Develop algorithms for robust quantitative measurements on these images (i.e. collateral ligament strain). 4. Technically validate the developed monitoring tool.

	Substrate	Piezo material	Membrane Diameter (µm)	Membrane Thickness (µm)	Array Distribution	Pitch (mm)	Characterization studies	Frequency (kHz) (%bandwidth)	Sensitivity (nm/V)	Bending Radius (mm)	Proposed Application	Author (et al.), Year
PMUT	PI	PVDF	750	60	Single element with 3 x 3 cells		In-air transmit, receive function	161	~5	~5	Rangefinding	Liu, 2021
	PI	PVDF	700	80	Two element		Hydrophone, underwater pulse-echo	150 in water	9.3 Pa/V at 12.5 cm		ToF based sensing	Su, 2024
	PI	AlN	250	1.2			LDV, impedance	2580	30 (k=1.42%)			Sun, 2018
	Polymer epoxy based	PVDF	480	16	64 x 64 row-column	0.625	LDV, microphone	400	0.14 Pa/V at 1 cm		Haptics	Halbach, 2019
	PI	PVDF		20	300+ cells annular		LDV, dielectric, hysterisis	66	~2.4			Peters, 2019
	PI	PZT	400	1			Impedance, hysteresis	36.8				Liu, 2018
	Silicon-PDMS	PZT	700	50	16 x 1	1.1	Impedance, hysteresis and hydrophone	700		5	Brain Stimulation	Lee, 2017
	Silicon	PZT	410	7	Single element with 3 x 3 cells	0.49	LDV	426 (1%)	4500	1		Sadeghpour, 2020

Summary of flexible PMUTs

	Substrate	Gap (µm)	Membrane Diameter (µm)	Membrane Thickness (µm)	Array Distribution	Pitch (mm)	Characterization studies	Frequency (kHz) (%bandwidth)	Vop (V)	Bending Radius (mm)	Proposed Application	Author (et al.), Year
CMUT	Silicon				128 x 1	0.375	Underwater pulse-echo and phantom	4000 (125 %) in water		40	**Demonstrated Abdominal imaging**	Wong, 2003
	Polymer-based	5	140	5	5 x 5 elements with 478 cells each	0.7	In-air pulse-echo	1000	120 VDC+16Vpp AC	2	Imaging	Chang, 2007
	PET	2	140	5	72 elements with 416 cells each	0.15	In-air pulse-echo	880	100 VDC + 300 Vpp AC	40	in display panels	Pang, 2017
	Ecogel Epoxy				192 X 1		Impedance, hydrophone, underwater pulse-echo	10700 (105%) in water		8.5	Endocavity imaging	Caronti, 2008
	PDMS	1	160	10	Single element with 2500 cells	0.2	Impedance	200				Shi, 2012
	PI	0.7	80	9.3	32 x 1 elements with 540 cells each		Impedance, hydrophone, underwater pulse-echo	4000 (75 %)	50 VDC + 30Vpp AC	30	Musculoskeletal imaging	Omidvar, 2022
	PI	0.35	50	2.5	Single element with 7 cells		LDV	4800	80 VDC, 30 nm/V	1	In implanted devices	Lucarini, 2021
	Silicon-PDMS	0.15	35*140 rectangular	1.83	16 x 16	0.25	Impedance	4500	70-100 VDC	0.45	Intravascular Ultrasound	Zhuang, 2008
	Silicon-PDMS	0.25	40	1.5	32 x 32 row-column	0.4	LDV, hydrophone	4500	60 VDC	10	Imaging	Chen, 2016

Summary of flexible CMUTs

Table 1.1: Quantitative summary of reported flexible MUTs.

The PhD project is aligned with the first objective and hence broadly the topic has been decided as 'Development of 2D flexible PMUT array technology for ultrasound imaging'. After studying requirements from the application side, concrete transducer specifications are iteratively defined and screened for technical feasibility and consistency with the overall aim of the platform. This has resulted in the following specifications: 1) 1.5 - 8 MHz center frequency and 50-100% relative bandwidth, 2) Output pressure of 250-500 Pa/V per channel at 1 cm, Receive sensitivity of 0.2-0.5 mV/kPa, combining both yields round-trip channel sensitivity (FOM) of $>$ 50 µV/V at 1 cm 3) Flexible and reliable with up to 2 cm bending radius. Note that round-trip channel sensitivity is an important figure of merit (FOM) for imaging applications.

As such, at first, a 128x1 rigid linear PMUT array was developed by Dr. Sina Sadeghpour in June '21 to prove the possibility of ultrasound imaging with silicon-on-insulator (SOI) technology [35, 90]. This array was fabricated based on SOI wafers. Fig. 1.8 shows a microscopic image of the array as well as the associated ultrasound imaging results. It has a center frequency of 1.5 MHz, 110% -6dB bandwidth, an output pressure response of 480 Pa/V at 3cm, and a receive sensitivity of 0.2 mV/kPa. The images validate that PMUTs fabricated by SOI wafers are a promising technology for medical imaging and hence, the characterization results of this array helped in coming up with the specifications required by the PMUTs to be developed in this thesis. However, SOI wafers are rigid and thus impossible to accommodate flexibility. Nevertheless, this technology development, and experience laid a foundation to further expand the research domain to flexible PMUTs.

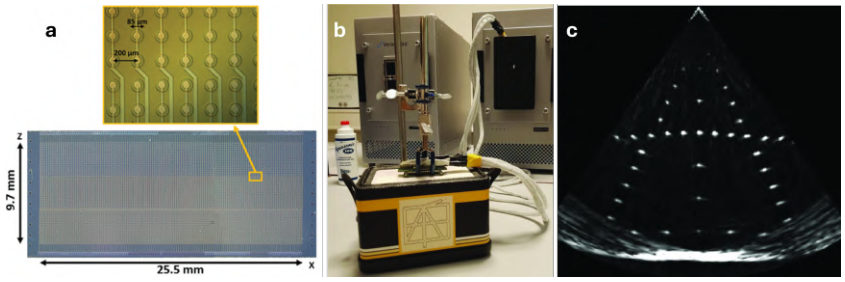

Figure 1.8: Already established rigid SOI based linear PMUT array technology in the ESAT-MNS: a) Array design, b) Imaging experiment with CIRS phantom and c) ultrasound image obtained.

Based on the state of the art and developments in our group, a polymer-based approach is chosen for my PhD project by taking the benefit of bendability and electronics integration while improving the device performance with novel

design and fabrication methods. This alternative fabrication approach is based on a conventional silicon substrate with polyimide membranes which allows the fabrication of flexible as well as rigid PMUTs. A key advantage of the alternatively developed technology is that it obviates the need for expensive SOI wafers. The PZT solution is prepared in-house and is deposited by a sol-gel process. The SOI-free process and custom-made PZT solution for depositing PZT thin films have resulted in low-cost fabrication.

For medical imaging applications, 2D ultrasound arrays allow for real-time volumetric imaging in 3D space which is beneficial for applications, such as cardiac imaging, obstetrics, and musculoskeletal imaging. Keeping these broader aspects in mind, the next generation focused on the development of a 2D array. 2D arrays can be designed with either a fully addressed scheme [91] or a row-column (RC) addressing scheme [92]. In comparison with the fully addressed arrays, for which there is a dedicated pad for accessing individual elements, RC-addressed arrays can be designed with a compact form factor, as they can achieve a high density of elements in a small footprint due to fewer interconnect lines. The fabrication processes developed in the PhD project enabled the realization of novel fully addressed and RC-addressed 2D array designs in rigid and flexible formats, for ultrasound imaging.

1.3 Oraganization of the Dissertation

This chapter presented PMUT theory and state of the art for the flexible PMUTs. Since piezoelectric thin film is at the heart of PMUT, its development is outlined in the following chapter, i.e. chapter 2. In chapter 3, the theory of PMUT is validated with a simple but novel polyimide-on-silicon-based design concept for the rigid fully addressed 2D PMUT array. Following that, PMUT fabrication is introduced and characterization results are presented. Chapter 4 presents a flexible analogue of the 2D fully addressed array design. The top-down fabrication used for realizing flexible PMUT on polyimide and alternative SU8 substrate is explained along with preliminary characterization results. In the following, chapter 5, a different design idea, row-column (RC) addressing, is introduced and rigid PMUT arrays on conventional silicon as well as SOI substrate are presented along with the fabrication and characterization results. The subsequent chapter, chapter 6, describes its flexible analogue, flexible RC PMUTs on a polyimide substrate. In addition to fabrication, it discusses detailed characterization, waterproof packaging, and electronics integration with the verasonics transceiver. Chapter 7 demonstrates imaging experiments and results with the rigid RC-addressed PMUT technology. Chapter 8 concludes the thesis by highlighting the most significant achievements and future work directions.

Chapter 2

Material Development and Characterization

PZT thin films are widely used for piezo mems applications because of their excellent piezoelectric and dielectric properties [93]. In the case of sol-gel thin films, properties depend on stock solution preparation and thin film deposition procedures as demonstrated by various reported studies [94,95]. In this chapter, the intricacies of PZT thin-film process development, such as PZT solution preparation, deposition process, and characterization results are discussed. The characterization of the piezoelectric coefficient is carried out in collaboration with aixACCT Systems (Aachen). The developed sol-gel route described in this chapter is used in the fabrication of all 2D PMUT arrays described in the thesis. First, the basics of piezo-electricity and the rationale for the material section are discussed before getting into actual experiments carried out.

2.1 Basics of Piezoelectricity

The piezoelectricity or piezoelectric effect refers to the generation of electric charges on the surface of specific insulators when mechanical stress is applied. Conversely, it can also be described as the generation of mechanical strain in these materials under exposure to an electric field. The linear electrical behavior is described by the $D = \varepsilon E$, where D is the electric displacement vector, E is the electric field vector, and ε is the permittivity matrix. Whereas Hooke's Law for linear elasticity is given by $S = sT$, where S is the strain tensor, T is the stress tensor, and s is the compliance matrix. Piezoelectricity is a linear

electromechanical phenomenon between the electrical and the mechanical states. The strain-charge form below combines mechanical and electrical behaviors where d is the piezoelectric strain coefficient matrix and note that the subscripts indicate the parameters held constant during measurement. For example, compliance coefficients are measured under a constant electric field.

$$\begin{cases} S = s_E T + d^t E \\ D = dT + \varepsilon_T E \end{cases} \tag{2.1}$$

The same strain-charge relations for tetragonal PZT C_{4v} in the matrix form:

$$\begin{pmatrix} S_1 \\ S_2 \\ S_3 \\ S_4 \\ S_5 \\ S_6 \end{pmatrix} = \begin{pmatrix} s_{11} & s_{12} & s_{13} & 0 & 0 & 0 \\ s_{12} & s_{11} & s_{13} & 0 & 0 & 0 \\ s_{13} & s_{13} & s_{33} & 0 & 0 & 0 \\ 0 & 0 & 0 & s_{44} & 0 & 0 \\ 0 & 0 & 0 & 0 & s_{55} & 0 \\ 0 & 0 & 0 & 0 & 0 & s_{66} \end{pmatrix} \begin{pmatrix} T_1 \\ T_2 \\ T_3 \\ T_4 \\ T_5 \\ T_6 \end{pmatrix} + \begin{pmatrix} 0 & 0 & d_{31} \\ 0 & 0 & d_{32} \\ 0 & 0 & d_{33} \\ 0 & d_{24} & 0 \\ d_{15} & 0 & 0 \\ 0 & 0 & 0 \end{pmatrix} \begin{pmatrix} E_1 \\ E_2 \\ E_3 \end{pmatrix}$$

$$\begin{pmatrix} D_1 \\ D_2 \\ D_3 \end{pmatrix} = \begin{pmatrix} 0 & 0 & 0 & 0 & d_{15} & 0 \\ 0 & 0 & 0 & d_{24} & 0 & 0 \\ d_{31} & d_{32} & d_{33} & 0 & 0 & 0 \end{pmatrix} \begin{pmatrix} T_1 \\ T_2 \\ T_3 \\ T_4 \\ T_5 \\ T_6 \end{pmatrix} + \begin{pmatrix} \varepsilon_{11} & 0 & 0 \\ 0 & \varepsilon_{22} & 0 \\ 0 & 0 & \varepsilon_{33} \end{pmatrix} \begin{pmatrix} E_1 \\ E_2 \\ E_3 \end{pmatrix} \tag{2.2}$$

The constitutive equations can also be expressed in the stress-charge form where c is the stiffness matrix (inverse of compliance matric) and e is the piezoelectric stress coefficient matrix.

$$\begin{cases} T = c_E S - e^t E \\ D = eS + \varepsilon_S E \end{cases} \tag{2.3}$$

Additionally, there are two more less commonly used formats, strain-voltage and stress-voltage, respectively. For more details, the reader is referred to [96].

As PZT material exhibits transverse isotropy (4mm crystal symmetry), the compliance matrix (s) can be simplified as [96]:

$$s = \begin{pmatrix} \frac{1}{E_1} & -\frac{\nu_{12}}{E_1} & -\frac{\nu_{13}}{E_1} & 0 & 0 & 0 \\ -\frac{\nu_{12}}{E_2} & \frac{1}{E_2} & -\frac{\nu_{13}}{E_2} & 0 & 0 & 0 \\ -\frac{\nu_{31}}{E_3} & -\frac{\nu_{31}}{E_3} & \frac{1}{E_3} & 0 & 0 & 0 \\ 0 & 0 & 0 & \frac{1}{2G_{13}} & 0 & 0 \\ 0 & 0 & 0 & 0 & \frac{1}{2G_{13}} & 0 \\ 0 & 0 & 0 & 0 & 0 & \frac{1}{2G_{12}} \end{pmatrix} \tag{2.4}$$

Here, E_i is the Young's modulus in the i-direction, ν_{ij} is Poisson's ratio for strain in the i-direction due to stress in the j-direction and G_{ij} is shear modulus in the ij plane. Piezoelectric strain coefficients d can be converted to piezoelectric stress coefficients e by multiplication with stiffness matrix.

For piezoelectric thin films, such as PZT, the strain along the in-plane directions is identical between the film and the substrate to which the film is clamped at its interface. However, the thin film is unrestricted in the perpendicular direction, resulting in zero stress along the z-axis. In the case of a thin film attached to a significantly thicker substrate (or a passive layer, as seen in PMUTs), applying an electric field in the z-direction induces negligible in-plane strains. Instead, in-plane stresses and an out-of-plane strain are generated. The strain-charge relations hence simplify to:

$$S_1 = (s_{11}^E + s_{12}^E)\sigma_1 + d_{31}E_3 = 0 \tag{2.5}$$

$$S_3 = 2s_{13}^E\sigma_1 + d_{33}E_3 \tag{2.6}$$

Finally, it is convenient to define $e_{31,f}$ and $d_{33,f}$ as following [97].

$$e_{31,f} = \frac{d_{31}}{s_{11}^E + s_{12}^E} \;\; \& \;\; d_{33,f} = d_{33} - 2s_{13}^E \frac{d_{31}}{s_{11}^E + s_{12}^E} \tag{2.7}$$

This is because $e_{31,f}$ is a multiplier of the electric field in the z-direction to obtain average in-plane stress, and $d_{33,f}$ is a multiplier of the electric field in the z-direction to obtain out-of-plane strain for the piezo-electric thin film used in piezo-MEMS devices, including PMUTs [98–100].

As a note, to define a material like PZT, although symmetry reduces the number of independent parameters, 13 parameters are still needed- 6 stiffness coefficients, 3 piezoelectric coefficients, 2 dielectric constants, and apart from these, density and mechanical Q factor. Here, the piezo-electric material development is attempted and one of the most important parameters in the context of PMUTs, $e_{31,f}$, is characterized.

2.2 Piezo-electric Material Comparison for PMUTs

The selection of materials for piezoelectric transducers is crucial, especially for applications like ultrasonic imaging. Actuation sensitivity is proportional to the piezoelectric constant e_{31}. For receiver applications, the sensitivity is described by the coefficient $e_{31}/\epsilon_0\epsilon$. Imaging involves transmission as well as reception of ultrasound where the figure of merit (FOM) in material selection is quantified multiplication of the above two parameters, round-trip efficiency, $e_{31}^2/\epsilon_0\epsilon$. Here, ϵ_0 is the permittivity of free space (8.854×10^{-12} F/m).

Material	PZT	KNN	AlScN	PVDF
Piezoelectric constant (e31) [C/m^2]	-13	-8	-1.5	-1
Relative permittivity (ϵ)	850	450	13	12
Roundtrip piezoelectric efficiency [Gpa]	22	16	19.5	11.3

Table 2.1: State of the art piezo-electric thin films used in PMUTs

Table 2.1 indicates that PZT has a better round-trip efficiency for imaging applications, among the most popular piezo-electric materials employed for PMUTs. Moreover, aluminum scandium nitride (Al-ScN) is not yet common due to processing challenges and mechanical limitations and has a lower piezoelectric constant, resulting in a poor transmitter. potassium sodium niobate (KNN) is not sufficiently mature either. PVDF, while flexible and lightweight, also has a much lower piezoelectric coefficient, making it less suitable for high-performance imaging applications. Note that, for flexible PMUTs, high acoustic pressure generation is the first priority in order to be able to receive the echo back for imaging, where PZT is an obvious winner. While its dielectric constant is much higher than that of AlScN and PVDF, making it a bad choice for receiving ultrasound, PZT strikes a balance between performance, cost, and processing maturity, making it the material of choice in many cases.

2.3 PZT Sol-Gel Process

2.3.1 Solution Preparation

The choice of the precursors, process parameters, and sequence are inspired by the cited literature [101–103]. For PZT solution Preparation, lead acetate (referred to as Pb precursor), zirconium propoxide (Zr precursor), (70 wt.%

solution in 1-propanol) and titanium isopropoxide (Ti precursor), 97% are used as precursors. Acetic acid, acetylacetone, and 1,3-propanediol are used as stabilizers and additives whereas alcohol-based solvents are used to adjust the solution molarity. The chemicals were mainly purchased from Sigma Aldrich.

To prepare the PZT stock solution, first acetylacetone, Zr, and Ti precursors are refluxed at 80 °C for 30 min in beaker 1 with the precursors in stoichiometric amounts (acetylacetone stabilizing the aforementioned precursors [101]). In beaker 2, Pb precursor taken in excess of the stochiometric amount is refluxed with acetic acid (5 times the millimoles of PZT) for 10 min at 105°C. The reflux chemistry is reported in [102]. It is cooled down to 80°C. The contents from both the beakers are mixed in another beaker. While mixing, 1,3-propanediol is added (twice the millimoles of PZT) for sol stability. The solution is diluted to 0.4 M with the solvent and optionally, PVP (polyvinylpyrrolidone, Sigma-Aldrich) polymer is added to relax the mechanical stress in the film.

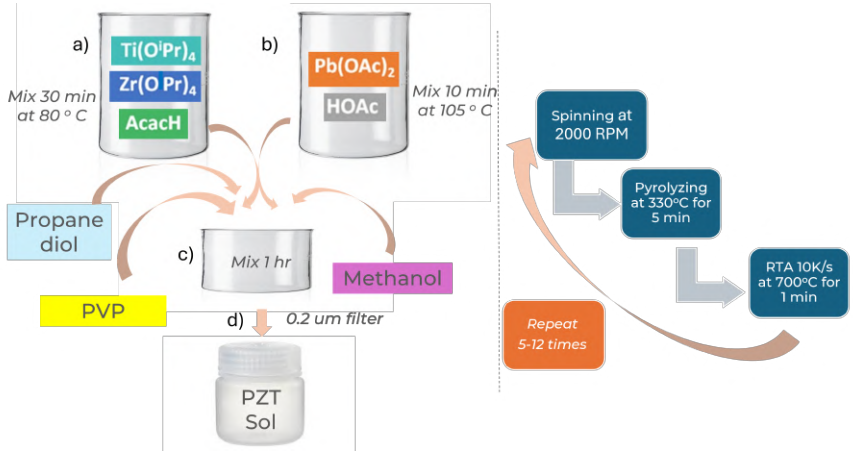

Figure 2.1: Recipe of making PZT solution: a) Zr and Ti precursors refluxed with Acetylacetone b) Lead precursor refluxed with acetic acid c) These two solutions are mixed followed by adding a sol stabilizer and solvent. The contents are allowed to be mixed thoroughly for an hour. d) The Solution is filtered in a stock bottle. On the right, **Procedure of PZT thin film deposition**: Spin coating, pyrolysis, and RTA are repeated. * Spin coating and pyrolysis steps can be additionally repeated before RTP for dilute solutions.

2.3.2 Thin Film Deposition

PZT thin film deposition requires the preparation of a seed layer on a substrate. For the preparation, a silicon wafer is first cleaned with Piranha and BHF. Then the wafer is wet oxidized in the oxidation oven at 1100°C for 35 min. This resulted in 300 nm of SiO_2 on both sides of the wafer. Next, the 200 nm Pt bottom electrode is deposited on a 10 nm Ti adhesion layer by RF sputtering. Pt serves as a seed layer for the PZT deposition process [95]. The prepared solution was deposited on top of Pt bottom electrode. The deposition involves spin coating, pyrolysis, and rapid thermal annealing (RTA) with the parameters described in Fig. 2.1. The sequence of the above procedures is repeated 5-12 times as per the film thickness requirements. Thickness per layer is about 150-190 nm.

2.4 Fine Tuning the Sol-gel Process

2.4.1 Effect of Changing Solvents

Changing the solvent alters the properties of the deposited thin film [104]. It also changes the viscosity of PZT solution to be spin coated and resulting film thicknesses. This affects thin film stress and cracking behavior in films. Moreover, solvent selection also affects homogeneity during solution preparation and the storage of solution in the freeze. Alcohol-based solvents are tried for the solution preparation. During the experiments, the PZT solution with isopropanol solvent precipitated during the final 1 hr mixing. Whereas the one with ethanol passed the mixing phase but failed in the freeze after 2 days due to the appearance of the precipitate. Methanol solvent turns out to be the best choice for solution preparation and storage and is finalized.

2.4.2 Effect of Solvent Dilution

Another practically important consideration in the development of a stock solution recipe is solvent dilution. The solvent dilution or content (which can be expressed in milliliters per millimole of PZT or inversely, molarity) defines the viscosity of stock solution and in turn the thickness after spin coating. After a certain threshold thickness, the film starts cracking due to excessive stress. Two molarities are considered in the study, 0.8 M and 0.4 M, while the spin coating speed is maintained at 2000 RPM. The 0.8 M solution has resulted in a 300 nm film which cracked after RTA (Fig. 2.2a). Other 0.4 M is chosen

as concentration for further experiments which resulted in 150-190 nm film thickness per layer. Typically, per layer film thickness less than 250 nm has less chance of cracking.

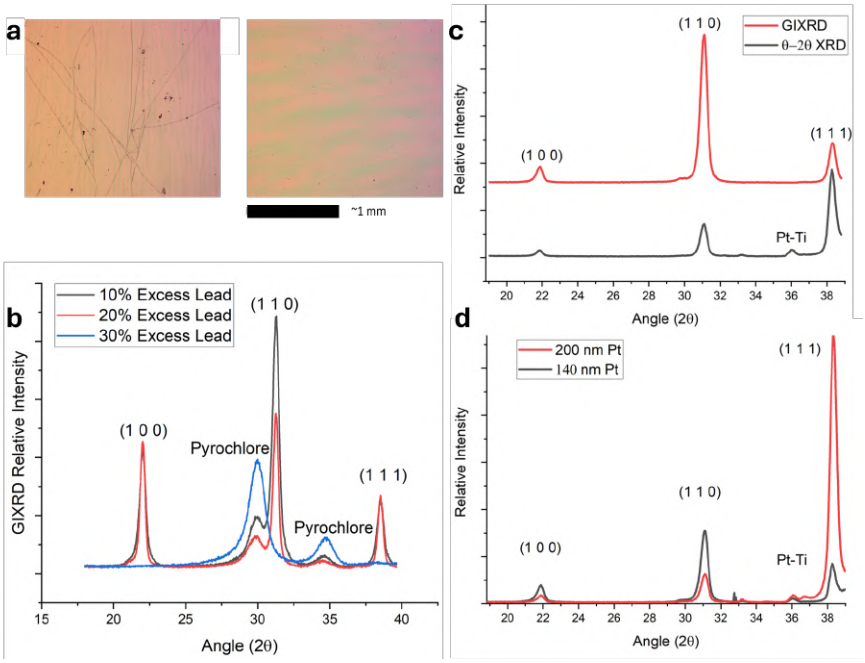

Figure 2.2: PZT thin film process development: a) PZT deposited Using solutions with 0.8M (left) and 0.4M (right). b) Effect of excess lead percentage evident from GIXRD of PZT deposited Using solutions with 10, 20, & 30 % excess lead. c) XRD of PZT deposited using a solution with 15 % excess lead. d) XRD of PZT deposited on substrates with 140 nm and 200 nm Pt seed layer.

2.4.3 Effect of Excess Lead Percentage

Excess lead is always added (5-30 %) while making PZT solution as lead evaporates during the solution preparation procedure. Lack of lead or excess lead in PZT stoichiometry leads to unwanted phases like pyrochlore in addition to the desirable perovskite [105]. Hence, the excess lead percentage needs to be finalized. For this, solutions containing 10, 20, and 30 excess lead percentages were prepared and deposited as a thin film. Grazing incidence XRD of these films was studied as the unwanted phases are easily detectable on the surface [106].

Small pyrochlore amounts are observed between 10 and 20 % (Fig. 2.2b). Hence, a solution with 15% excess lead is prepared and has led to pyrochlore-free $\theta - 2\theta$ XRD (Fig. 2.2c).

2.4.4 Effect of Pt Seed Layer Thickness

Platinum (Pt) seed layers are predominantly deposited with a [111] orientation prior to PZT deposition due to the intrinsic properties of Pt and its interaction with PZT. Pt naturally favors this orientation because this plane has the lowest surface energy among its crystallographic planes, leading to a more stable and energetically favorable configuration. This orientation also provides a lattice-matched structure that promotes the growth of high-quality [111] PZT films with desirable ferroelectric and piezoelectric properties. Even if the PZT is desired in a different orientation, the Pt [111] layer serves as a consistent base for an additional seed layer, controlling the PZT orientation. Additionally, the [111] orientation of Pt enhances its resistance to oxidation and maintains adequate conductivity, which is crucial for the PZT-based device performance.

Strong [111] orientation of the Pt seed layer is confirmed by the following. Two samples are prepared with Pt thicknesses of 140 nm and 200 nm respectively. The one with thicker Pt has resulted in a strong [111] orientation of PZT and the other sample has a mixed orientation ([110] dominant) as seen in Fig. 2.2d. Hence, 200 nm is chosen as the suitable thickness of the Pt seed layer. Moreover, consistency during the Pt seed layer sputtering process is of paramount importance in PZT processing and can be ensured with a precise sputtering recipe and setup (for instance, maintaining target-sample distance).

2.4.5 Effect of Adding Polymer

Even after these development steps, the PZT deposition is found to be not consistent and has resulted in cracked films, sometimes. The inconsistency can result from the irregularities during the Pt seed layer sputtering process, stock solution preparation, and PZT deposition. Hence, to mitigate these problems, reducing the overall mechanical stress levels in this process is the way forward. Hence, a so-called porogen, PVP powder is added to the solution. Adding PVP to the sol-gel process for PZT films allows for the creation of thicker films—up to twice as thick—without causing cracks, which is a significant advantage in fabrication [103]. However, as more PVP is added, the porosity of the film increases, which lowers the dielectric constant (Note that, porosity refers to the presence of PVP molecules distributed throughout the PZT matrix, leading to a PZT-PVP composite material) and can also degrade PZT ferroelectric

properties. As crack-free film is a requirement for the proper functioning of PMUT device, PVP is incorporated in the solution with the content set to be 0.05 grams PVP/millimole (mM) of PZT (î5 wt% as suggested in [103]).

2.5 Thin Film Characterization

2.5.1 Sample Preparation with the Developed Recipe

First, the substrate is prepared with the bottom Pt electrode. PZT solution is then prepared with the developed recipe (15% excess lead, 0.4 M solution in a methanol solvent, and 0.05 gm PVP per mM of PZT) 1 µm film is prepared with 6 deposition cycles of spin coating at 2000 RPM, pyrolysis at 330°C for 5 min, and RTA at 700 °C for 1 min in the presence of oxygen. 2 µm film is also prepared with just by having 12 deposition cycles.

PZT is patterned using wet etching to access the bottom electrode. 3 µm thick positive photoresist s1818 (microresist technologies) served as an etch mask for patterning. The wet etchant constituents are $1BHF : 2HCl : 4H_2O : 0.7NH_4Cl$ by weight and are adapted from [107]. The etch rate is around 10 nm/s. After PZT patterning, the top Pt electrode is sputtered and patterned by the liftoff method. LOR10B (microresist technologies) and s1818 are used as lift-off masks for patterning.

2.5.2 DBLI Method for d_{33} and e_{31} Characterization

The film is then characterized with the DBLI system at Aixacct (Aachen). DBLI is a proven technique for the measurement of the out-of-plane piezoelectric coefficient. Basically, DBLI measures the net thickness expansion, i.e., the thickness expansion in the piezoelectric due to piezo-electricity and the expansion in the substrate which is a mechanical phenomenon. Out-of-plane coefficient $d_{33,f,\text{meas}}$ is calculated then per unit voltage. However, the $d_{33,f,\text{meas}}$ values obtained are electrode size dependent due to substrate contribution [108]. The dependence of electrode size and substrate thickness ratio r, on the $d_{33,f,\text{meas}}$ can be used for the measurement of $d_{33,f}$ and $e_{31,f}$. The measured coefficient $d_{33,f,\text{meas}}$ is influenced by substrate properties as follows [109]:

$$d_{33,f,\text{meas}} = d_{33,f} + f(r)s_{13,s}e_{31,f} \tag{2.8}$$

Here $f(r)$ is the geometry factor and $s_{13,s}$ is the substrate compliance coefficient. The geometry factor $f(r)$ captures the effects of in-plane and out-of-plane stresses in the substrate and is calculated as:

$$f(r) = \frac{\int \left(2T_{1,s}s_{13,s} + T_{3,s}s_{33,s}\right)\, dz}{\int T_{1,p}\, dz} \tag{2.9}$$

Here, $T_{1,s}$ and $T_{3,s}$ are the in-plane and out-of-plane stresses in the substrate,$s_{13,s}$ and $s_{33,s}$ are the substrate compliance coefficients, $T_{1,p}$ is the in-plane stress in the piezoelectric layer. $f(r)$ depends only on the substrate properties and is independent of the piezoelectric film's properties. The geometry factor can be calculated using the finite element method (For further details on its calculation and validation that it is independent of piezo layer properties, the reader is referred to [109]). To isolate $d_{33,f}$ and $e_{31,f}$, measurements of $d_{33,f,\text{meas}}$ are taken for two pad sizes with ratios r_1 and r_2. Solving gives:

$$e_{31,f} = \frac{d_{33,f,\text{meas}}(r_1) - d_{33,f,\text{meas}}(r_2)}{f(r_1) - f(r_2)} \cdot \frac{1}{s_{13,s}} \tag{2.10}$$

$$d_{33,f} = \frac{f(r_2)d_{33,f,\text{meas}}(r_1) - f(r_1)d_{33,f,\text{meas}}(r_2)}{f(r_1) - f(r_2)} \tag{2.11}$$

2.5.3 Characterization Results and Discussion

The obtained results with 1 µm PZT are shown in Fig. 2.3. An important observation from the figure is that the PZT properties start saturating between 5-10 V. Hence while applying the film in device applications, a typical DC bias of 5-10 V should be sufficient. The coercive field is about 6.6 V/µm or 66 kV/cm whereas remnant polarization is about 15 $\mu c/cm^2$. Wafer maps of $d_{33,f}$ (Fig. 2.3d) are obtained to check the uniformity across arrays. $d_{33,f}$ and $e_{31,f}$ are about 60 pm/V and 4 C/m^2 respectively. Unfortunately, the coefficients are 3 fold lower compared with state-of-the-art [108]. One of the main reasons for the low piezoelectric coefficients is the absence of [100] orientation (at least 2-3 fold improvement is expected by achieving [100] orientation). Moreover, the PVP content also alters the PZT quality and coefficients. The breakdown voltage is obtained to be around 100 V. The dielectric constant of the PZT film characterized is about 1000 and reduces up to 600 in the presence of 20 V bias.

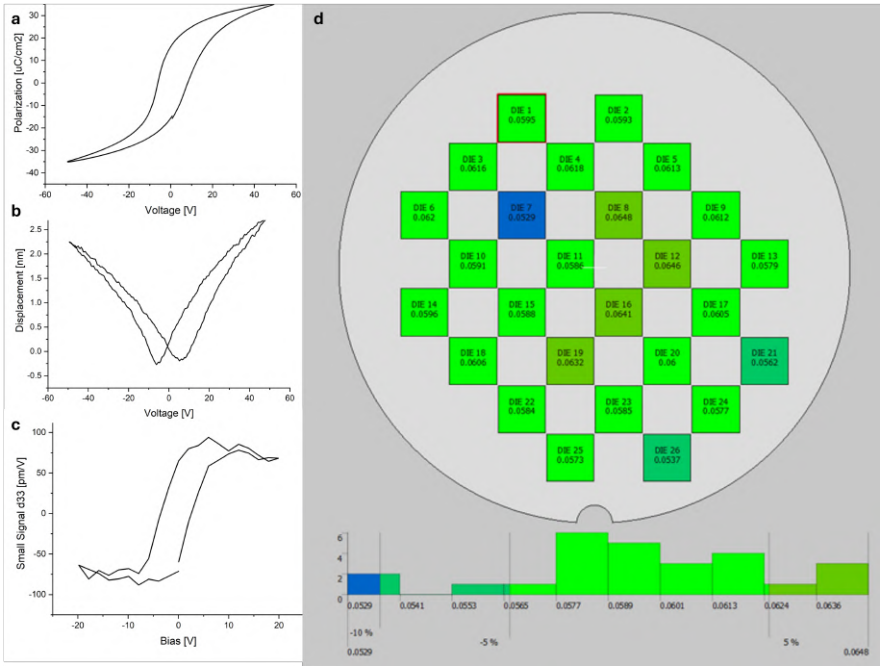

Figure 2.3: 1 µm PZT thin film DBLI characterization: Large signal hysteresis loops: a) Polarization-Voltge (P-E) b) Displacement-Voltage (s-E). c) small signal $d_{33,f}$ vs bias voltage. d) Wafer map of small signal $d_{33,f}$.

Fig. 2.4 shows the wafer maps of e_{31}. It shows an improvement of e_{31} with PZT thickness. The other results with 2 µm PZT are also obtained (not shown here). A shift is clearly seen with all the values. The coercive field is about 9 V/2 µm or 45 kV/cm whereas remnant polarization is about 14 $\mu c/cm^2$. $d_{33,f}$ and $e_{31,f}$ are about 65 pm/V and 5 C/m^2 respectively. The dielectric constant of the PZT film characterized is about 1700 and reduces up to 1000 in the presence of 20 V bias. Both 1 µm and 2 µm PZT will result in similar values as capacitance is directly proportional to the dielectric constant and inversely proportional to thickness. Now, the PZT thickness choice during device fabrication depends on the membrane design, passive layer thickness, and residual stresses, affecting transmit-receive sensitivities.

Comparison with the state of the art suggests scope for 2-3 times improvement in the piezoelectric coefficients [36, 39, 93]. FOM for the developed material with these values is about 2.5-3 GPa (5-10 times lower than state-of-the-art). This suggests that, if state-of-the-art [100] oriented material is used, the device

FOM can also improve 5-10 times. Note that, the lower coefficients are mainly the result of [111] orientation of the PZT. State-of-the-art PMUTs typically use [100] oriented PZT with higher piezo-electric coefficients [92].

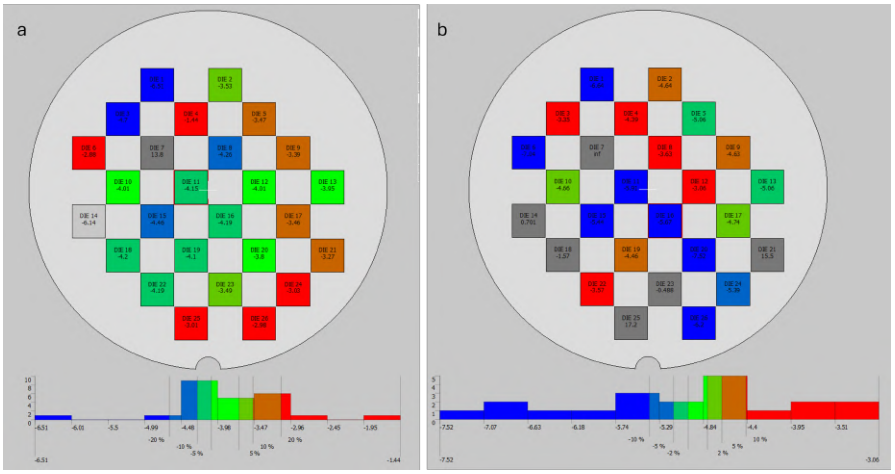

Figure 2.4: PZT thin film e_{31} wafer map: a) 1 µm and b) 2 µm film.

2.6 Conclusion

PZT sol-gel preparation and deposition recipes are developed. During in-house preparation, methanol turned out as the best solvent in terms of solution stability and resulted in the desired coating parameters. 0.4 M concentration has resulted in 160-170 nm single-layer coating thickness. The excess lead percentage was set to 15% percent to minimize the pyrochlore phase. The PVP porogen concentration is experimentally tuned as 0.05 gm/mM of PZT to reduce the film stress and crack formation, in order to obtain a stable 1 µm PZT film after 6 coating steps. [111] orientation of the film is confirmed by XRD. This is attributed to the strong [111] orientation of 200 nm thick Pt substrate. The film is characterized by DBLI measurements. The coercive field is about 7V/µm or 70 kV/cm whereas remnant polarization is about 15 $\mu c/cm^2$. $d_{33,f}$,e_{31}, breakdown voltage and dielectric constant of the film are about 60 pm/V, 4 C/m^2, 100 V, and 1000 respectively. FOM for the developed material with these values is about 2.5-3 GPa. A comparison with the state of the art suggests there is a scope of 2-3 times improvement of piezoelectric coefficients (5-10 times FOM at material level) which in turn suggests a need for [100]-oriented PZT development.

Chapter 3

Low Cost Rigid PMUT Technology

This chapter is adapted from a previously published article: Joshi et al. Polyimide-On-Silicon 2D Piezoelectric Micromachined Ultrasound Transducer (PMUT) Array. Sensors 2023, 23, 4826 [110].

3.1 Background

In this chapter, a 2D PMUT array on a conventional silicon wafer is described. The device is cost-effectively (No SOI wafer) fabricated with a polyimide membrane and characterized without compromising on resonance frequency. SOI technology is a mature and convenient PMUT fabrication technique because of the silicon device layer with a desired thickness and buried oxide etch stop during backside etching, which makes it easy to realize the membranes [62], however, SOI wafers are costlier compared with conventional silicon wafer.

The fabrication process based on polyimide membranes, described here, is much simpler compared to the reported processes on conventional silicon wafers. Previously reported PMUT fabrication processes on conventional silicon wafers include back-side sloped sidewall cavity etching [111], front-side isotropic cavity etching with a via hole [112], sacrificial layer etching [113], etc. These processes lack a passive layer in the membrane, which is required to keep the piezo layer away from the neutral axis. A recent method based on hydrogen annealing [114] has a passive layer, but it is a relatively more complicated fabrication process.

The rigid-flex design with polyimide-PZT membrane on a silicon wafer can be seen as a step towards a fully flexible PMUT. In the following, PMUT fabrication is briefly described. Then, the material and electrical characterizations of PZT thin film as well as PMUT are explained. Air and water are the acoustically closest environments where PMUTs operate. Hence, the operation of the PMUTs is evaluated in-air as well as underwater, which can help optimize the design and performance of the transducer for specific applications in the future. The evaluations include LDV, and hydrophone measurements supported by theoretical calculations. Note that there are two crucial factors regarding transducer arrays that are not addressed much in the literature and are touched upon here: (i) interconnect design to address each individual element (full addressing) in 2D arrays; and (ii) inter-element crosstalk.

3.2 Fully Addressed 8×8 Rigid PMUT Array Design

Our proposed single PMUT element consists of a polyimide passive layer in the membrane situated above the top electrode and the 1 µm thick active piezoelectric (PZT) layer, as shown in Fig. 3.1a (top view image of the array elements are in Fig. 3.1d where circular parts are top electrodes from the PMUT elements). Note that the polyimide passive layer arrangement in the membrane is different from the usual silicon passive layers in SOI PMUT technology. In an SOI PMUT, the passive silicon device layer of the SOI wafer is below the active piezoelectric layers. Another thing to note is that an SOI PMUT's silicon passive layer keeps the neutral axis outside the PZT (the neutral axis should be outside the piezo layer to ensure a good sensitivity [84]), and here, polyimide does the same. Moreover, an advantage presented by this technology is the resonance frequency tunability by means of changing the polyimide thickness.

The underwater resonance frequency is designed to be 1.5–2.5 MHz so that the devices can be used for applications such as ultrasound imaging and consequently, 100 µm is chosen as the diameter of the PMUT membrane, considering around 6-8 µm passive layer thickness, which is compromise 1) to have neutral axis as away as possible from PZT, 2) to not have too much damping and 3) to meet resonance frequency requirement which is confirmed by calculations described in the next section. In the array design, a half-wavelength pitch of 300 µm is chosen to avoid imaging artifacts and the creation of side lobes in the beampattern [29]. A fully addressed 8 × 8 array is designed, resulting in an around 2.4 mm × 2.4 mm aperture size. Fully addressable means that there is a dedicated top electrode pad for exciting each individual PMUT element. This presents a design challenge, especially for 2D array interconnects, as a transducer with m rows and n columns requires m × n interconnect lines for operation. The

proposed novel design of the top electrode interconnects can be seen from microscope images of the fabricated device shown in Fig. 3.1b–d. The area where PMUT elements are located is marked (black outline). Including the interconnects and bond pads, the chip size is 1 cm × 1 cm. This design has limited scalability to increase element count by reducing the line width and drawing more lines between two adjacent top electrodes.

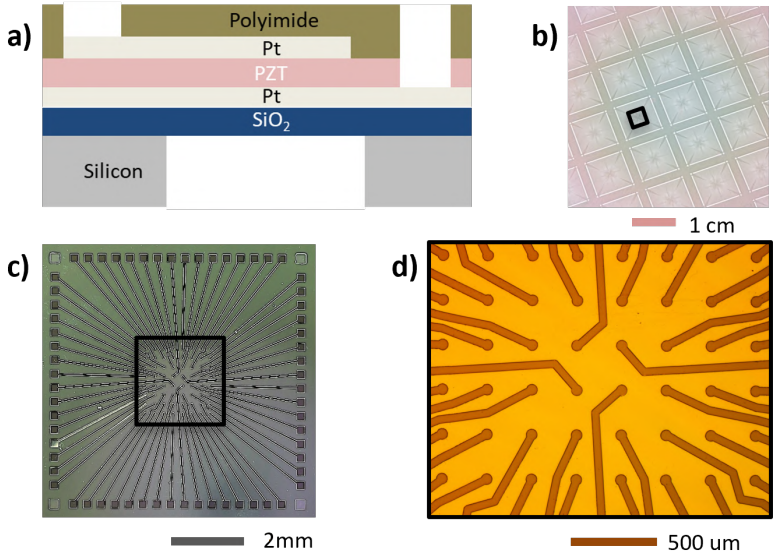

Figure 3.1: Design of a fully addressed 8 × 8 rigid PMUT array: (a) Schematic of a PMUT element (not to scale). The area where PMUT elements are located is marked (black outline). (b) Two-dimensional PMUT array on the wafer. (c) Optical microscope image of the demonstrated 8 × 8 array. (d) Zoomed-in top view where circular parts are top electrodes from the PMUT elements.

An advantage presented by this technology is the resonance frequency tunability by means of changing the polyimide thickness. The resonance frequency of the PMUT in the air is given by Equation (1.1). Basically, increasing the thickness makes the membrane effectively stiffer and increases the resonance frequency. Equation (1.4) shows that the mass of the water medium reduces the resonance frequency in comparison with the air medium. However, the dependence on the layer thickness, t_i, is normally weak (also applies to our case) and follows a $t^{0.5}$ relationship when the lateral dimensions are significantly larger (the second term from the denominator of Equation (1.4) is much larger than 1 in this case). In

essence, the combined effect of both equations is the increase in the underwater resonance frequency with the increase in the thickness of the polyimide layer.

The PMUT resonance frequency underwater is also theoretically calculated using these equations. The values of the used parameters are in Table 3.1. When 6 µm thick polyimide is used, along with 1 µm PZT thin film, the flexural rigidity is calculated to be 740 nN.m, whereas the linear mass density is calculated as 17.12 g/m^2. Using Equation (1.1), the in-air resonance frequency is estimated to be 4.35 MHz. Equation (1.5) is further used to find the underwater resonance at 2.35 MHz. Since 6 µm polyimide resulted in a resonance frequency between 2 and 2.5 MHz, this thickness is used for fabrication. Calculating using a 3 µm polyimide thickness resulted in 2.3 MHz and 1.1 MHz resonance frequencies in air and water, respectively, validating claims regarding resonance frequency tunability.

3.3 PMUT Fabrication

The PMUT fabrication can be divided into four parts as follows. Although a recipe for particular device fabrication described in this chapter is explained next, the same applies to the processes described in later chapters:

3.3.1 Substrate Preparation

The PMUT array device fabrication starts with preparing a (100) silicon wafer. The wafer is cleaned with Piranha and BHF. Then the wafer is wet oxidized in the oxidation oven at 1100°C for 80 min. This has resulted in 500 nm of SiO_2 on both sides of the wafer. This oxide serves as an etch stop in the final DRIE step. Next, the 200 nm Pt bottom electrode is deposited by RF sputtering (100 W RF power, 10 µbar Ar pressure, 70 nm/min deposition rate) along with a 10 nm Ti adhesion layer (200 W RF power, 10 µbar Ar pressure, 60 nm/min deposition rate). Pt serves as a seed layer for the PZT deposition process.

3.3.2 Active Layers' Deposition and Patterning

1 µm PZT thin film is deposited on top of the Pt bottom electrode. The sol-gel process is described at length in the last chapter 2. PZT is patterned at the corner squares (see Fig. 3.1-c) using wet etching to access the bottom electrode. 3 µm thick positive photoresist s1818 (microresist technologies) serves as an etch mask for patterning. The wet etchant constituents are by weight

$1BHF : 2HCl : 4H_2O : 0.7NH_4Cl$ and are adapted from [107]. The etch rate is around 10 nm/s.

After PZT patterning, the top Pt electrode is sputtered and patterned by the liftoff method. 4 µm thick LOR10B (microresist technologies) and 2 µm thick s1818 are used as lift-off masks for patterning. The top electrode diameter is maintained as 70% of the membrane diameter which is the optimized value in PMUT literature [62].

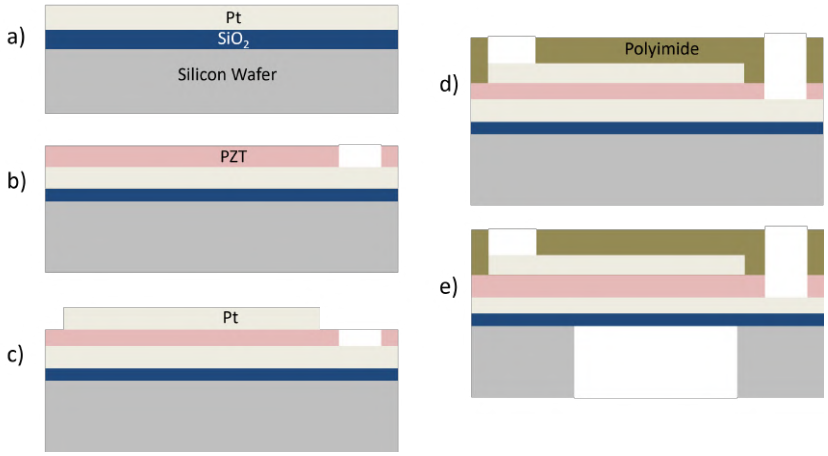

Figure 3.2: Rigid PMUT device fabrication process: (a) Oxide growth followed by deposition of the Pt as the bottom electrode. (b) Deposition and patterning of the PZT layer. (c) Patterning the top electrode. (d) Polyimide passive layer patterning. (e) Realizing the membrane via DRIE.

3.3.3 Passive Layer Deposition and Patterning

Once active layers are prepared, polyimide is deposited to serve as the membrane material. Moreover, this also serves as an insulation to the top electrodes when the device is immersed in water. Polyimide processing is briefly explained next. The PI2611 solution (HD Microsystems) is spun, soft-baked on a hot plate, and cured in a programmable oven. Spin coating RPM of 2500 and 5000 is used for achieving 6 µm and 3 µm layer thickness after curing. For soft baking, the wafer is kept on a hotplate at 90°C. After 1 minute, the hotplate temperature is set to 150°C to ramp up the hotplate temperature. (ramp rate not controlled). After baking for 1 minute at 150°C, the wafer is removed from the hotplate and is cooled down on a cleanroom wipe. For curing, the wafer is hard-baked in a

programmable oven at 350°C for 1 hour. The wafer is loaded and removed at room temperature and the ramp up/down rate is programmed to be 2.5°C/min with a 1-hour dwell step in between ramping.

At this point, backside oxide is removed by a 6 min dip in buffered oxide etch (BOE) as the etch rate is about 100 nm/min. Next, polyimide is patterned to access top and bottom electrode pads (Note that except for pads, the device including top electrodes and interconnects is waterproof). A hard mask has to be used. 50 nm chromium layer is used as a hard mask and is deposited by sputtering (200 W RF power, 3 µbar Ar pressure, 50 nm/min deposition rate) and patterned with photoresist and Cr01 etchant (Microchemicals). The polyimide is etched with oxygen using RIE (100 W RF power, 20 sccm O_2 flow, 150 nm/min etch rate). The chromium is removed using the same etchant.

3.3.4 Final Release Procedures

Next, the wafer backside is patterned with around 30 µm thick Az125nxt (Microchemicals) negative photoresist (Spin coating at 2500 RPM) and silicon etched using deep reactive ion etching (DRIE). After DRIE, Az125nxt is stripped in the MLO-07 stripper (microchemicals). RIE can further be used with the same parameters as used for polyimide etching for 15-30 min to remove all the resist residues. This completes the fabrication of the PMUT. The fabrication process flow is shown step by step in Fig. 3.2.

Material	Function	Thickness (µm)	Young's Modulus (GPa)	Density (Kg/m^3)	Poisson's Ratio	Deposition Method
Polyimide	Membrane passive layer	6	8.5	1420	0.34	Spin coating
PZT	Piezo layer	1	80	7500	0.3	Sol–gel
Pt	Top, bottom electrodes	0.2	168	21400	0.39	RF sputtering
Silicon oxide	Etch stop for DRIE	0.5	70	2200	0.17	Thermal wet oxidation
Silicon	Membrane sidewall	525	140	2330	0.265	--

Table 3.1: Details of the materials used for the rigid PMUT technology

3.4 Characterization Results and Discussion

3.4.1 Material and Electrical Characterization

During fabrication, just after the PZT deposition step, the X-ray diffraction (XRD) pattern of the PZT thin film is obtained, showing (111) – orientated PZT (peak at 38°) without any pyrochlore phase (normally around 29°) (Fig. 3.3a). The sharp peak around 40° is due to platinum (111) and is cut out, as it would otherwise diminish the important PZT peaks.

Next, while analyzing the device electrically, the capacitance of a single PMUT element is measured to be around 2.5 nF. However, note that this also includes the significant contribution of parasitic capacitance due to interconnects, which negatively affect the performance of the PMUT. Furthermore, the impedance of the PMUT device is measured with an impedance analyzer (6500 B, Wayne Kerr Electronics) and is shown in Fig. 3.3d. Further characterization of the PZT has involved P–E hysteresis loop measurements (Fig. 3.3b). This is carried out after top electrode deposition. For this measurement, a Sawyer–Tower circuit is assembled where the PZT sample and a capacitor (C_0) of a known value are connected in series. The value of the sample capacitor (about 100 times the PZT capacitance) is chosen such that almost 99% of the applied voltage dropped across the PZT capacitor. From the applied voltage, the electric field is determined by considering the PZT thickness. Polarization charge density across the PZT capacitor is determined by dividing the charge across the capacitor of known value, C_0V_0, (same charge as the PZT capacitor in series) by the area of the PZT capacitor. A remnant polarization and coercive field of 12 µc/cm2 and 40 kV/cm, respectively. These in-house measurements compare well with the measurements done at aixACCT systems (from the last chapter 2). Here, note that the PZT thin film can stand up to 20 V without breakdown, which defines the limit on the applied driving voltages. However, during the P–E loop measurements, a voltage of up to 15 V is used to be on the safe side.

Next, further device fabrication steps are carried out the fabrication is completed. Fig. 3.3c shows a high-resolution optical microscope image of the fabricated PMUT. The array membranes with 6 µm of polyimide and 1 µm of PZT show almost straight sidewalls, demonstrating good fabrication quality. During DRIE, straight sidewalls ensure reproducibility with consistent etching rates and depth control, reducing defects. Note that the process is done from the bottom of the silicon wafer where the photoresist mask is opened for silicon etching and the process is designed to have the same lateral dimensions at the membrane. Additionally, sloped sidewalls can worsen the fill factor of the array, as such etching takes more space on the backside pattern.

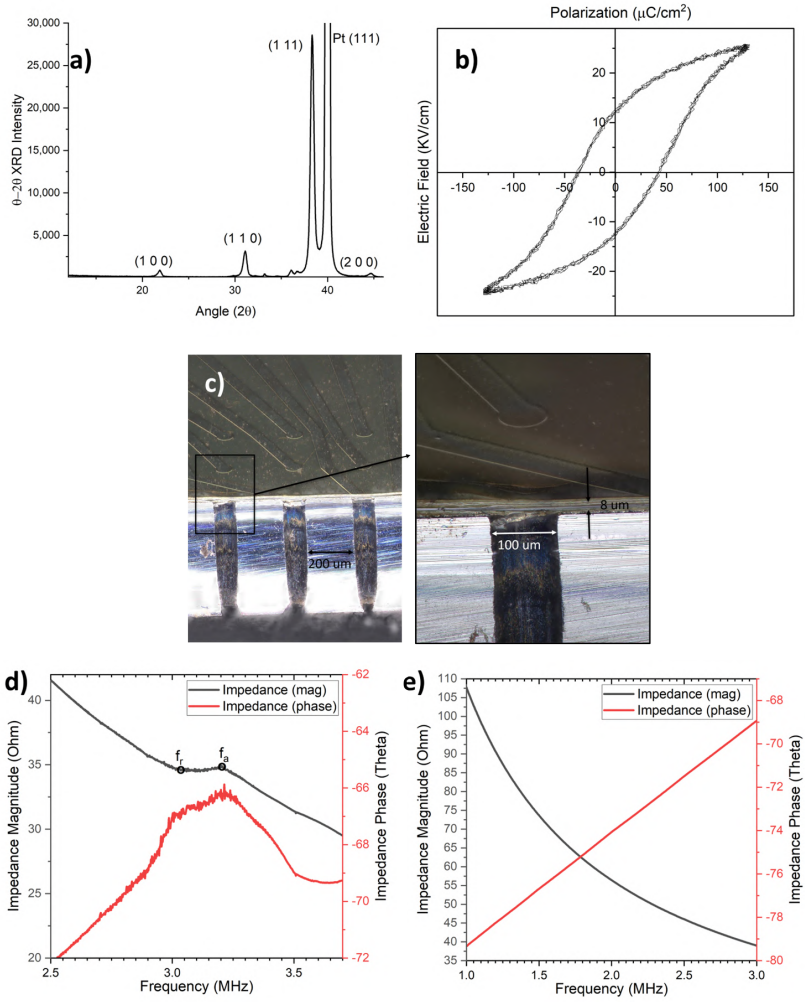

Figure 3.3: Material and electrical characterization of rigid PMUT device: (a) XRD of the PZT. (b) P-E hysteresis loop of the PZT. (c) A high-resolution optical microscope image of the high-frequency PMUT array membranes with 6 µm polyimide and 1 µm PZT, along with electrodes and oxide is about 8 µm in thickness. Zoomed-in view to the right. (d) The impedance of the single PMUT showing resonance (f_r) and antiresonance frequencies (f_a). (e) The impedance of the single PMUT underwater.

3.4.2 Laser Doppler Vibrometer (LDV) Measurements

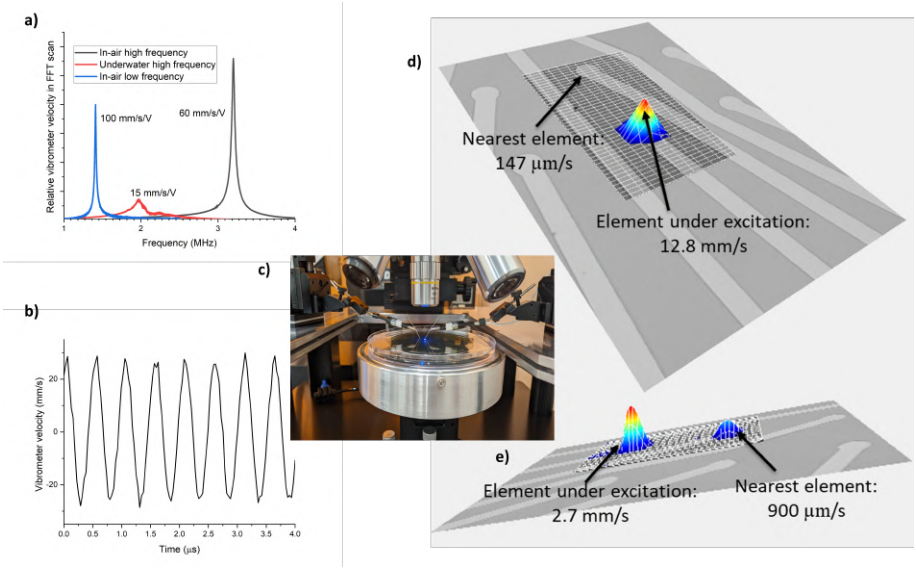

Figure 3.4: LDV measurements of single PMUT: (a) Frequency response in-air. (b) Underwater time domain response at 2 MHz with 2 V sinewave actuation along with (c) setup. Crosstalk (d) in air and (e) underwater.

The fabricated device is characterized in air and de-ionized water using LDV. The in-air resonance frequency is recorded using periodic chirp excitation as 3.2 MHz (Fig. 3.4a) with a transmission sensitivity of 60 mm/s/V. To experimentally demonstrate the resonance frequency tunability with polyimide thickness, another array is fabricated with 3 µm thick polyimide, showing a resonance frequency of 1.4 MHz in the air with a higher sensitivity of 100 mm/s/V (Fig. 3.4a). The measurements of eight PMUTs selected from this array show a small center frequency mismatch of 20 kHz (1.5%), demonstrating good fabrication uniformity. Moreover, LDV studies can also be performed in liquid mediums, as demonstrated by several other studies on PMUTs [115,116]. Underwater, the resonance frequency and sensitivity dropped to 2 MHz due to medium damping (Fig. 3.4a). The underwater sensitivity of the PMUT element is around 15 mm/s/V at 2 MHz, measured with sinewave excitation in a time-domain experiment (Fig. 3.4b). For crosstalk measurement, RMS velocities are recorded for the element under periodic chirp excitation and the adjacent unexcited element. A low in-air crosstalk (1%) is recorded (Fig. 3.4d). 6% in-air crosstalk is the lowest measured figure to date [115]. Meanwhile, underwater, coupled vibrations are observed in the nearby element (Fig. 3.4e).

3.4.3 Underwater Acoustic Characterization

The next measurements involve pulse characterization of the PMUT device underwater with a hydrophone (1 mm needle, Precision Acoustics). For this measurement, the PMUT array is glued to the PCB with epoxy (Fig. 3.5a) and then wire bonded to the PCB. Bond pads along with the bond wires are sealed with epoxy (Note that till this point, the device has been waterproof except for pads and this step makes waterproofing complete). Fig. 3.5b shows the setup for the hydrophone measurements. The hydrophone is aligned with the PMUT to obtain the maximum signal. The actuation amplitude is set as 10 V.

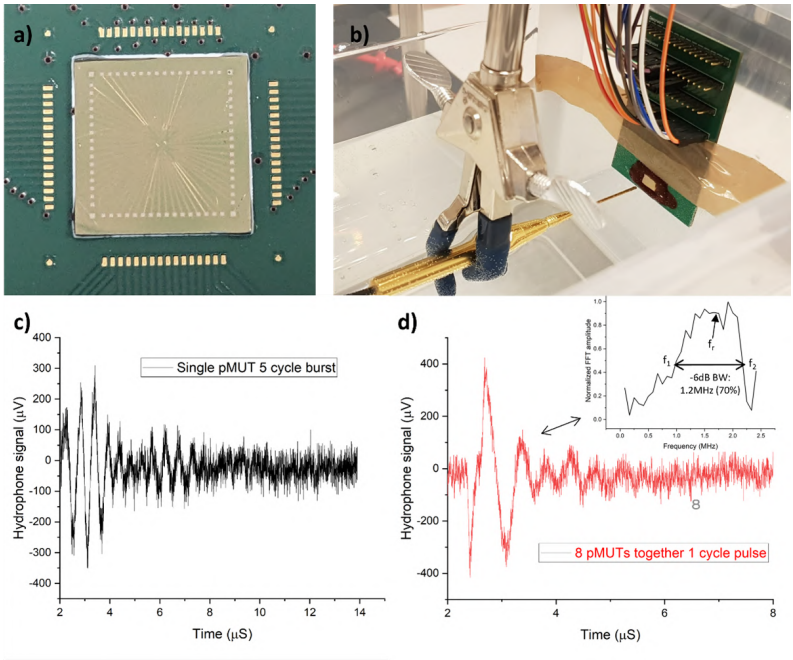

Figure 3.5: Underwater transmit characterization of rigid PMUT device with hydrophone: (a) PMUT array glued to the PCB before wire-bonding. (b) Underwater hydrophone setup with a PMUT array wire-bonded to a PCB followed by epoxy sealing (along the chip periphery in brown). (c) The response of single PMUT to 5-cycle square wave burst signal captured by hydrophone at 5 mm. (d) Response of eight PMUT elements together with 1 cycle pulse captured by hydrophone at 1 cm.

The first measurement concerns a single PMUT element. Fig. 3.5c shows the response of a single PMUT to five cycles of a square wave burst signal at 2

MHz. Hydrophone at 5 mm measures a transmission response of 400 Pa, i.e., 40 Pa/V. This suggests that focusing all 64 elements of the array together can produce approximately 20 kPa at the current impedance setting. However, with impedance matching, it is possible to generate even higher pressures. Still, the response can be considered to be on the lower side [35]. The lower response can be explained as follows: (1) It is the pressure generated by a single PMUT element and hence a very small vibrating aperture, resulting in a lower response. (2) Less ringing means a wide bandwidth and that its vibration is damped significantly. Moreover, widening the bandwidth using a polyimide passive layer comes at the cost of a lower bending moment. Therefore, a lower vibration amplitude and, consequently, a lower output pressure are obtained. (3) A smaller voltage appears across the PMUT due to parasitics and impedance mismatch, further reducing the pressure.

The second measurement is carried out by exciting eight PMUT elements together with one cycle pulse with the hydrophone at 1 cm (Fig. 3.5d). The distance is increased so that the combined effect of eight PMUTs is translated into the measurement. This measurement shows a pressure of 500 Pa. Due to no focusing, output power limitations from the signal generator, and insufficient excitation energy from one cycle pulse, only 500 Pa is obtained. The FFT of the time-domain response (inset of Fig. 3.5d) suggests that the transducer has a center frequency of around 1.7 MHz and a -6 dB bandwidth (BW) of 1.2 MHz, which is 70% of the center frequency, comparable to the most recent bulk-piezoelectric-based ultrasound imagers [2, 117].

Lastly, to measure the receive sensitivity of the PMUT transducer, a single-element wide-band transducer (Precision Acoustics, UK) is used to transmit a burst signal at 2 MHz. The transmitted signal is measured by the calibrated hydro-phone and the PMUT transducer. The measured hydrophone signal (Fig. 3.6a) amounted to a 73 kPa pressure. Fig. 3.6b shows the received signal of eight PMUTs connected in parallel in response to 10-cycle sinusoidal burst signal. Since the same pressure levels are applied to the PMUTs (by maintaining the same distance and applied burst signal level), the receive sensitivity is calculated by dividing the voltage signal in response to the 10-cycle burst by 73 kPa pressure, and a receive sensitivity of about 15 mV/MPa is obtained for the PMUTs. This receive sensitivity is found to be on the lower side because of the high parasitic capacitance of the PMUT interconnects. Note that the pulse response of the single-element transducer utilized in this experiment is not short and has some ringing. However, a very similar response is captured by the PMUT channel and hydrophone, again a confirmation of the wide bandwidth demonstrated by this technology, which makes the PMUT attractive for ultrasound imaging applications. For imaging applications using ultrasound transducer arrays, resonance frequencies of several MHz and a fractional bandwidth from 40 to

80% are used [118]. Sadeghpour et al. tabulated the specifications of state-of-the-art PMUT arrays designed for imaging, which show pressure levels of about a few kPa to perform imaging in several mm ranges [35]. To use the PMUT array for imaging applications, focused ultrasound, and impedance matching are required to improve the transmit response.

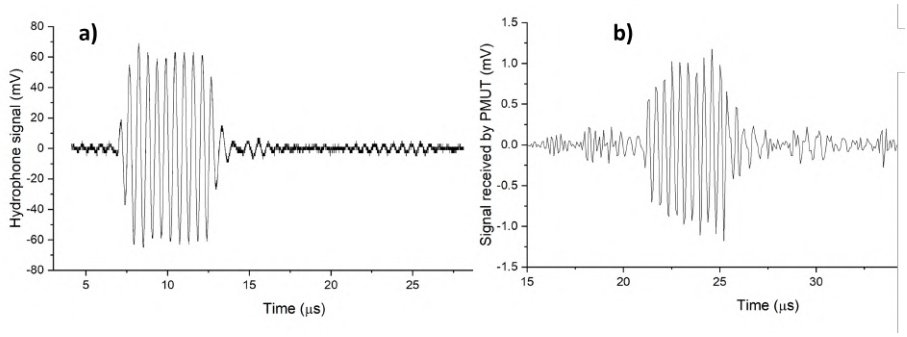

Figure 3.6: Underwater receive characterization of rigid PMUT: Signal measured by (a) hydrophone and (b) PMUT in response to 10-cycle pulses.

3.5 Conclusion

The low-cost SOI-free technology of a PZT-based PMUT is described in this chapter for a fully addressed array with its design fabrication and detailed characterizations. The polyimide membrane passive layer can enable resonance frequencies required for low-frequency ultrasound imaging. It is shown that the resonance frequency can be easily tuned by controlling the thickness of the polyimide. The PMUT membranes are realized using backside DRIE with an oxide etch stop. The fabricated PMUT with 6 µm thick polyimide membranes showed a 3.2 MHz in-air frequency with a 3 nm/V sensitivity, the lowest interelement crosstalk of 1% between the PMUT elements. Additionally, a pressure response of 40 Pa/V at 5 mm is measured underwater using a hydrophone while exciting a single PMUT element. The single-pulse response captured using the hydrophone suggests a 70% fractional bandwidth of the center frequency and is attractive for ultrasound imaging applications. Moreover, optimization is being attempted for this technology to be applied in imaging applications in shallow-depth regions.

Chapter 4

Flexible PMUT Development

This chapter is adapted from a previously published article: Joshi et al. Bendable Polymer-Based High-Frequency pMUTs on Transparent SU8 and Polyimide Substrates, Transducers 2023 proceedings, pp. 849-852 [119].

4.1 Background

Rigid PMUTs and CMUTs are commonly fabricated on SOI wafers [36, 67]. However, the opaque silicon can hinder their use in tactile displays [120], and their inability to achieve solid interfacial contact with non-planar surfaces leads to unreliable results. In contrast, a bendable device array on a curved surface not only can be conformally attached but also functions as a mechanical lens to focus ultrasound and saves power consumed in electrical focusing. Moreover, flexible ultrasound transducers are user-friendly for continuous monitoring.

As explained in chapter 1, flexible PMUTs show a trade-off between performance and bendability, e.g., silicon-based approaches provide high acoustic pressures but island-spring-based meta-rigid designs or silicon-PDMS-based designs have a limited interconnect area, and fill factor [54]. Thinned silicon or substrates with continuous topography would not have this issue however, thin silicon is fragile [49]. Considering the convenience of interconnect design, PMUTs on flexible substrates are considered. To deal with the low sensitivity of devices on flexible substrates, multiple transducer elements can be excited together.

PMUTs on polymer substrates such as SU8 and polyimide can conform to the

skin, providing advantages of wearable technology. Polyimide is a partially transparent material that has been widely used for developing flexible ultrasound transducers, as well as other electronic devices such as flexible solar cells and neural probes [50, 121, 122]. This is due to its high bendability, excellent mechanical strength, and thermal stability, as well as electrical insulating properties. Additionally, it is easy to deposit using spin coating or as an adhesive tape and pattern with photo patternable alternatives (PI-4100 series, HD Microsystems), or laser-based techniques [123]. On the other hand, SU8 can provide partial bendability with the added advantages of high transparency and the ability to realize high aspect-ratio microstructures using photolithography [124, 125]. Using other transparent substrates such as glass or PET for high-resolution bulk micromachining can be challenging. SU8 has been a common structural material in polymer-based CMUTs but has not been investigated as a substrate [72, 126]. Moreover, the lack of studies on PMUTs with SU8 structures and substrates can be attributed to the challenges involved in the fabrication process. Releasing the device and managing the SU8 temperature budget during high-temperature processes in the transducer fabrication pose significant complexities. For instance, a PZT sol-gel process typically involves a rapid thermal annealing step at 700°C. However, SU8 can withstand only up to 200°C, which is the maximum recommended hard bake temperature [127].

This chapter presents the development of flexible PMUT technology- mainly the fabrication process and preliminary results. The "polymer substrate last approach" introduced here involves processing the polymer substrate after high-temperature fabrication steps, such as oxide growth and rapid thermal annealing of sol-gel PZT. By doing so, we address the challenges of incorporating high-performance ceramics in flexible devices. PZT thin films are commonly used in piezo-MEMS due to their excellent piezoelectric properties [107].

4.2 Design-Fabrication Scheme

The key components of a PMUT comprise a membrane and a cavity sidewall (for PMUTs, the cavity sidewall also acts as a substrate and hence, now on, referred to as substrate sidewall). The membrane usually contains a patterned layer stack of passive layers, electrodes, and piezoelectric thin film. Fig. 4.1a shows a 3D schematic of the PMUT design. The active PZT is sandwiched by Pt electrodes, on top of the polyimide passive layer. The dimensions of the membrane and substrate sidewalls are given in Table 4.1. Fig. 4.1b shows the cross-section illustration of a single bendable PMUT element. It is important to note the presence of a polyimide interlayer between the bottom electrode-PZT and the top electrode; this enables the PMUT device to function without any

electrical shorts and decreases the PMUT capacitance. Alternatively, silicon oxide can also be used for similar purposes [54].

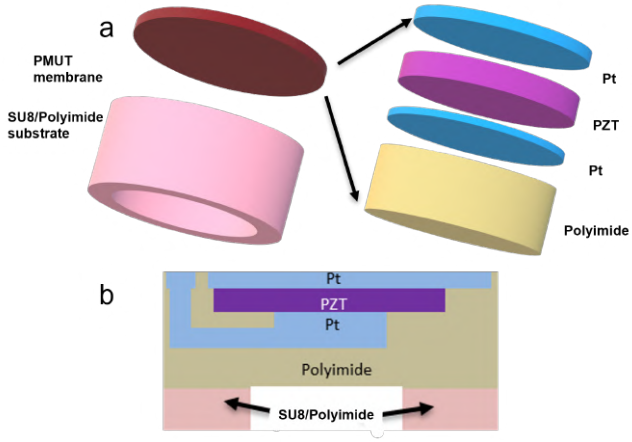

Figure 4.1: a) 3D Schematic of a bendable PMUT element and layer stacks in the membrane (right). b) PMUT cross section. Schematics are not to scale.

The fabrication schematic is in Fig. 4.2. The top-down fabrication scheme is inspired by the process described in [43]. However, considering the complexity of 2D array design, optical microscopic images of each fabrication step are provided as well in Fig. 4.3 and are used for further illustration.

On the oxidized wafer, the bottom Pt layer is patterned acting as the seed layer for PZT. Pt also acts as the electrode pad layer- the array corners are electrode pads common to all elements whereas the other pads provide electrical access for each individual PMUT element in the array (Fig. 4.3a). This is followed by PZT patterning (Fig. 4.3b). Then, a 2.5 µm polyimide interlayer (6000 RPM is used for spin coating [128]), which acts as a dielectric, reduces parasitic capacitance and roughness across the wafer, is deposited and opened (Fig. 4.3c) to realize interconnects from the PMUT element to individual electrode pad (Fig. 4.3d). For top conformal electrode deposition, it is beneficial to limit the topography variation across the chip. Since polyimide interlayer patterned at vias and PMUTs is responsible for this topography variation, its thickness should be as low as possible. Whereas to ensure that the patterned bottom Pt, PZT layer is conformally covered, the thickness of polyimide is chosen to be 2.5 times the PZT, and bottom electrode thickness combined to be safer.

After interconnects, the polyimide passive layer (7 µm in thickness achieved

using 2000 RPM during spin coating) for the membrane is deposited, soft-baked, and cured. The membrane thickness ensures the neutral axis is away from the PZT, which is required to improve sensitivities [84]. After the aforementioned steps, the substrate layer is deposited and patterned to realize a substrate sidewall structure with a cavity diameter of 100 µm (Fig. 4.3e).

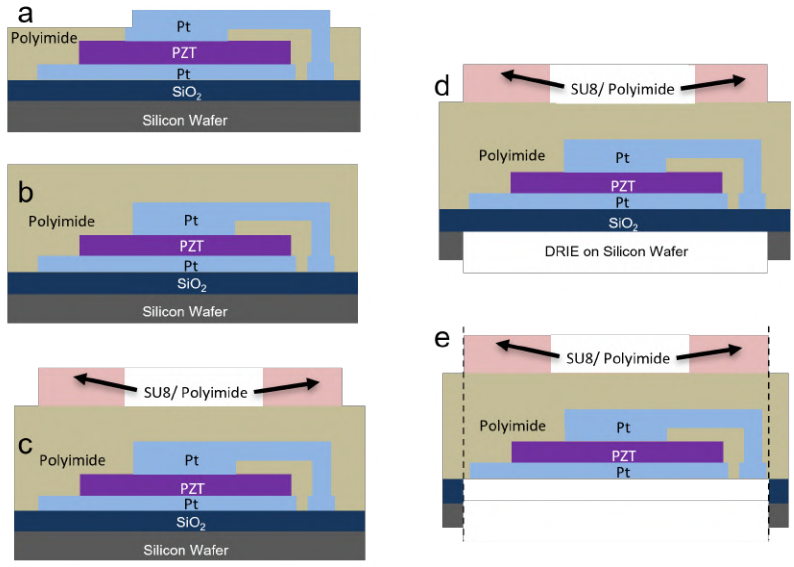

Figure 4.2: Bendable PMUT fabrication process schematic: a) Prepared wafer with the active layers. b) polyimide membrane passive layer deposition. c) SU8/polyimide substrate sidewall patterning. d) Backside DRIE on silicon e) Oxide removal and cutting the flexible chip from the wafer with a scalpel.

For PMUT on SU8, about 300 µm thick SU8 is deposited by casting (to be patterned later as a substrate sidewall). For the 3-inch wafer used for this process, 2.5 mL SU-8 2007 is cast on the wafer on leveled hotplate. It is allowed to spread at room temperature (hourglass over it against solvent evaporation for 15 min). Then, it is baked for 4 hours at 80°C. Then, it is exposed with a dose of $12 J/cm^2$ through PMMA filter (suitable for thicker layers than 300 µm filtering out light below 400 nm). Alternatively, about 850 mJ/cm2 with the SU-8 filter also works [129]. This is followed by post-exposure baking at 80°C for 1 hour. Finally, it is developed upside down in PGMEA, for about 20 minutes. It can be hard-baked optionally at 150°C for 1 hour. For PMUT on polyimide, 28 µm polyimide was deposited by repeated spin coating (4 times) and a single hard baking step was performed. It is patterned with a chromium

layer as a hard mask. The thickness is chosen based on a report that mentions a polyimide substrate thickness of around 25 µm is a favorable balance between high bendability and easier handling [50].

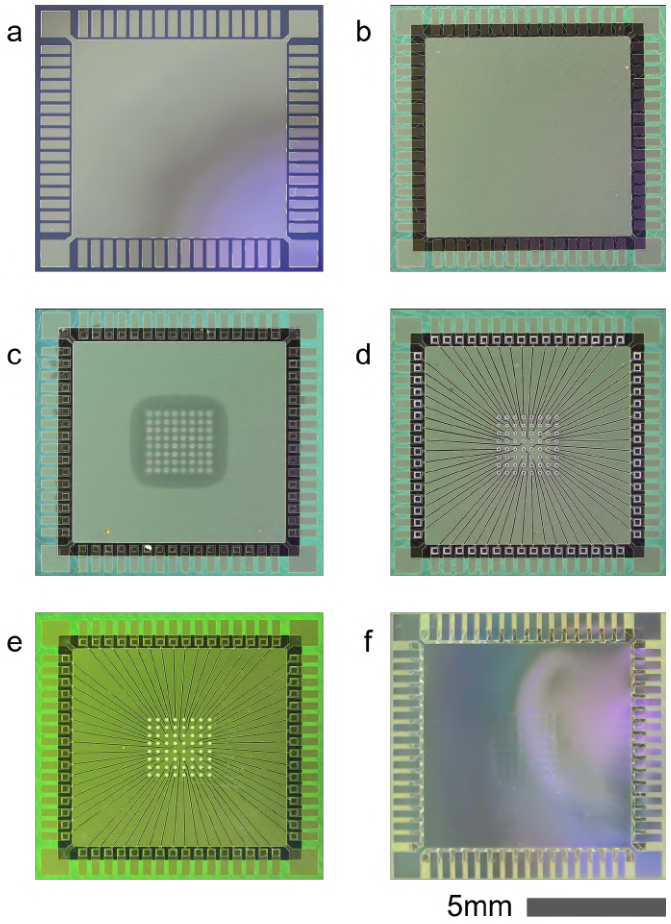

Figure 4.3: Optical microscope images taken during flexible PMUT fabrication: a) patterning of the bottom Pt layer on thermal oxide. b) Sol-gel deposited PZT is patterned in the pad area. c) Polyimide interlayer patterning. d) Top Pt layer patterning of electrodes and interconnects for individual PMUT elements. e) Polyimide membrane layer deposition followed by polyimide substrate sidewall patterning. f) After DRIE and oxide removal, the exposed bottom Pt layer from the backside.

Finally, DRIE is performed on the stack to release the flexible array from the silicon carrier followed by oxide removal to access electrode pads (Fig. 4.3f). The array is then cut from the wafer with a scalpel to complete the fabrication.

Material	Function	Thickness (μm)	Deposition method
SU8	Substrate sidewall	300	Casting
Polyimide	Substrate sidewall	40	Spin coating
Polyimide	Membrane passive layer	7	Spin coating
Polyimide	Dielectric layer	2.5	Spin coating
PZT	Piezo layer	1	Sol-gel
Pt	Top & bottom electrode	0.2	RF sputtering
Silicon oxide	Etch stop for DRIE	0.5	Thermal wet oxidation
Silicon	Temporary carrier	380	--

Table 4.1: Details of the materials used for the flexible PMUT technology

4.3 Preliminary Characterization Results

Images of the released PMUTs on SU8 and polyimide substrate are shown in Fig. 4.4a,b, respectively. A difference between the stiffness of the substrate arising from their thicknesses is clearly noticeable. Fig. 4.4c shows the patterned substrate on the membrane stack. A close-up view of membranes on SU8 is shown in Fig. 4.4d. Fig. 4.4e shows the device on SU8 bent and mounted on a curved fixture with a 25 mm bending radius. Such a bending radius is suitable for shoulder, abdomen, or knee areas. PMUT on polyimide is much more flexible and can be bent even on a finger with a 5 mm bending radius (Fig. 4.4f). Although SU8 and polyimide have a similar Young's modulus, the drastic difference in the bendability is due to two reasons: 1) Difference in the device thickness and hence the stiffness. 2) Difference in the fracture strength of both substrate materials- polyimide with 350 MPa and SU8 with 10 times lower value of 34 MPa. Hence, SU8 is brittle and has a higher chance of breaking than polyimide for a similar bending radius.

LDV measurements on SU8 PMUTs (Fig. 4.54a) show high resonance frequencies of 15 MHz and 12 MHz in-air and underwater, respectively. For PMUT on polyimide, resonance is at 5 MHz in-air and 4 MHz underwater, respectively (Fig. 4.5b). The membrane in both devices is made of polyimide with the

same thickness. Hence, their first-mode eigenfrequencies should theoretically be similar. The key difference lies in the substrate sidewall material—SU8 versus polyimide—which affects residual stresses during fabrication. Polyimide generates relatively low residual stress, whereas SU8 induces significantly higher stress. This difference suggests that the substrate sidewall material, and the residual stresses it introduces, play a crucial role in determining the resonance behavior of the devices. Understanding these influences requires further investigation to optimize the design and performance of flexible PMUTs.

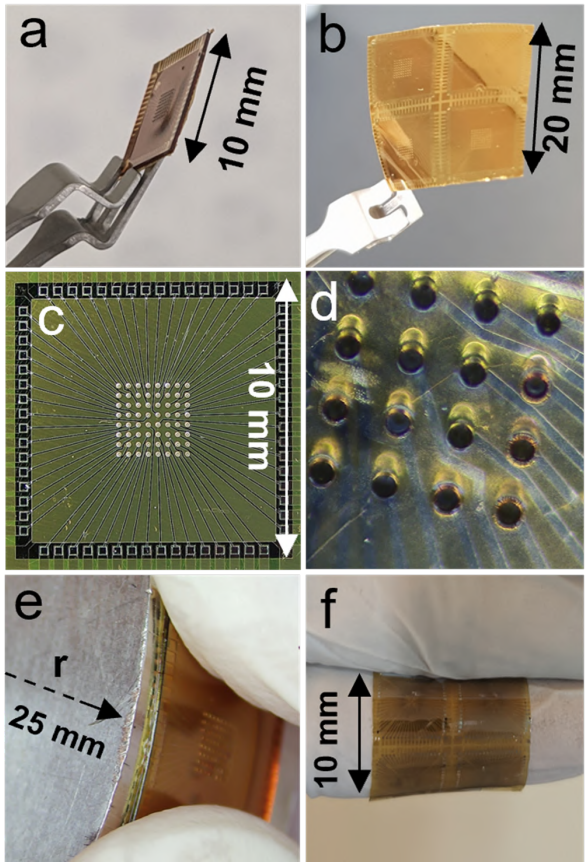

Figure 4.4: Released PMUT on a) SU8 and b) polyimide substrate. c) PMUT membranes and interconnects. d) Magnified view at 30° to normal showing cavities patterned in SU8. e) SU8 PMUT mounted on a curved fixture of 25 mm radius. f) Polyimide PMUT wrapped around a finger.

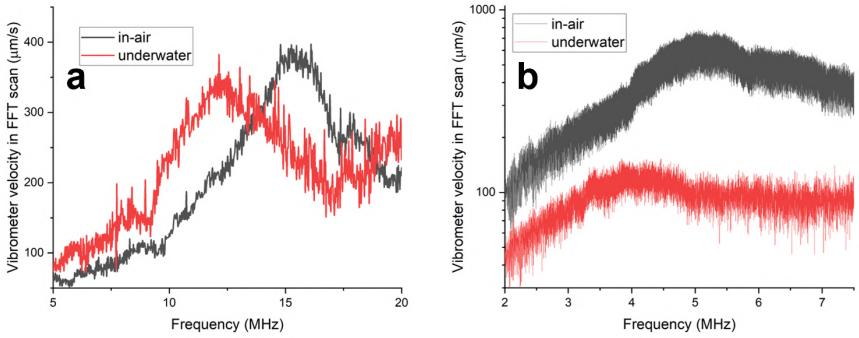

Figure 4.5: LDV measurements of a flexible PMUT element: Frequency response of the a) SU8 PMUT and b) polyimide PMUT.

4.4 Conclusion

This chapter presents the development of bendable PMUTs based on polymer substrates using a substrate last approach for incorporating PZT ceramic thin film. The top-down fabrication process uses a silicon wafer as a temporary carrier from which a flexible PMUT array is released by DRIE. The flexible PMUT membrane consists of 1 µm PZT and 6 µm polyimide layers. A substrate sidewall with a cavity of 100 µm in diameter is defined by reactive ion etching (RIE) for polyimide based-PMUT and by just photolithography for SU8 one. The basic functionality of the PMUTs is demonstrated through bending tests and LDV characterization in-air and underwater. The performance comparison of the PMUTs on SU8 and polyimide substrates suggests that PMUT on polyimide shows better bendability and the one on SU8 shows higher transmit sensitivity and resonance frequency. The underwater high resonance frequencies make the technology particularly interesting for imaging applications. However, the influence of substrate sidewalls and residual stresses during fabrication of the device on SU8 substrate on performance needs investigation and will be addressed in future work. Nevertheless, a PMUT on the SU8 substrate is fabricated for the first time and the novel fabrication flow of PZT-based flexible PMUTs on polyimide is established.

Chapter 5

Row-Column (RC) Addressed PMUT Development

This chapter is adapted from a previously published article: Joshi et al. A 50x20 Row-Column Addressed PMUT Array on Silicon Substrate for Imaging, IUS proceedings 2023 [130].

5.1 Background

For applications such as medical imaging, ultrasound transducers are operated at high frequencies which are in the megahertz (MHz) range. A PMUT element designed at such resonance frequency typically has a small aperture. The acoustic pressure generated by the vibrating diaphragm of a small aperture is generally not sufficient for medical imaging applications. Hence, the excitation of multiple elements from an ultrasound transducer array is preferred to generate higher acoustic pressures. Moreover, array schemes enable signal transmission and reception at a high SNR for real-time image generation without mechanical scanning. These arrays employ beamforming and precise electronic control over ultrasound beam focus, steering, and signal timing. In this context, 2D ultrasound arrays allow real-time 3D volumetric imaging, benefiting applications like cardiac imaging, obstetrics, and musculoskeletal imaging.

For 3D imaging, the fully addressable designs are more common as it has the advantage of providing high SNR for 3D imaging without any complicated

switching circuitry [131]. However, it is quite challenging to further scale the array size to have more elements as 1) it increases the number of cables. 2) it complicates interconnect design or needs innovative wiring or packaging. For instance, although the 11 × 11 fully addressable array from section **??** has an active aperture of about 5 mm × 5 mm, the chip size including interconnects is about 2 cm × 2 cm.

In comparison with fully addressable 2D arrays with a dedicated pad for accessing individual elements, RC-addressed arrays can be designed with a compact form factor. RC-addressed arrays use one pad per row and one pad per column to access their individual elements and hence achieve a high density of elements in a small footprint due to fewer interconnect lines. This compactness facilitates easier integration into portable ultrasound devices and better access to anatomically challenging regions. However, implementing an RC addressing scheme for ultrasound transducers involves additional complexity in terms of electronics and control. For example, during a pulse-echo experiment, transmit operations are performed with transducer elements in a row and receive with those in a column, or vice versa, adding complexity to switching circuitry. Moreover, the main shortcoming is the complexity of the fabrication process leading to lower yield.

Although each approach has its nuances, both are worth the research. In this chapter, the focus is RC-addressed arrays. Starting with the single-element simulations, RC-addressed array design, and fabrication on conventional silicon wafers with polyimide membranes are discussed first. It is followed by measurements with LDV and hydrophone to demonstrate the working of the PMUT as a transmitter as well as a receiver. In the end, similar fabrication on SOI wafers and its nuances are touched upon briefly.

5.2 COMSOL Simulation

The acoustic pressure simulations for the single PMUT element (not the array) are carried out in a water medium. The single element of the RC-addressed PMUT is the same as that of the 8 × 8 fully addressed PMUT from chapter 3. A COMSOL 2D axisymmetric model is used to carry out these simulations (geometry in Fig. 5.1a). PMUT is an axisymmetric device, hence axisymmetric simulations can be used to drastically reduce the simulation time.

For the simulations, the PZT is actuated with a 1 V electric potential difference between the top and bottom boundaries with the electrostatics module of COMSOL. The piezo material chosen in the COMSOL models, PZT-5H, comes with defined properties including piezoelectric and elastic coefficient matrices.

However, the experimentally prepared PZT thin film properties are different from the properties defined for PZT-5H. Characterized values from chapter 2 are used as an input for the piezoelectric material introduced in the solid mechanics model ($d_{33} = 60pm/V, d_{31} = 25pm/V, \epsilon = 800$).

The mesh and the perfectly matching layer (PML) are designed according to the COMSOL documentation [132]. The mesh size in the water domain ensures that the smallest wavelength is resolved by at least 6 elements, whereas the boundary layer thickness is chosen to be 20 times lower. The resolution in the narrow region (for instance, the piezo layer) is set to 2. For convergence testing, the maximum mesh size in the solid mechanics domain is parameterized. However, because of the narrow region resolution condition, all meshes have the same result, as the meshing has not changed significantly.

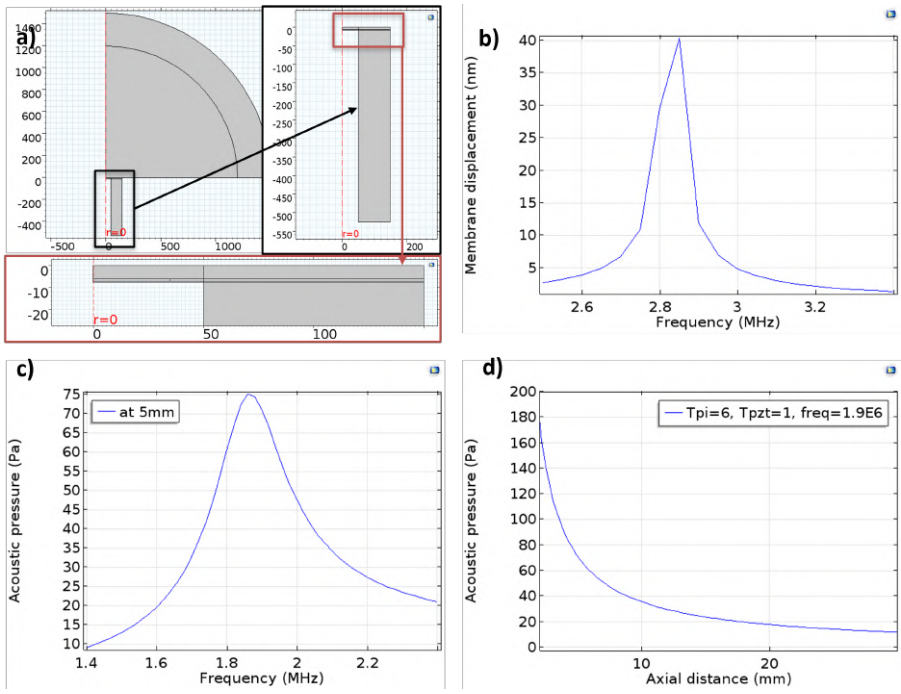

Figure 5.1: COMSOL simulation of a single PMUT element: (a) Simulation geometry with zoomed-in views. The PMUT axis is indicated by r=0, where r is the radial coordinate. (b) Membrane displacement in-air, and (c) underwater on-axis sound pressure response at 5 mm. (d) At 1.9 MHz, pressure decay with axial distance.

For the PMUT single element, a frequency sweep is performed and membrane displacement in-air and pressure response at 5 mm in water with frequency are plotted in Fig 5.1b,c. These indicate a resonance frequency of around 2.9 MHz in air and 1.9 MHz in water. Moreover, at the underwater resonance frequency, on-axis transmitted pressures are shown in Fig. 5.1d, showing an inverse relationship with distance.

Although simulations of the PMUT array are not presented here, a preliminary perspective on the system's behavior is provided briefly here. In an array channel with parallelly connected (assumed identical) PMUT elements, the electrical and motional properties change in specific ways. The total capacitance proportionally increases with the number of elements, while the overall impedance and motional resistance (R_m) decrease, allowing more current to flow at the same voltage. In other words, reduced impedance means the driving circuit needs to handle a higher current. If the system is capable of handling higher currents, each PMUT element can generate a surface pressure comparable to the scenario where it is excited independently. The acoustic pressure at a specific on-axis distance increases due to the contribution of multiple elements operating in parallel. Additionally, the array maintains a receive sensitivity similar to that of a single-element configuration.

5.3 Design-Fabrication Scheme

For realizing the device on a silicon substrate with polyimide membrane, the steps from chapter 3 are followed with slight modification, and the scheme is shown in Fig. 5.2a for reference. Fig. 5.2b shows a part of the fabricated array with the bottom electrode rows and top electrode columns. The 20 rows each at two ends of the array form electrode pads for the top electrodes (duplicated in the design and interconnected) whereas the central 50 rows are the bottom electrode rows of the row-column PMUT. The figure also shows a unique interconnect scheme where via through polyimide and PZT connect the top electrode line (PMUT column) to the top electrode pads. This arrangement allows for accessing rows and columns with pads in a single line, making the device easy to integrate with electronics and package. The array is 50 × 20 elements with a 300 µm pitch. Hence, the total aperture of the PMUTs is 15 mm × 6 mm and the chip size including interconnects and pads is about 27 mm × 8 mm. The membrane diameter (100 µm) and the thickness (6-7 µm) are the same as that used for the fully addressed scheme in chapter 3 as the underwater frequency is again desired around 1.5-2.5 MHz.

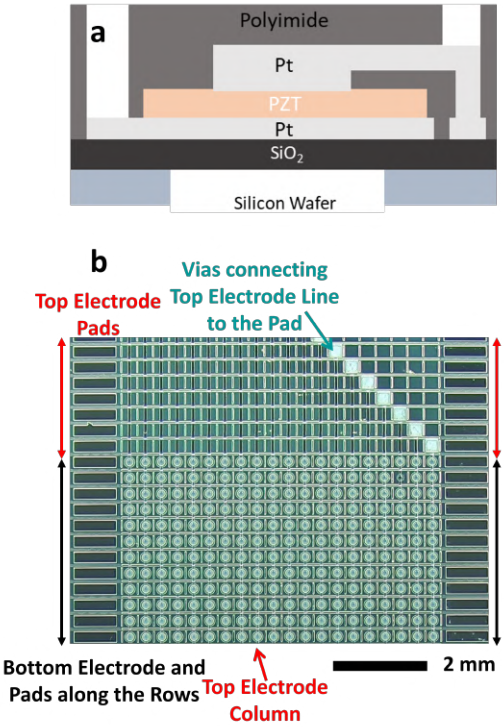

Figure 5.2: Row-column (RC) addressed PMUT design: (a) Single PMUT schematic and (b) a part of the fabricated PMUT array.

The fabrication steps for the PMUT array (follow Fig. 5.3) involve wet oxidation of a silicon wafer, followed by the active layer patterning, i.e. bottom Platinum (Pt), PZT, and top Pt layers. Pt acts as the seed layer for PZT deposition and the electrode pad layer as well. This prepares the substrate for further steps. After this, sol-gel PZT deposition is followed which involves spin coating, pyrolysis, and rapid thermal annealing processing. More details regarding PZT deposition and patterning can be found in chapter 2 and 3. Note that, the PZT cracks in the area between the adjacent Pt lines, where it is deposited on oxide. Possible shorts arising due to this are avoided by the polyimide interlayer which also reduces parasitic capacitance and roughness across the wafer. It is patterned for connecting the top electrode line to PZT below and to the top electrode pads through vias. After top Pt lines interconnect the PMUT elements, a 7 µm thick polyimide passive layer is deposited and opened to access pads. Finally, membranes are released by DRIE to complete the fabrication.

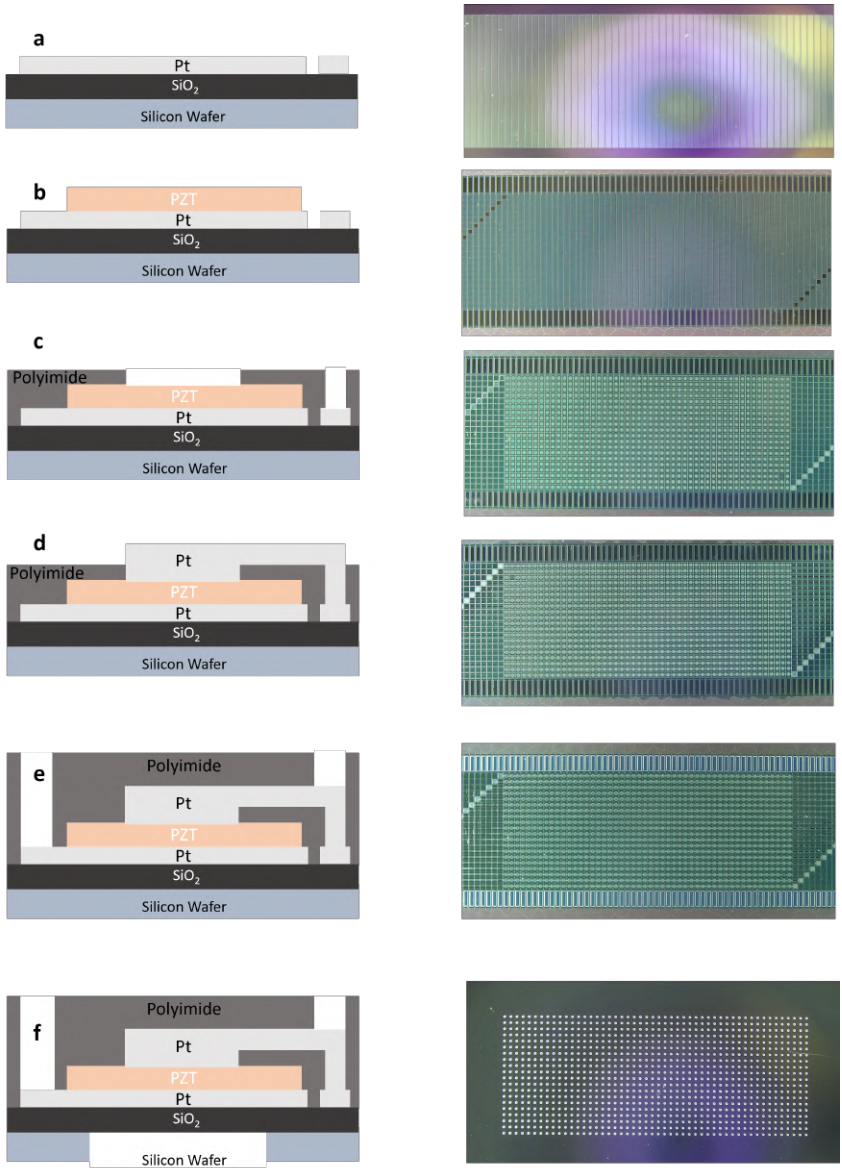

Figure 5.3: Fabrication steps for the row-column addressed PMUT device: (a) Patterning of the bottom Pt layer on thermal oxide. (b) Sol-gel deposited PZT is patterned for pads and vias. (c) Polyimide interlayer patterning for vias and electrodes. (d) Top Pt interconnect patterning (e) Polyimide membrane layer deposition followed by patterning for opening pads. (f) Backside DRIE process.

Next, the PMUT arrays are diced with a dicing saw and glued to the PCB with epoxy (Fig. 5.4a), and then wire bonded to the PCB (Fig. 5.4b). Bond pads along with the bond wires are sealed with epoxy.

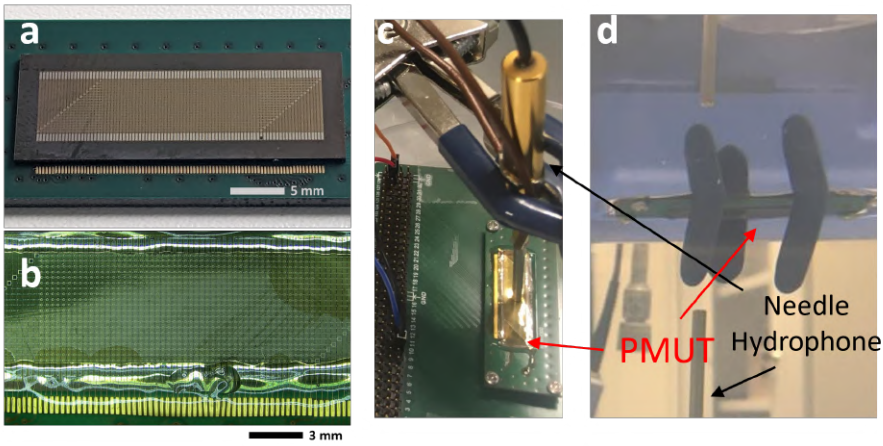

Figure 5.4: (a) Part of the array showing wire bonding and sealing the bond wires and pads with epoxy. (b) Diced PMUT array glued to the chip before wire bonding. Hydrophone setup at (c) 5 mm and (d) 2.5 cm.

5.4 Results

The fabricated device is first characterized using LDV. The in-air and underwater resonance frequency is recorded using periodic chirp excitation as 3.2 MHz and 1.85 MHz, respectively (Fig. 5.5a,b). The transmission sensitivity of the PMUTs is measured to be 600 mm/s/V (30 nm/V) and 80 mm/s/V in-air and underwater, respectively, with a 5 V sinewave excitation and a DC offset of 5 V at the respective resonance frequencies in a time-domain experiment (Fig. 5.5c,d). These results closely match with the simulations presented earlier in this chapter (Fig. 5.1b). Moreover, less than 10 % in-air crosstalk with neighboring unexcited elements is observed (Fig. 5.5e), comparing well with the literature [92].

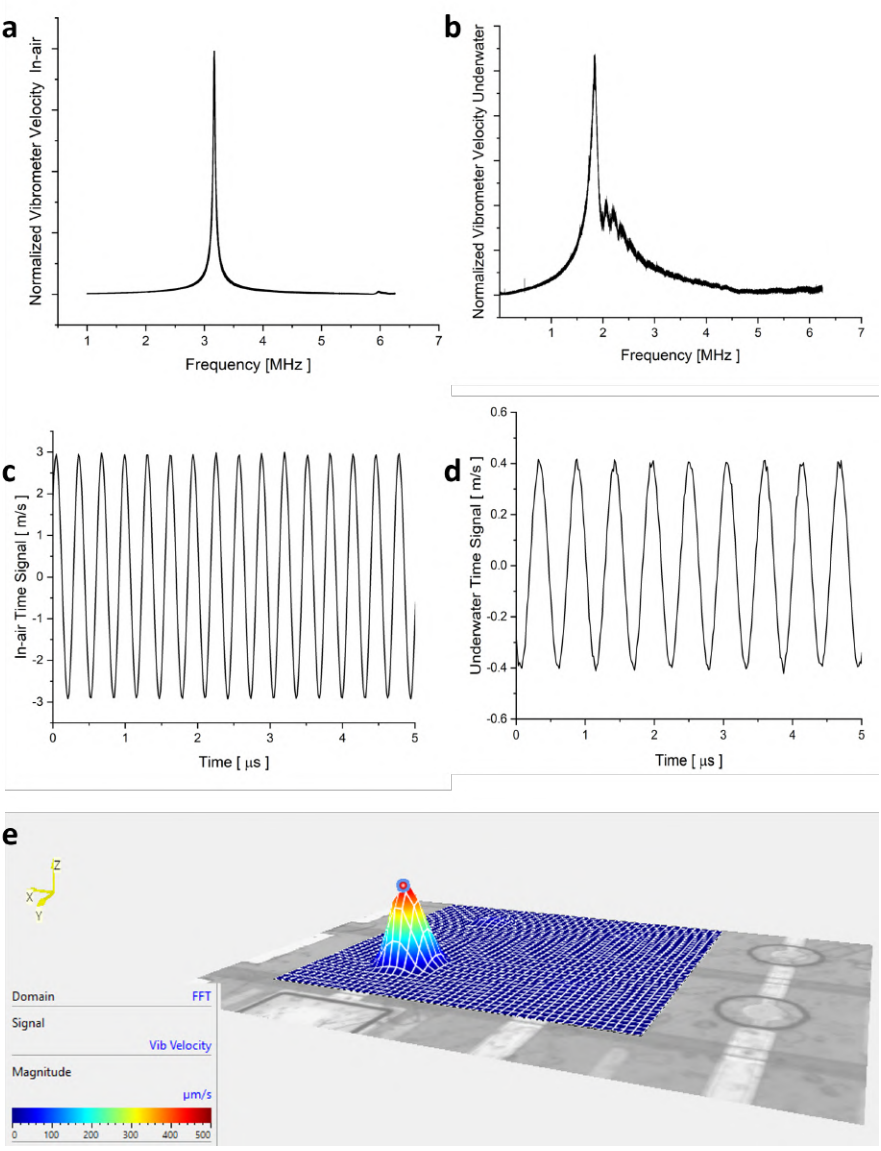

Figure 5.5: LDV characterization of single PMUT element: Frequency response (a) in-air and (b) underwater. Time domain response (c) in-air and (d) underwater at 5 VAC sinewave excitation at resonance frequency with 5 V DC offset. (e) In-air crosstalk analysis by LDV.

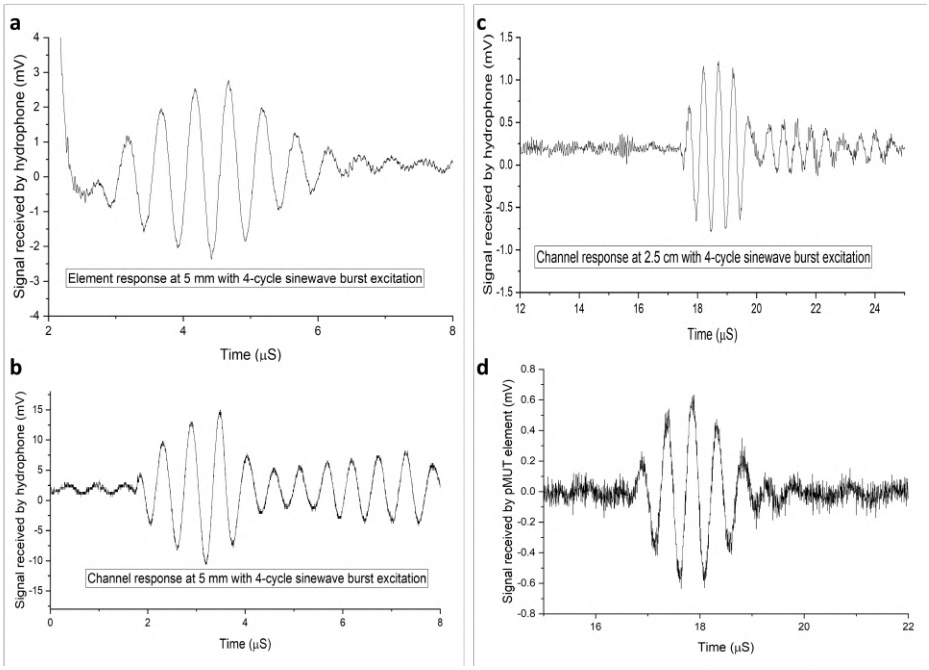

Figure 5.6: Underwater characterization of RC addressed PMUT: As a transmitter, hydrophone measurements with 4-cycle sinewave of (a) a single element at 5 mm,(b) a single channel at 5 mm, (c) a single channel at 2.5 cm. (d) As a receiver, 22.5 kPa pressure (burst) signal received by PMUT.

The next measurements involve pulse characterization of a single PMUT element underwater with a hydrophone (2 mm needle, Precision Acoustics, UK) with a sensitivity of about 3.5 V/MPa around 2 MHz. For this measurement, Fig. 5.4c,d shows the setup for the hydrophone measurements at 5 mm and at 2 cm distance. The actuation amplitude is set as 5 V AC along with 5 V DC bias. Four-cycle Sinewave burst pulses at 2 MHz are applied with the HMF2525 function generator (Rohde & Schwarz) in this experiment. Fig. 5.6a shows the response of a single PMUT element to four cycles of a sinewave burst signal at 2 MHz. It indicates a transmission response of 750 Pa at 5 mm, i.e., 150 Pa/V. Here, the measured pressure is almost double compared with what is presented in the simulation result (Fig. 5.1c). This contribution could be coming from the crosstalk with neighboring elements and needs further in-depth study. The second measurement is carried out by exciting the single PMUT channel with a four-cycle square wave pulse at 5 mm (Fig. 5.6b) which resulted in a higher

sensitivity of about 400 Pa/V. For this characterization, all rows of the array are connected to the ground and the signal is applied at a column. In another measurement at 2.5 cm in a water tank, the same channel indicates 80 Pa/V sensitivity (Fig. 5.6c). Although the bandwidth is not shown here, is very similar to that of fully addressed PMUT (about 60 %).

Lastly, to measure the receive sensitivity of the PMUT transducer, a single-element transducer (Precision Acoustics, UK) is used to transmit a four-cycle burst signal at 2 MHz. The transmitted signal is measured by the calibrated hydrophone and the PMUT transducer. The measured hydrophone peak pressure is about 22.5 kPa. Fig. 5.6d shows the received signal on an oscilloscope from the single element PMUT. Since the same pressure levels are applied to the PMUTs (by maintaining the same distance and applied burst signal level), the receive sensitivity is calculated by dividing the voltage signal, resulting in a receive sensitivity of about 30 mV/MPa for the PMUTs. Note that, no amplifier is used in the receive mode.

5.5 Device Fabrication on the SOI Wafer

Despite the potential of RC-addressed PMUT arrays, the exploration of RC PMUTs in the imaging domain remains limited. Hence, it is explored further here with the SOI platform for comparison (and on a flexible platform in the next chapter). The schematic of a single element of the PMUT array is shown in Fig. 5.7a. The device design and fabrication follow a similar scheme as explained previously in the chapter, except for a couple of modifications- 1) Instead of a conventional silicon wafer, an SOI wafer is used in this fabrication and a 6 µm thick silicon device layer acts as a passive layer. 2) The top polyimide layer just acts as an electrically insulating layer and damper and it is 3 µm in thickness. In the following, the design-fabrication is explained briefly for completeness.

The process of fabricating a PMUT array includes oxidation of an SOI wafer and a subsequent active layer (comprising a 200 nm bottom Pt, 1 µm PZT, 200 nm top Pt layer, and a 3 µm thick polyimide insulation just before top electrode deposition, preventing electrodes from shorting) patterning. This is followed by the deposition of polyimide insulating top electrodes which is opened to access pads. Finally, membranes are released by DRIE to complete the fabrication.

Fig. 5.7c shows a close-up image of fabricated PMUT with array elements, the bottom electrode columns, and the top electrode rows. The array consists of 50 × 20 elements spaced at a pitch of 300 µm. Consequently, the combined aperture of the array measures 15 mm × 6 mm, while the overall chip size, inclusive of interconnects, is approximately 27 mm × 8 mm. After dicing, the

array is glued to a PCB and wire-bonded followed by sealing the pads and wires with epoxy (Fig. 5.7b) for application in water or phantoms. The connector on the back of the PCB connects it to a transceiver (Verasonics).

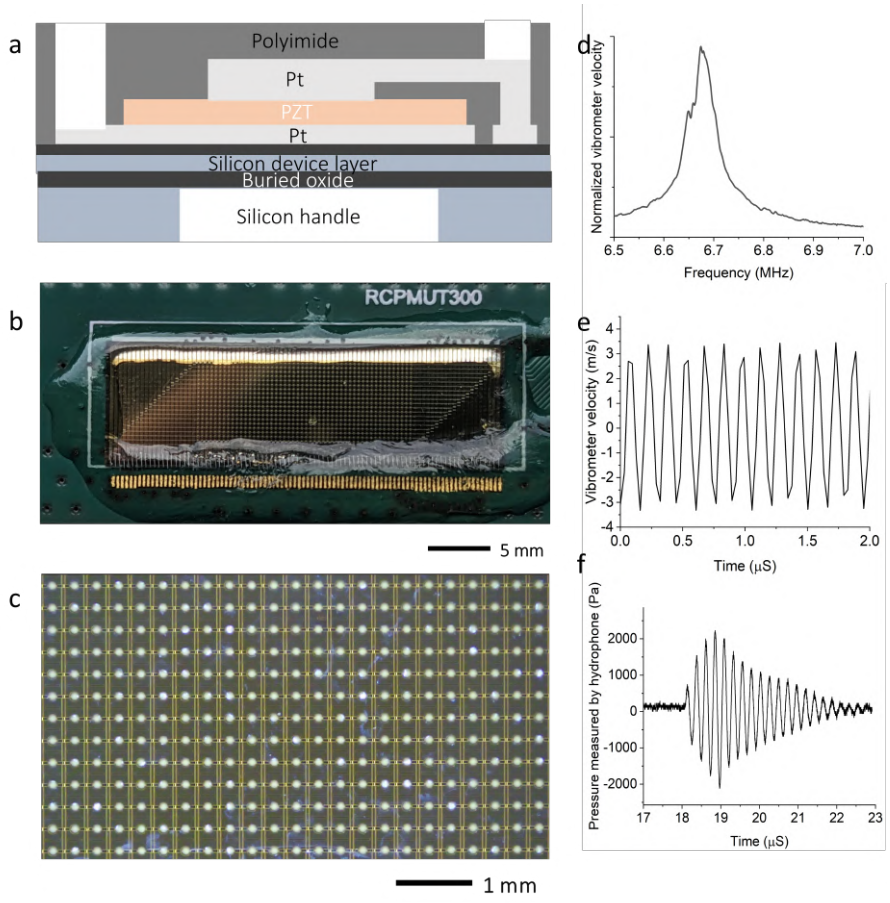

Figure 5.7: Design of RC addressed PMUT on SOI wafer: (a) Single PMUT element schematic (b) array assembly with PCB, and (c) optical microscope image of array elements.**Characterization of RC addressed PMUT on SOI wafer**: LDV characterization of (d) frequency response and (e) time domain response when $5V_{AC} + 5V_{DC}$ is applied. (f) Hydrophone response to 4-cycle square wave burst of 10 V amplitude at 2.5 cm.

Fig. 5.7d shows the frequency response of a single PMUT element from a channel characterized in-air using a laser Doppler vibrometer (LDV) indicating

6.7 MHz resonance frequency and time domain signal in Fig. 5.7e indicates 0.6 m/s/V sensitivity or 15 nm/V displacement of the membrane when and 5 V signal applied along with 5 V DC bias. For underwater characterization, a random PMUT channel is scanned with a 20 Vp-p 4-cycle square wave burst at frequencies between 2 and 6 MHz with a 0.1 MHz step (not shown here). Maximum response is captured by hydrophone at 4.2 MHz indicating the resonance frequency underwater. The scan also suggests about 50 % -6 dB bandwidth, ensuring minimum ringing, required for high axial resolution. Fig. 5.7f shows the captured response by hydrophone at 4.2 MHz, indicating 200 Pa/V at 2.5 cm per channel. Although the results are not shown here, it is observed during measurements that, an application of square wave (instead of sinewave) has enhanced this sensitivity by up to 2 times.

5.6 Conclusion

Fabrication of an RC-addressed 2D PMUT array with 50X20 channels is proposed in this chapter, describing the design and fabrication process in detail. The fabrication scheme is unique due to sol-gel processed PZT on patterned bottom platinum electrodes and an interconnect scheme involving vias allowing all pads for the rows as well as columns to be in line. The fabrication is carried out on a conventional silicon wafer as well as an SOI wafer with minor modifications. The basic functionality of the PMUTs as a transmitter as well as a receiver is confirmed by LDV and hydrophone-based characterizations. Both the PMUTs show similar sensitivities of about 0.5-0.6 m/s/V in-air. Underwater, although the results are shown here in different conditions, the generated pressures are quite similar, when observed at the same distance and excitation. However, the membrane material changes the resonance frequency. PMUT on a conventional silicon wafer with polyimide membrane has a 1.8 MHz resonance and that on an SOI wafer has a 4.2 MHz resonance, underwater.

Chapter 6

Flexible Row-Column (RC) Addressed PMUT Array

This chapter is adapted from a previously published article: Joshi et al. Flexible PZT-Based Row-Column Addressed 2-D PMUT Array, in IEEE TUFFC, vol. 71, no. 11, pp. 1616-1626, Nov.2024 [133].

6.1 Background

Because of the potential of RC addressing, it is worth developing a flexible analogue of the RC designs demonstrated in the last chapter 5. For realizing the device on polyimide substrate, the steps from the chapter 4 are followed and the scheme is shown in Fig. 6.1 for reference. A top-down fabrication strategy flexible PMUT array is proposed with 1) a resonance frequency of 1.5-2 MHz, which is higher in comparison with state-of-the-art flexible PMUTs, and is applicable for low-frequency imaging, 2) piezoceramics (here PZT), and 3) a row-column addressing scheme for the 2D array. The device packaging and characterization as a transmitter as well as receiver are also detailed. Such a platform can enhance the capabilities of polymer-based PMUTs because of the comparatively larger active area and control over individual transducer elements. Further optimization can help push the other performance limits and open possibilities for the use of large-area flexible PMUTs for applications such as non-contact stimulation, biomedical sensing, and imaging at shallow depths.

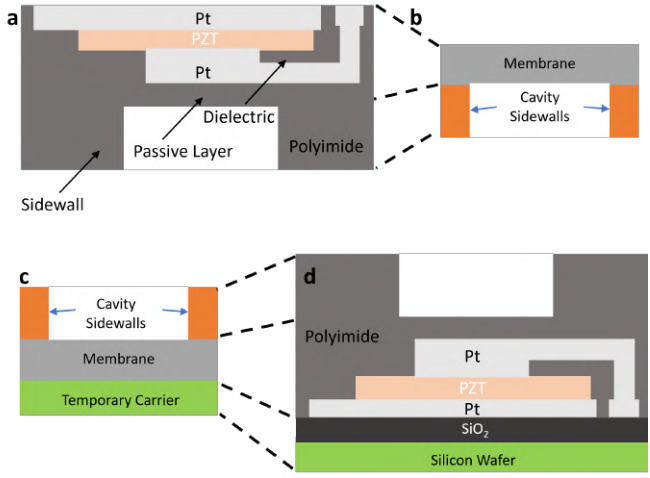

Figure 6.1: (a) Schematic of a flexible PMUT on polyimide. (b) High-level description of a MUT. (c) Simplified layout and (d) detailed stacks of top-down PMUT fabrication scheme (Schematics not to scale).

6.2 Design-Fabrication Scheme

In this study, a row-column addressed 30 × 12 array was designed. The center-to-center pitch between the elements is set as 500 µm, allowing the array operation up to 3 MHz frequency, without any sidelobes in unfocused ultrasound beam patterns [29]. Such design leads to an aperture dimension of 15 mm × 6 mm. The proposed novel design of the top electrode interconnects is shown in Fig. 6.2a. Note that each element of this array has 4 interconnected PMUTs. Including the interconnects and pads, the chip size is 27 mm × 8 mm. The membrane diameter (100 µm) is the same as that used in previous chapters just for ease of fabrication and to establish a process for the working device. A summary of the lateral dimensions for the PMUT is given in Table 6.1.

The 12 rows located at each end of the array, serve as electrode pads for the top electrodes and are replicated in the design and interconnected. The central section consists of 30 rows designated as the bottom electrode rows for the PMUT. Moreover, a unique interconnect scheme can be seen in Fig. 6.2a where 400 µm × 400 µm via-through-polyimide-and-PZT connects the top electrode line along the column to the top electrode pads (along the rows). This simplifies

access to rows and columns using pads in a single line, easing integration with electronics and packaging. The pad line is also duplicated (as seen in Fig. 6.2a on the left and right) and one of them is used during electronics integration.

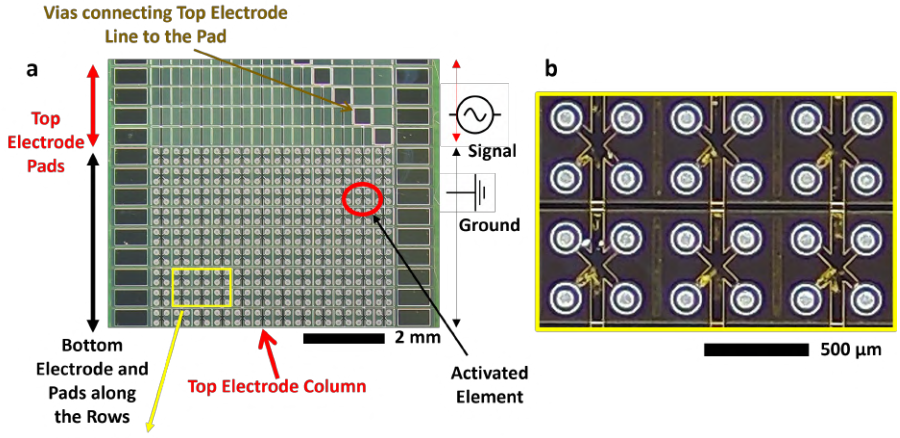

Figure 6.2: (a) Flexible RC addressed PMUT design. (b) Magnified view of a few PMUT elements from the array.

Parameter	Relevant for	Chosen value
Membrane diameter	Resonance frequency, acoustic pressure	160 µm
Electrode diameter	Power consumption and residual stresses	100 µm
Element pitch	Lateral resolution and ultrasound beam pattern	500 µm
Array size	Targeted application areas, for instance, affects imaging footprint in imaging	30×12 (15 x 6 mm)
Chip size	Fabrication cost and application	27 x 8 mm

Table 6.1: Lateral dimensions for the flexible row-column (RC) PMUT

The device fabrication used a top-down method, meaning that the device layers are assembled in reverse order, very similar to the one in chapter 4. Initially, on a temporary carrier, membrane structures are created, followed by cavity sidewalls. The fabrication stack on a silicon wafer carrier is shown in Fig. 6.1d. The step-by-step microfabrication process flow is shown in Fig. 6.3 with schematics and optical microscopic images at each fabrication step.

The fabrication started with wafer cleaning and 35 min wet oxidation at 1100°C resulting in 300 nm oxide on both sides. Then, the bottom Pt layer is patterned with a lift-off process (Fig. 6.3a). After substrate preparation, sol-gel PZT deposition is followed which involves spin coating, pyrolysis, and rapid thermal annealing (RTA). PZT is then patterned for pads and vias by wet etching (Fig. 6.3b). Wet etchants for the PZT are described in [107]. Note that the PZT locally cracks in the area between the adjacent Pt lines at locations where it is deposited on SiO_2 as it does not have the oriented seed layer below as in the case where it is deposited on Pt (and that these cracks do not spread under uniform flexing.). In Fig. 6.3b inset, it is annotated in the small area between Pt lines where these become critical and also clearly visible in the left and bottom parts of the figure. Since the PMUT membranes are to be realized well within the bottom Pt line where PZT does not crack, it might appear that the individual PMUTs are unharmed. While this is true, a potential issue arises with the top electrode line (connecting the top electrode pad to PMUT top electrodes), which runs across the uneven, cracked wafer surface. This can result in electrical discontinuity, making it challenging to access the PMUT top electrodes by applying potential at the pads. A polyimide layer is used to mitigate this challenge and also helps reduce unwanted capacitance and unevenness on the wafer surface. It is patterned to connect the top electrode line to PZT below and the top electrode pads through vias (Fig. 6.3c).

After the sputtered top Pt lines interconnect the PMUT elements and cover the vias that connect the elements to the respective pads (Fig. 3d), the polyimide membrane and sidewall are realized (Fig. 6.3e). Firstly, 7 µm polyimide is deposited by a single spin coating step at 2000 RPM followed by soft baking and curing. Next, spin coating at 2000 RPM followed by soft baking is performed and repeated 4 times. In the following, a single hard baking step is performed which results in another 28 µm cured polyimide. Out of total 35 µm polyimide is deposited, 21 µm thickness is patterned to form a sidewall. The remaining 14 µm is a membrane passive layer ensuring the neutral axis away from the PZT.

Finally, the release procedure involves DRIE on the stack shown in Fig. 6.1d to release the flexible array from the temporary silicon carrier. During the DRIE process, the silicon is etched (in the area just below the arrays) with an etch rate of 0.66 µm/cycle till the oxide color starts appearing when the release process is about to finish (Fig. 6.4a). With further DRIE cycles, the oxide is also removed with an estimated etch rate of 8 nm/cycle (exposed Platinum in Fig. 6.4b which is the same as in the top of Fig. 6.1a). To make sure that no more oxide is left, the wafer is put in the BHF for 5 min which removes any remaining oxide. The array is then separated from the polyimide film attached to the remaining wafer frame by cutting it with a scalpel to complete the fabrication (Fig. 6.4c). The array can be bent with fingers without any PZT cracking (Fig. 6.4d).

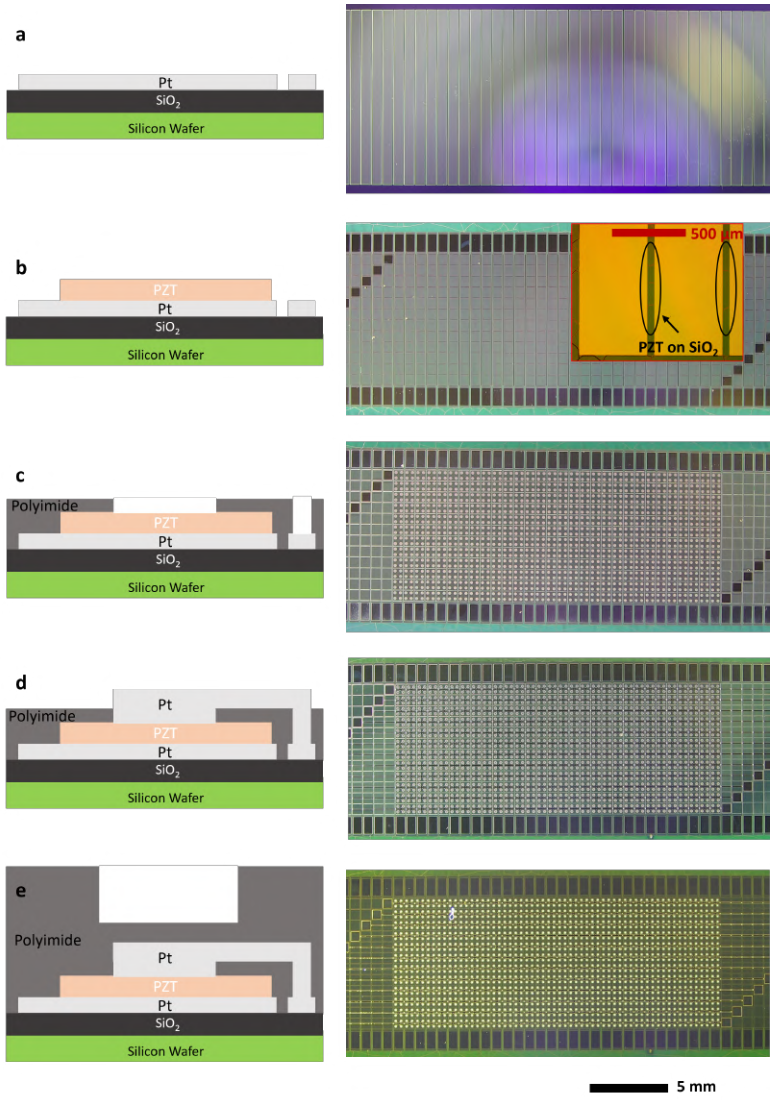

Figure 6.3: Schematics of fabrication steps (left) and corresponding optical microscope images of a 2D array during fabrication (right): (a) Patterning of the bottom Pt layer on thermal oxide. (b) Sol-gel deposited PZT (in the inset, image taken just after PZT deposition) is patterned for pads and vias. (c) Polyimide interlayer patterning for vias and electrodes. (d) Top Pt interconnects patterning. (e) Polyimide membrane and sidewall layer deposition followed by patterning for membrane cavities.

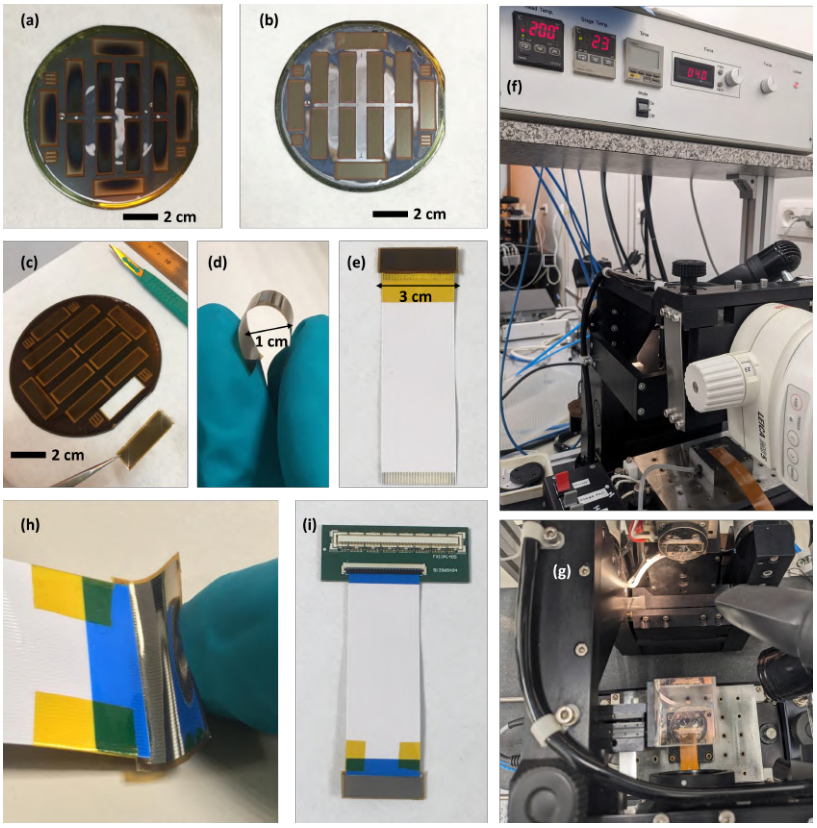

Figure 6.4: Release and packaging of the flexible array: (a) Oxide color appearance during DRIE and (b) Completion of the DRIE after oxide color disappears and Platinum is visible. (c) The flexible arrays being released with a scalpel. (d) The array being bent. (e) The array after bonding to the FFC using anisotropic conductive glue. (f,g) Setup for anisotropic conductive gluing using flip-chip bonder. (h) Flexible PMUT being bent around the other axis. (i) The other end of the FFC plugged into the FFC connector on a rigid PCB.

The array is then bonded to a pitch-matched FFC using anisotropic conductive glue (IQ-BOND 5976-ACE, Roartis) using a flip-chip bonder. The chip is first fixed on the head and the FFC is on the stage. The glue is applied to the FFC and the FFC is aligned with the chip.The head temperature is increased to 200°C. After confirming that the alignment is still intact, the FFC is bonded to the chip by bringing the FFC and the chip in contact with 100 N force for 5 min, establishing the electrical contact (Fig. 6.4e,f,g). Following this, the

chip with the FFC was sealed with 3 µm Parylene-C deposited using a Parylene coater. The array can still be bent around the other axis after bonding (Fig. 6.4h). The other end of the FFC is further plugged into the FFC connector soldered on a rigid PCB for further electronics integration (Fig. 6.4i).

During fabrication runs (also applies for the rigid device from chapter 5), various checks are performed to ensure uniformity and reproducibility. The thickness of each processed layer is primarily measured using a Dektak XT stylus profilometer for layers such as platinum, PZT, the polyimide interlayer, and the sidewall layer, all of which involve patterning. For layers without patterning, such as the oxide layer, the color of the layer is visually inspected, and its thickness is measured optically using a Nanocalc system. Additionally, electrical conductivity checks are carried out whenever a contact is exposed after etching, such as during PZT and polyimide interlayer etching. After polyimide etching, a detailed microscope inspection is also additionally conducted to check for any residue, as this is a primary cause of poor electrical contact. Microscope inspections are performed routinely after every patterning and deposition step to ensure the integrity of the process.

6.3 Results

After parylene sealing, various characterizations are performed, starting with LDV. The elements are accessed using a PCB connected to an external function generator. The in-air (Fig. 6.5a) and underwater resonance frequency (Fig. 6.5b shows the response along with the setup in the inset) are recorded, using periodic chirp excitation, at 2.7 MHz and 2.1 MHz, respectively. No optical corrections are needed to determine underwater resonance frequency. The transmission sensitivity of the PMUTs is measured to be 5 mm/s/V and 20 mm/s/V in-air, without and with 5 V DC bias, respectively (from Fig. 6.5c,d). Although DC bias is not necessary for PMUTs, it is documented in the literature that it significantly improves the performance of PMUTs by increasing the e_31 coefficient and decreasing the permittivity [32]. However, note that no separate poling process is performed on the PZT. The velocity responses can be translated into a displacement response of around 1.2 nm/V with DC bias. The time domain response is also recorded after mounting the transducer on the curved fixture of 8 mm radius (response in Fig. 6.5e along with the setup) and is very similar to that without bending.

Around 50 % in-air crosstalk with neighboring unexcited elements is present when a single element (note that, it is composed of 4 PMUTs) is excited with a periodic chirp signal (Fig. 6.5f). This is higher than the latest rigid row-column

PMUT (literature lacks studies on flexible PMUT crosstalk) which indicates 10 % crosstalk [26]. However, note that neighboring columns (or rows) are not grounded. This is a combination of electrical (capacitive) and mechanical phenomena. Moreover, the PMUT excitation brings the substrate in different vibration modes, and in Fig. 6.5f inset (in red), these vibration peaks of the substrate (it is not a PMUT although it appears like one) are shown. The second adjacent peak in the frequency response from Fig. 6.5a,b could be due to mechanical coupling between the vibrating substrate and PMUTs.

Then, the transmission characterization of a single PMUT element is carried out underwater with a hydrophone (2 mm needle, Precision Acoustics, UK). Fig. 6.6a shows the setup for the hydrophone measurements. The actuation signal was a 10 V 4-cycle sinewave burst at 2 MHz. Fig. 6.6b shows the response of a single PMUT to four cycles of a sinewave burst signal. It measures a transmission response of 250 Pa or 25 Pa/V (division by 10 V actuation amplitude) at 1 cm. The FFT of the time-domain response (inset of Fig. 6.6b) suggests that the transducer has a center frequency of around 2.05 MHz and a bandwidth (BW) of 0.4 MHz, which is about 20% of the center frequency. The center frequency is in line with the design goal of low-frequency imaging and is higher than the flexible PMUT frequencies reported in the literature [53, 54, 85]. However, the bandwidth is lower than the reported rigid PMUTs which demonstrated more than 100 % bandwidth (no comparison with flexible PMUTs is possible) [35]. This needs improvement for imaging applications which can be achieved for instance, by introducing more damping in the membrane [35].

Fig. 6.6c shows the signal acquired after the application of 10 V DC bias on top of the same AC signal and is about 40 Pa/V. Fig. 6.6d shows the transducer mounted on a curved fixture of 20 mm radius. After the device is bonded to the FFC, it is difficult to bend the transducer to smaller bending radii because of the stiffness of the FFC. The signals acquired after applying without and with DC bias application on a bent transducer are shown in Fig. 6.6e,f and are about 22 Pa/V and 32 Pa/V respectively. FFTs of these acquired signals are shown in the inset for completeness (no significant change is observed in the bandwidth of bent PMUT). This shows the working of the transducer underwater after bending and suggest performance enhancement of the transducer with DC bias.

Lastly, to measure the receive sensitivity of the PMUT transducer, a PZT-based 2MHz single-element transducer, PA1497, with a 19 mm diameter (Precision Acoustics, UK) is used to transmit a four-cycle burst signal at 2 MHz. The transmitted signal is measured by the calibrated hydrophone and the PMUT transducer (Setup in Fig. 6.7a). Fig. 6.7b shows the received signal on the oscilloscope from the single element PMUT. The measured hydrophone peak pressure is about 33 kPa. Since the same pressure levels are applied to the PMUTs (by maintaining the same distance and applied burst signal level), the

receive sensitivity is calculated by dividing the voltage signal by the pressure, and a receive sensitivity of about 30 mV/MPa is obtained for the PMUTs.

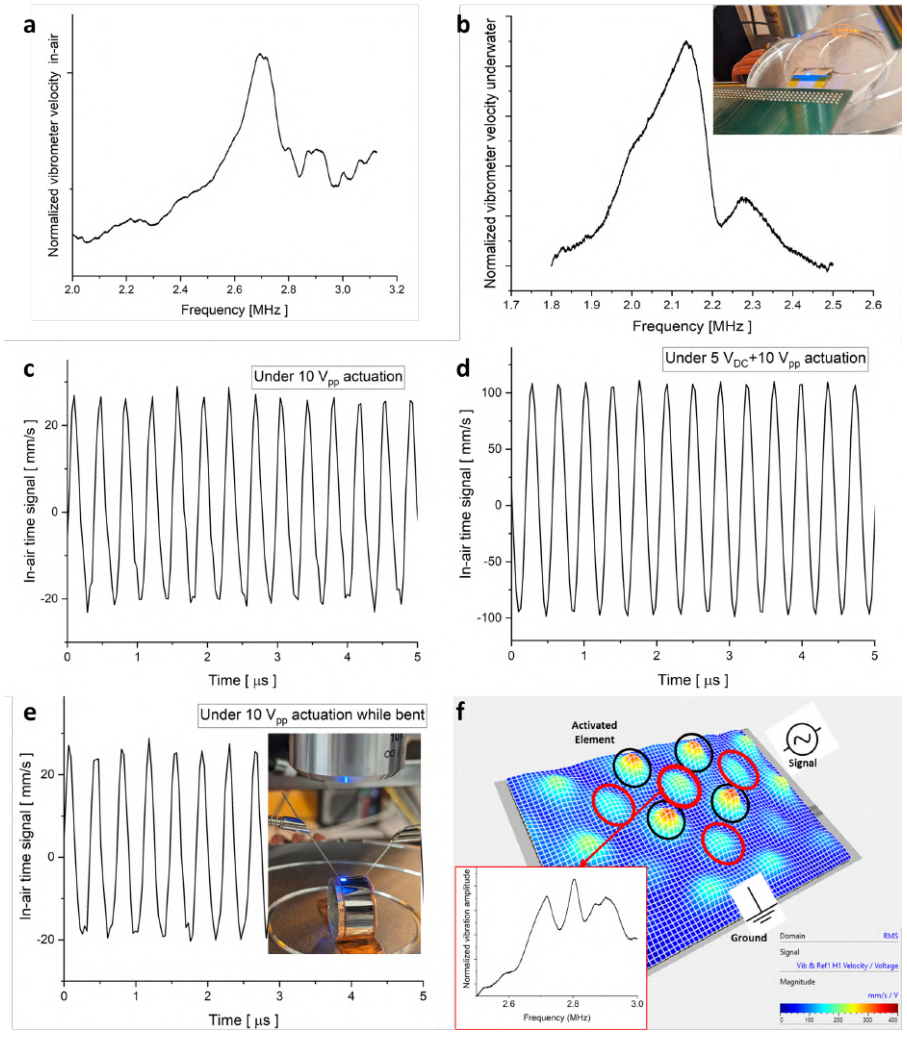

Figure 6.5: LDV characterization of single PMUT element: Frequency response (a) in-air and (b) underwater. Time domain response in-air (c) without DC bias and (d) with DC bias. (e) Setup for LDV characterization with a transducer on a curved fixture. (f) Time domain response in-air under bending conditions. (g) In-air crosstalk analysis. Activated row-column and corresponding element is marked.

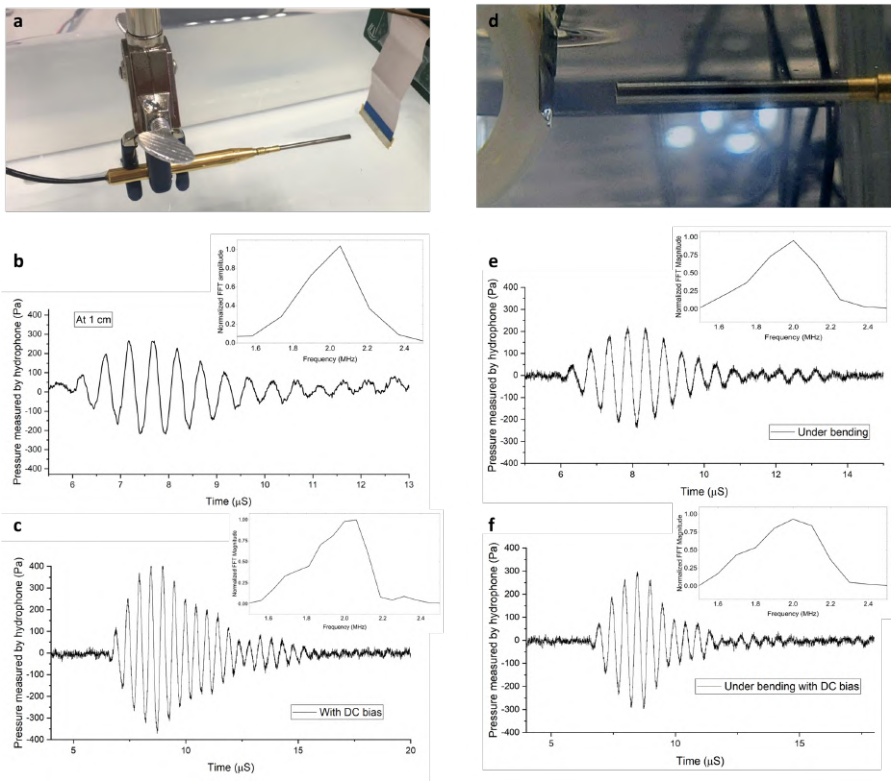

Figure 6.6: Hydrophone measurements at 1 cm along with their FFT in the inset: (a) Setup without bending. The signal received by hydrophone (b) without DC bias and (c) with DC bias. (d) The transducer bent on a curved fixture. Signal acquired (e) without DC bias and (f) with DC bias.

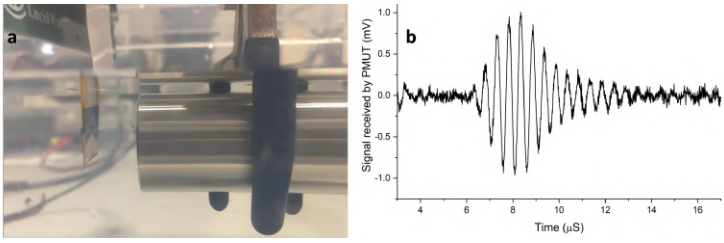

Figure 6.7: (a) Setup showing a single element transducer transmitting ultrasound pulse towards PMUT. (b) The signal received by PMUT

6.4 Updated Design of the Flexible RC PMUT

There are two potential issues identified with the previous design. 1) Low sensitivity because of the small fill factor. 2) Frequency is higher than required for phased array operation. The transducer pitch should be less than half the wavelength [29]. For a 500 µm pitch, the underwater frequency should be tuned around 1.5 MHz. To achieve these goals, the design is modified slightly by increasing the diameter of the membranes to 160 µm. This increases the fill factor and should reduce the resonance frequency of the PMUT device.

The design is simulated in COMSOL and then fabricated followed by characterization. The simulations (Fig. 6.8a,b) indicate a 1.9 MHz frequency in air and a 1.3 MHz resonance frequency, underwater. Note the antiresonance from the in-air simulations. The antiresonance frequency is the frequency at which the impedance of the device reaches a maximum, effectively opposing the driving signal. Less current flows through PMUT resulting in less velocity (membrane displacement) in the mechanical domain (refer to the electrical model of PMUT in Fig. 1.4). This frequency typically occurs slightly above the resonance frequency (where the impedance is minimum).

After device fabrication, preliminary yield tests are carried out. The response of individual PMUTs is initially tested using an LDV on five randomly selected PMUTs to confirm proper functionality. Once the device's operation is verified, it is integrated with a FFC. The alignment is checked with a microscope and electrical connections are then randomly tested on five pads to ensure proper conductivity. If the connections are confirmed to be functional, the device is sealed with a parylene coating to make it waterproof. Following this, the array is connected to a PCB, where it is configured as a linear array by grounding the rows. Finally, channel characterization is performed with a 5 V DC bias.

The in-air resonance frequency is about 1.9 MHz, matching with the simulations whereas the sensitivity ranges from 20-30 mm/s/V across the elements, a bit less than what came out in simulations (Fig. 6.8c,d). There are 3 potential reasons for this discrepancy all of which are limiting voltage transfer to PMUTs: 1) Impedance mismatch: A mismatch between the impedance of the function generator and the impedance of the PMUT channels can result in voltage losses. 2) RC filter Effects: The PMUT interconnects, along with the inherent capacitance of the elements, create RC filtering effects that attenuate the voltage delivered to the PMUTs, when the cutoff frequency of the RC filter is lower than the operating frequency. 3) Parasitic capacitances: Parasitic capacitances from PMUT interconnects, wiring, and the PCB—though generally small—can contribute to additional voltage losses, by increasing the current demand further reducing the effective voltage available to the PMUTs. The reduced input

voltage at the PMUT leads to lower membrane displacement and, consequently, lower sensitivity compared to simulations. Addressing this requires optimizing PMUT interconnects, geometry, and material aspects.

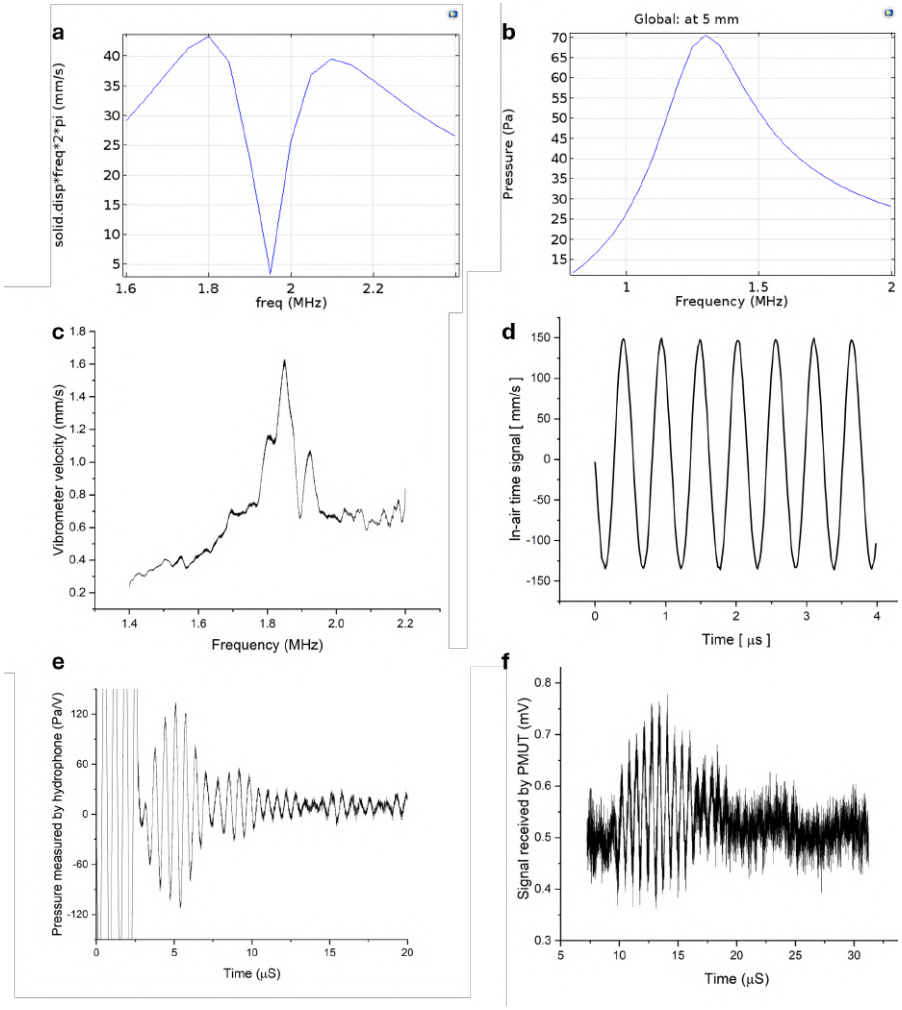

Figure 6.8: Results obtained with an updated design of the flexible RC PMUT: (a) Simulated in-air sensitivity. (b) Simulated underwater pressure (c) In-air frequency response measured by LDV (d) In-air time domain signal measured by LDV (e) Pressure transmitted by PMUT at 5 mm and (c) 5 kPa signal received by PMUT as a receiver.

The underwater resonance frequency closely matches the simulations. The transmitted pressure per channel at 1.3 MHz is about 80-120 Pa/V when measured at 5 mm and that is more than what came out in simulations. This behavior can be explained by crosstalk between neighbouring elements which contributes to additional pressure.The sensitivity variations across the PMUT elements in the array can be attributed to several factors. 1) The dominant reason is the crosstalk between array elements. Typically, central channels of the array have shown sensitivity towards the higher side. 2) Moreover, variations in piezo-electric material thickness and properties across the wafer (refer to chapter 2, Fig. 2.4), could lead to non-uniform sensitivity. 3) Additionally, other fabrication process errors, such as, the non-uniform thickness of polyimide layers can also contribute to differences in performance. 4) Finally, the top electrode deposition and hence interconnect resistance is non-uniform because of non-uniformity in the polyimide interlayer etching (etched via slope varies and exposed PZT surface, sometimes unclean).

The receive sensitivity is characterized by exciting a commercial transducer to produce 5 kPa pressure at 5mm (confirmed by hydrophone) and the signal is received by PMUT and is about 0.03 mV/KPa. The results indicate an appropriate frequency for the phased array operation.

Table 6.2 provides a comparison of this work with major advancements in flexible PMUT technology. In general, flexible PMUTs on a polymer substrate have shown much lower transmit sensitivity compared to the flexible ones on a silicon substrate, possibly because of the significant damping of the vibrations in the polymer (polyimide) sidewall. Optimizing the material stack is required in this case which needs careful consideration of the temperature budget in the process sequence starting from device fabrication to integration and packaging. Despite exhibiting superior transmit sensitivity, flexible PMUTs on silicon substrates remain largely unexplored towards imaging applications. This gap in research likely arises from the formidable challenges associated with array interconnects and electronic integration essential for imaging functionality. Polymer-based approaches can offer better possibilities for array interconnects and electronics integration, in the context of imaging. However, there are no reports regarding polymer-based PMUT arrays suitable for imaging.For instance, a notable polymer-based PMUT approach in [85] reported sensitivities suitable for underwater pulse-echo experiments and successfully demonstrated time-of-flight (ToF) based sugar concentration sensing application. However, the two-element device with a 150 kHz working frequency is not suitable for imaging applications. This work advances the state-of-the-art for flexible PMUTs in several aspects in the context of imaging applications- 1) Unlike most reports with a sub-MHz resonance frequency, this work demonstrates flexible PMUTs with MHz frequency. 2) It is the first flexible 2D PMUT array with an RC

addressing scheme. 3) This research takes the first step towards the rigorous characterization of flexible PMUT sensitivities as is done for rigid MUTs or conventional transducers developed for imaging [35, 134].

Substrate	Piezo material	Membrane diameter (µm)	Membrane thickness (µm)	Array size	Pitch (mm)	Frequency (kHz) (% bandwidth)	Sensitivity	Bending radius (mm)	Proposed application	Author, year
PI	PVDF	700	80	Two element		150 in water	9.3 Pa/V at 12.5 cm		ToF based sensing	Su, 2024
Silicon-PDMS	PZT	700	50	16 x 1	1.1	700		5	Brain Stimulation	Lee, 2017
Silicon	PZT	410	7	Single element with 3 x 3 cells	0.49	426 (1%)	4.5 µm/V	1		Sadeghpour, 2020
PI	**PZT**	**160**	**12**	**30 x 12 Row-column**	**0.5**	**1300 in water (20%)**	**120 Pa/V at 5 mm**	**8**	**Imaging**	**This work**

Table 6.2: Comparison with flexible PMUT state of the art

6.5 Conclusion

Top-down fabrication of a PZT-based RC addressed 2D (30×12) flexible PMUT array is described. The design-fabrication scheme is unique due to sol-gel processed PZT on patterned bottom Pt electrodes and interconnect scheme involving vias allowing all pads for the rows and columns in-line. About 1 µm thick sol-gel processed PZT thin film acts as the active piezoelectric. The flexible PMUT membrane includes the PZT film and a 14 µm polyimide as a passive layer. A sidewall made of polyimide measuring 21 µm in thickness with a cavity of 100 µm in diameter, is realized by RIE. LDV characterization of the PMUT indicates 2.7 MHz and 2.1 MHz as the resonance frequency in-air and underwater, respectively. Excitation of a single PMUT element coupled with 5 V DC bias results in 1.2 nm/V sensitivity in-air. The working of the packaged flexible chip using FFC for electronics integration is demonstrated with underwater characterizations, and also under bending conditions. The performance does not show a noticeable difference after bending. When the PMUT is excited along with a 10 V DC bias, a pressure response of 40 Pa/V at 1 cm is measured underwater using a hydrophone. The recently fabricated PMUT element has an updated membrane diameter of 160 µm and has shown a resonance frequency of 1.9 MHz in-air and 1.3 MHz underwater. In-air sensitivity is about 20-30 mm/s/V across the elements. 80-120 Pa/V transmitted pressure at 5 mm is recorded underwater. The presented results under bending to an 8 mm bending radius show the potential for wearable applications in shallow-depth regions subject to further optimization.

Chapter 7

Ultrasound Imaging using PMUTs

This chapter is adapted from a previously published article: Joshi et al. Imaging with a Row-Column (RC) Addressed PMUT Array, IEEE UFFC-JS 2024 proceedings [135].

7.1 Background

Previous research in imaging applications using PMUTs has predominantly focused on either fully addressed 2D arrays [91] or linear phased arrays [35]. Fully addressed 2D arrays, while providing comprehensive imaging capabilities, face significant challenges concerning a high number of cables and also associated interconnect design. This complexity can impede practical implementation in clinical settings. On the other hand, linear phased arrays, although simpler, are inherently limited to 2D imaging, thus restricting their utility in applications requiring volumetric or 3D imaging. To address these limitations, row-column (RC) addressed arrays have emerged as a viable alternative [136]. However, to date, only one notable study has reported the use of RC PMUT arrays, demonstrating image capture at a shallow depth of 1 mm [92].

This chapter presents several centimeter deep imaging results obtained with the 50×20 rigid RC PMUT arrays demonstrated in chapter 5- RC-addressed array devices built on an SOI wafer (silicon membrane) as well as a conventional silicon

wafer (polyimide membrane). This advancement evidenced by B-mode imaging results, is interesting as it is demonstrated for the first time in literature,

7.2 Pulse-echo Ultrasound Imaging Basics

7.2.1 Imaging Modes

A-mode (amplitude mode) imaging is the simplest form of ultrasound imaging, where the echo amplitudes are displayed as vertical spikes on a one-dimensional plot. Each spike corresponds to the strength of an echo from a specific depth, determined by the time delay between pulse transmission and echo reception. A-mode is primarily used in applications requiring precise distance measurements, such as ocular biometry [137], where spatial resolution along a line is crucial.

In M-mode imaging, the A-mode measurement is repeated in the time domain. With a static transducer and moving object, the signal changes during various acquisitions. This kind of M-mode (motion) imaging yields a 2D image with depth (along a single line) and as a function of time [117].

B-mode (brightness mode) imaging is the most commonly used ultrasound modality, where echo amplitudes are represented as grayscale brightness on a two-dimensional image (on y axis is depth and on x axis is the position in the azimuthal direction [35]. The received echoes from multiple lines are processed to construct an image that represents the spatial arrangement of structures within the field-of-view (FOV). Each pixel's intensity corresponds to the echo strength, enabling visualization of anatomical structures. B-mode images are formed by combining echoes using beamforming which applies time delays to echoes received from various channels to enhance signals from the target region and suppress noise from other areas.

C-mode (constant-depth mode) imaging generates two-dimensional images of structures at a specific depth [138]. After transmitting pulses, echoes from the desired depth are extracted and displayed as a cross-sectional view. C-mode imaging is achieved by selectively gating echoes corresponding to the target depth and can be used for specialized applications, such as visualizing skin lesions or specific tissue layers.

7.2.2 Imaging Strategies

Plane-wave, plane wave compounding (PWC), and single-line transmission (SLT) are the most common imaging strategies, described briefly. The choice

of strategy depends on clinical needs, with plane wave imaging favoring speed, SLT emphasizing resolution, and compounding balancing both. Other advanced strategies involve diverging wave imaging, synthetic aperture imaging, coded excitation imaging, harmonic imaging, etc [139].

Plane-wave imaging transmits a single, unfocused ultrasound pulse (plane wave) across the entire field of view. This approach enables the simultaneous acquisition of echoes from all points along the wavefront, allowing for very high frame rates. However, plane wave imaging has limited spatial resolution due to the lack of beam focusing. Its advantage lies in dynamic applications like cardiac imaging, where temporal resolution is critical.

PWC improves spatial resolution by transmitting multiple plane waves at different angles and combining the received echoes. Each angled plane wave provides unique information, and their compounding enhances image quality by increasing contrast and reducing speckle noise. The number of plane wave emissions and the angular range directly impact the balance between frame rate and image quality. A larger number of emissions and wider angular range improve resolution and contrast but reduce frame rate.

SLT emits focused ultrasound beams sequentially along individual scan lines, providing excellent spatial resolution due to precise focusing. This traditional strategy generates high-quality images but is slower, as only one scan line is acquired per pulse. The number of scan lines determines the image resolution and affects the trade-off between frame rate and detail.

7.2.3 Image Reconstruction

In all these modes, the system transmits short pulses from the transducer, and the received echoes are processed to determine their amplitude, time of flight, and location. Beamforming techniques and signal processing algorithms are used to enhance resolution, suppress noise, and improve image quality. Let's consider the simplest case of the plane wave approach to generate a B-mode image. This involves several critical steps from the transmission of pulses to the processing of received echoes [140]:

Pulse transmission In a plane wave strategy, the transducer array emits a short, unfocused ultrasound pulse. The plane wave propagates uniformly across the FOV (same as the transducer aperture in the lateral and elevation directions, for plane wave strategy), illuminating all structures within its path simultaneously. This ensures that echoes are received from all depths and lateral positions at once, allowing for high temporal resolution and faster imaging.

Echo reception After the transmitted wave interacts with tissue, it is reflected, scattered, or absorbed. The reflected waves, or echoes, return to the transducer elements. Each transducer element (channel) acts as an independent receiver, recording the returning echoes as raw signals. These signals contain information about the amplitude (strength of the echo), and time of flight (depth of the reflecting structure).

Processing received echoes To reconstruct an ultrasound image, several processing steps are performed on the received echoes. When echo signals are received from a particular point in the tissue, each transducer element in the active aperture records the signal at slightly different times due to the varying distances from the point of reflection. To accurately reconstruct the signal, these different signals must be combined in such a way that they arrive at the same time and contribute to the final signal for that point. This process is achieved by applying a time delay to the signals from each element in the aperture. The delay ensures that the signals from all elements are synchronized, meaning they will combine constructively when summed, rather than interfere with each other. This process, known as delay-and-sum beamforming, allows the system to focus on a particular point and produce a clear, accurate signal that represents the structure being imaged.

Next, envelope detection converts the raw RF signals into their amplitude envelopes using techniques like Hilbert transformation or rectification, extracting intensity information from the high-frequency data. To make the data displayable, logarithmic compression reduces the dynamic range of the amplitudes, ensuring that both weak and strong echoes are visible. The resulting data, originally in polar coordinates (angles and depths), undergoes scan conversion, where it is interpolated into a Cartesian grid for proper visualization. Finally, post-processing techniques, such as noise filtering, speckle reduction, and contrast enhancement, further refine the image for improved quality and diagnostic utility.

The final B-mode image represents tissue structures as a grayscale map, where pixel brightness corresponds to the amplitude of the echoes. Strong reflectors (e.g., bone) appear bright, while weaker reflectors (e.g., soft tissue) appear darker. The lateral resolution depends on the beamforming process, and the axial resolution depends on the pulse duration and frequency.

7.3 Experimental Setup

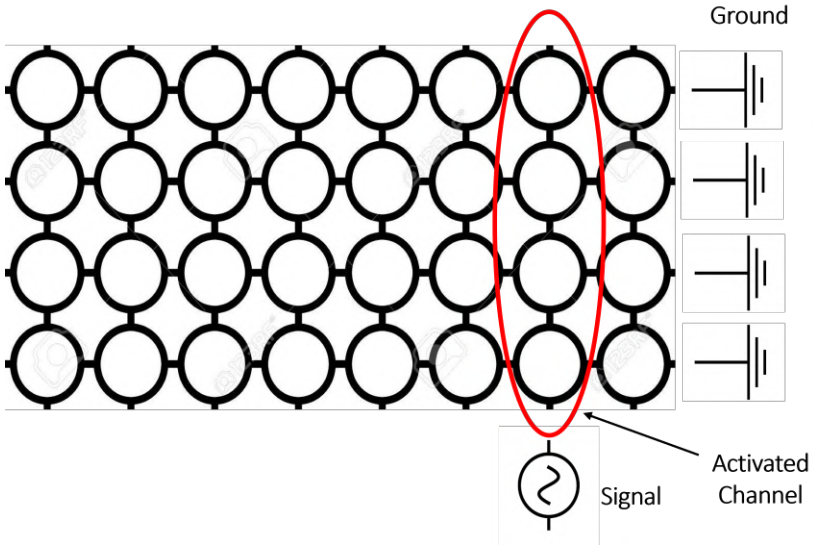

Figure 7.1: Accessing the columns of the RC PMUT array during characterization and imaging experiments.

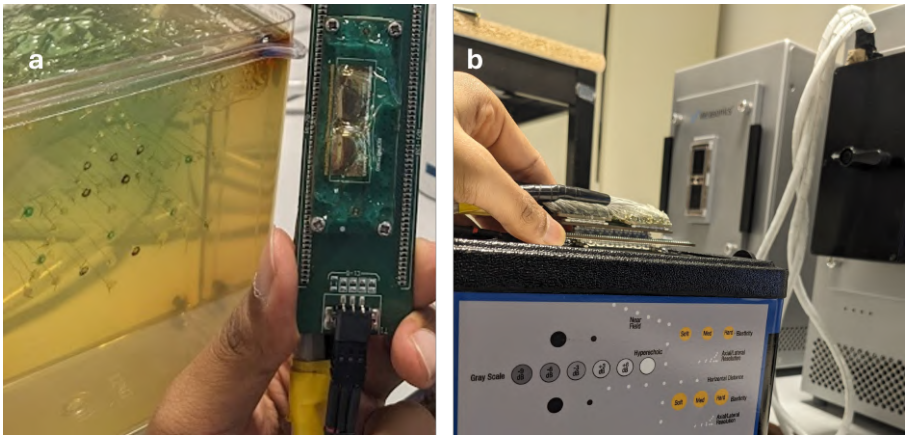

Figure 7.2: (a) Setup showing wire phantom and the PMUT connected to the cable through the connector board with the gel applied. (b) During the imaging experiment, the PMUT connected to the Verasonics transceiver pressed on the tissue mimicking phantom.

Usually, an RC addressing approach employs, for instance, columns during a transmit event and rows during a receive event as they are applied for 3D imaging. Here, instead, the columns are used during transmit as well as receive operations (20 rows were always grounded), as a 50-channel linear array (50×1). Fig. 7.1 explains this schematically with an example of an 8×4 array, transforming it to 8×1. This greatly simplifies the electronics while demonstrating the performance and suitability of the PMUTs for 3D imaging applications of the RC-addressed array, given the switching circuitry is taken care of. Fig. 7.2 shows the setup for imaging experiments conducted with a custom-made metal wire phantom. Verasonics Vantage 256 is used as a transceiver.

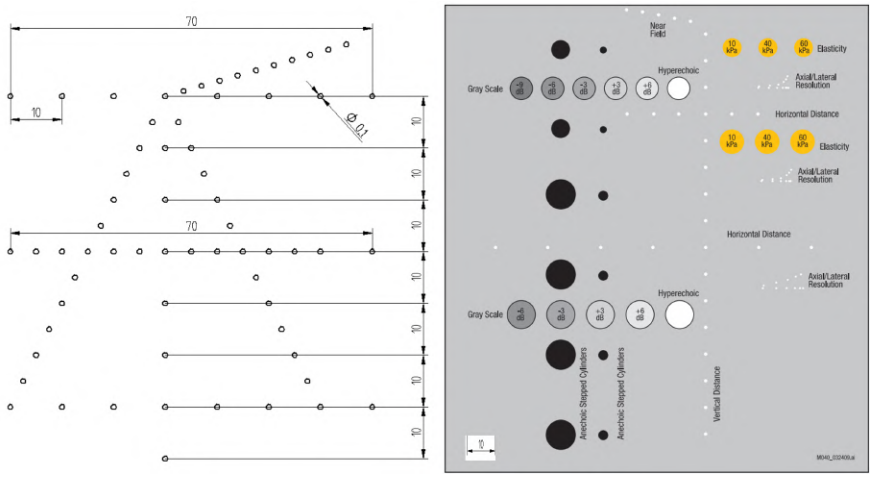

Figure 7.3: Cross sections of the phantoms used- Wire phantom on the left and tissue-mimicking phantom on the right (adapted from [141] and [142])

Another integral apparatus in ultrasound imaging experiments is the ultrasound phantom. Phantoms are specialized tools used in B-mode (brightness mode) ultrasound imaging to evaluate, calibrate, and test the performance of ultrasound systems. They provide a controlled and repeatable environment for assessing system accuracy and image quality. Two common types of phantoms are wire phantoms and tissue-mimicking phantoms (see Fig. 7.3. Note that wires and objects go into the plane) [141, 142]. Wire phantoms consist of thin wires suspended in a medium with acoustic properties similar to soft tissue. These are primarily used to assess spatial resolution, geometric accuracy, and the ultrasound beam profile. The strong reflections from the wires allow precise testing of axial and lateral resolution, transducer alignment, and distance measurement. They are invaluable for analyzing system precision and identifying

distortions or artifacts in the imaging process. Tissue-mimicking phantoms, on the other hand, often include structures resembling blood vessels, lesions, or cysts, enabling comprehensive testing of contrast resolution, depth penetration, and artifact behavior. They are also widely used for operator training and practicing scanning techniques. Together, wire and tissue-mimicking phantoms complement each other in ultrasound system evaluation.

7.4 Imaging with the SOI PMUT

Actuation voltage is set as 10 V_{DC} + 10 V_{AC} at 4.2 MHz. Various algorithms are used to compare the image quality. First, a SLT imaging procedure is set up, using 71 scanning lines along a -30^0 to 30^0 FOV, with a 30 mm focal depth (Fig. 7.4a shows a sector spanning -30^0 to 30^0 with respect to y-axis which is along depth). This employs transmit beamforming. It is the process of applying time delays to signals from different transducer elements to focus the transmitted pulse in a specific direction or at a desired depth. FOV determines the imaged area, and the number of scan lines dictates image detail. Focal depth plays a crucial role in SLT, as the beam's resolution is highest at the focal point. The second imaging procedure is a single plane wave (PW) emission and reception. Finally, a plane wave compounding (PWC) is performed which has combined 10 plane wave emissions spanned across a -10^0 to 10^0 FOV. This uses beam steering where time delays are applied such that the signals from the elements combine coherently at a specific angle. This results in the ultrasound beam being directed in the desired direction, allowing for scanning at different angles. In plane-wave compounding, more emissions negatively impact the frame rate. A smaller angle between consecutive plane wave emissions (i.e., more densely spaced angles) provides more detailed information, but it also increases data acquisition time, reducing the frame rate.

Fig. 7.4 displays a B-mode image of metal wires located at depths of up to 5 cm. Attenuation artifact is observed in all images at higher depths due to a decrease in signal-to-noise ratio (SNR). Typically, SLT results in the highest acoustic pressure and hence should result in the best image quality. However, here, the pitch is more than half the wavelength (0.84 λ) which has probably resulted in the artifacts (Fig. 7.4a). Best image quality is obtained with PWC as shown in Fig. 7.4c. It can be briefly explained as follows. In single-PW acquisition, the ultrasound probe sends out a single wave in one direction. The echoes from this wave are used to form an image, which may suffer from artifacts like speckle noise or limited contrast resolution. In contrast to that, in PWC, Multiple plane waves are emitted in different directions, and the echoes from each wave

are combined. This process enhances the image by averaging out noise and reducing artifacts, leading to better spatial resolution and contrast.

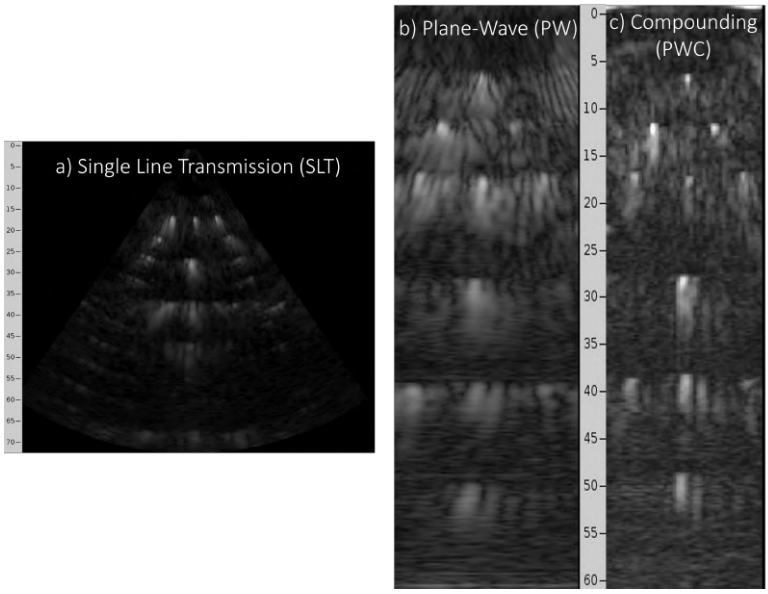

Figure 7.4: Ultrasound images obtained using SOI PMUTs obtained with various algorithms: (a) Single line transmission (SLT) (b) Plane-wave (PW) acquisition, and (c) Plane-wave compounding (PWC). Along the y-axis, imaging depth is indicated in mm.

7.5 Imaging with PMUT on Conventional Wafer

Before presenting imaging results, more characterizations are shown here with tissue-mimicking phantom with 2.5 cm thickness. Scanning using hydrophone 1.3 to 3.8 MHz frequencies with 5 V DC bias (plotted in Fig. 7.5c), the resonance frequency is determined to be around 2.2 MHz where the highest response of about 100 Pa/V is recorded with 66 % - 6 dB Bandwidth. Time domain response without DC bias suggests 50 Pa/V peak pressure at resonance (Fig. 7.5d). Receive operation is performed by exciting a commercial transducer at 2.2 MHz to transmit 9 kPa at 2.5 cm (confirmed by hydrophone) and the same is measured by PMUT indicating 0.1 mV/kPa sensitivity which doubles with 5 V DC bias (Fig. 7.5e). Round trip sensitivities at 2.5 cm with no DC bias and

5 V DC bias are 5 and 20 µV/V (4-fold), respectively. When excited with 10 V DC bias, a 10-fold improvement in round-trip sensitivity can be expected.

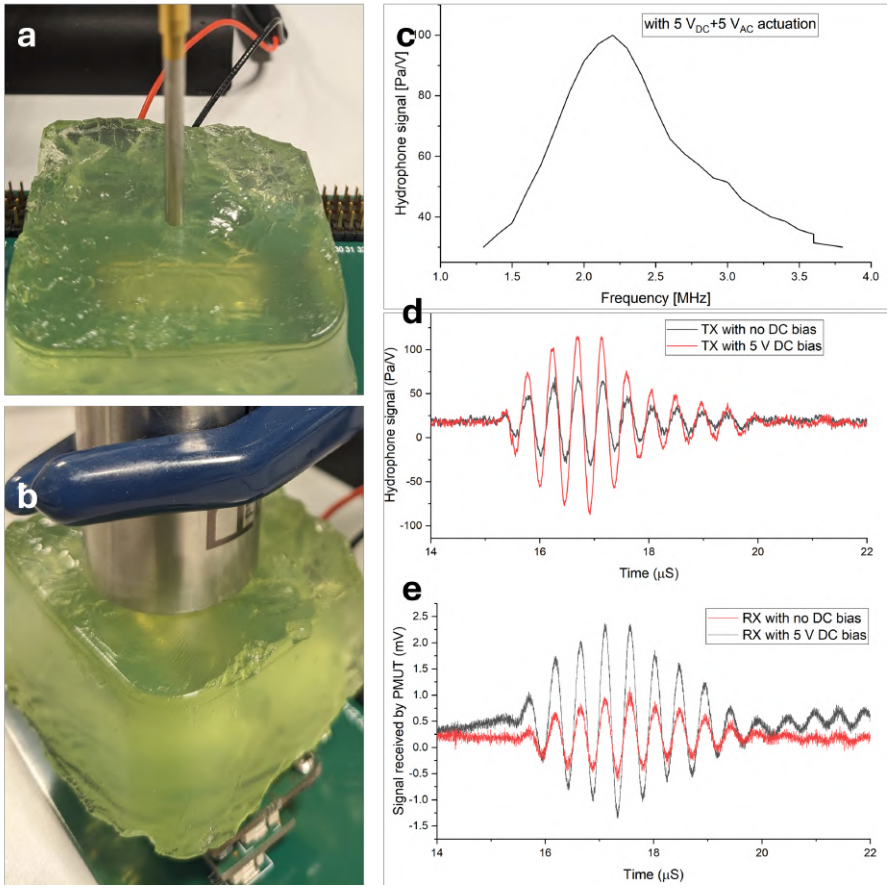

Figure 7.5: Characterizations of rigid PMUTs with polyimide membranes using tissue-mimicking phantom of 2.5 cm thickness: (a) TX setup with needle hydrophone and (b) RX setup with a commercial transducer to transmit 9 kPa 4 cycle pressure wave at 2.2 MHz. (c) TX frequency response and (d) time domain response with 4-cycle sinewave. (e) RX time domain response of the PMUT

Ultrasound images obtained with the novel RC PMUT on a silicon substrate with polyimide membrane are in Fig. 7.6. Actuation voltage is set as 10 V_{DC} + 10 V_{AC} at 2 MHz. Note that, here, the SLT algorithm is used and has resulted

in the best image quality owing to the highest focused pressure and pitch being well below the half-wavelength limit (0.36 λ) in this case. However, the results are yet not at par with medical-grade imaging as the cyst (hyperechoic cyst location can be understood from tissue-mimicking phantom cross-section shown in Fig. 7.3) is not clearly visible in the CIRS phantom image (Fig. 7.6b) and many other objects from the phantom could not be imaged.

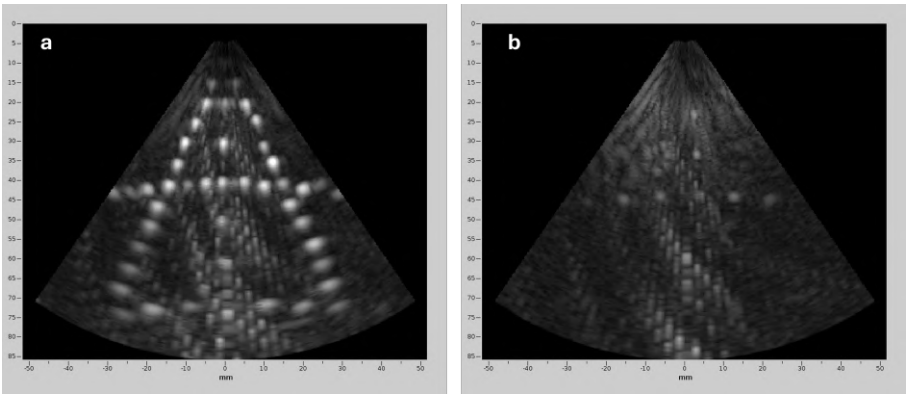

Figure 7.6: Ultrasound imaging using rigid PMUTs with polyimide membranes: (a) metal wire phantom. (b) tissue-mimicking phantom (CIRS).

Another thing that draws attention is the periodic arcs observed in the ultrasound image. It suggests a systemic issue, potentially arising from the DC bias used to enhance the SNR. While a DC power supply can improve SNR by stabilizing the electronics, any instability, such as ripple or noise in the supply, can introduce low-frequency interference into the imaging system. This interference may couple into the analog front-end circuitry, including amplifiers, transducers, or digitizers, resulting in harmonics that manifest as periodic artifacts in the reconstructed image. Additionally, inadequate shielding and grounding could amplify this problem. Poorly shielded transducer cables or connections may act as antennas, allowing external electromagnetic interference (EMI) from the DC supply, nearby electronics, or environmental noise to couple into the system. These distortions can propagate through the imaging chain and appear as systematic artifacts.

Mitigating these issues requires a multi-faceted approach, including the use of ultra-low-noise power supplies with effective ripple suppression, robust shielding of cables and equipment, and ensuring proper grounding. Environmental isolation and diagnostic testing, such as temporarily disconnecting the DC bias can help identify and resolve the root cause.

7.6 Challenges while Imaging with Flexible PMUT

As outlined in the experimental setup of this chapter, all rows of the flexible RC PMUT array are grounded to configure it as a linear array. To evaluate the readiness of the array for imaging experiments, several checks are conducted in the context of yield and uniformity:

1. Capacitance and Resistance Measurement: The capacitance of each array channel is measured, and is considered acceptable if their capacitance is within a 20% tolerance range. If an element falls outside this range, its resistance is also measured. A resistance value greater than $100\,k\Omega$ indicates that the channel is still usable. This step provides an initial estimate of the number of operational channels in the array.

2. Hydrophone Measurements: If more than 80% of the channels are functional, hydrophone measurements are performed to evaluate the acoustic response of individual channels. These measurements have shown that when capacitance values are within tolerance, the corresponding acoustic pressure response is typically consistent at approximately 100 Pa/V at a distance of 1 cm, again within a 20% tolerance range. On average, about 80% of the channels in tested arrays meet these criteria. Only arrays meeting this threshold are subsequently connected to Verasonics for imaging experiments.

3. Impedance Testing with Verasonics: As a final quality check, impedance testing is conducted using Verasonics. These results have consistently corroborated the findings from the capacitance and hydrophone measurements.

Despite these thorough checks, imaging experiments using the flexible PMUT arrays developed in this thesis have been unsuccessful. Two primary challenges contribute to the difficulty in achieving ultrasound imaging with these arrays at their current stage of development.

7.6.1 Low Sensitivity

The flexible PMUT channel (last row from Table 7.1) demonstrates transmit sensitivities around 10 dB (around 3 times) lower than the rigid one after normalizing the distance. This is because of two dominant reasons 1) polyimide sidewalls associated with more damping. 2) [111] oriented PZT (developed in this thesis) with 2-3 times lower e_{31} coefficient, compared with the [100] PZT (gold standard).

Moreover, to access the imaging capability of these PMUTs, a quantitative performance analysis can be carried out. For instance, with 120 Pa/V transmit

sensitivity at 5 mm, and 0.03 µV/Pa receive sensitivity per channel, round trip sensitivity per channel (FOM) is 3.6 µV/V. Using 30 channels to perform transmit beamforming can improve the sensitivity at most by about 10 times (considering 25% of the channels are short, 25 % could not have high-pressure sensitivity and electronic focusing is not optimal because the array is not ideally flat), amounting to 0.036 mV/V. The Verasonics system noise level is about 0.3 mV RMS (0.425 mV peak) and the medium attenuation is about 0.5 dB/MHz/cm as reported by Sadeghpour et al. in [90]. Even after assuming negligible attenuation of the medium, to detect highly reflecting objects such as metal wires even at 5 mm, more than 10 V is necessary.

# channels, pitch (µm)	Center frequency (MHz), -6 dB bandwidth (%)	Transmit sensitivity (Pa/V)	Receive sensitivity (µV/Pa)	Round-trip sensitivity (FOM) @ 1 cm (µV/V)	Imaging depth	Study
1 x 128, 214	1.5, 184	430 Pa/V @ 3 cm	0.19	250	12 cm	Sadeghpour, 2022, Comm. PZT
4 x 64, 175	5, 30	1 kPa/V @ 2 cm	---	---	4 cm	Dausch, 2014, Acetate PZT
1 x 15, 70	7.5, ---	1.2 kPa/V @ 0.5 cm	6	3600	0.5 cm	Liu, 2020, Epi PZT
1 x 64, 300	2.5, 81	312.5 Pa/V @ 3.6 cm	3.2	3600	16 cm	Savoia, 2021, STM PZT
1 x 50, 300	**2, 60**	**100 Pa/V @ 2.5 cm**	**0.2**	**50**	**4 cm**	**Rigid-flex RC PMUT POC, In-house PZT**
1 x 30, 500	**1.3, 20**	**120 Pa/V @ 0.5 cm**	**0.03 (w/o DC)**	**3.6**	**N/A**	**Flex RC PMUT POC, In-house PZT**

Table 7.1: Comparison of the rigid-flex and flexible PMUT developed in this thesis with state of the art rigid PMUTs which demonstrated imaging [35, 91, 143, 144]

The comparison of the flexible PMUT array performance with conventional ultrasound transducers [136] and rigid SOI-based PMUTs [35,92] for high-quality imaging applications (detecting tissues or working in attenuating mediums) suggests a significant technological maturity gap. For example, conventional technology has dominated the medical imaging market because the probes can deliver high acoustic pressures and receive echoes with high SNR. Moreover, flexible counterparts of conventional technology, with the use of piezo composites have successfully reported imaging capabilities [2]. The rigid SOI-based PMUTs have also demonstrated in-vivo imaging or at least proof-of-concept (POC) for imaging applications using phantoms or metal objects at voltages as low as 20-30 Vp-p [35,91,143,144]. Table 7.1 summarizes the PMUT imaging state-of-the-art in detail. However, state-of-the-art polymer-based PMUTs, including this thesis, are not yet there because their sensitivities are lower than the above-mentioned imaging technologies. As an example, in [35], imaging has been performed

with a transmit sensitivity of 490 Pa/V at 3 cm and a receive sensitivity of 0.19 µV/Pa. Such sensitivities make the transducers a good starting point for medical imaging. The measured transmit sensitivity is 80-120 Pa/V at 5 mm and the receive sensitivity is 0.03 µV/Pa for the device demonstrated here. Hence, at least 10 times FOM improvement is required to establish a POC for imaging applications (this matches the FOM for rigid-flex PMUT from this thesis) whereas at least 10 times improvement in both transmit and receive sensitivities (100 times FOM) would be recommended for medical imaging.

7.6.2 Other Operational Challenges

The 10 dB pressure improvement can result from higher applied voltage and bias, for instance, 20 V each (in case sensitivity improvement is challenging). However, here comes the limitation from the material side. The PZT thin film developed (refer to chapter 2) starts to break down beyond 12 V. If one PMUT element is shorted (meaning PZT below a single circular electrode breaks down), the entire channel containing that element becomes unusable. The defects in PZT should be reduced to sustain twice the voltage at a few MHz frequencies. Moreover, already some of the array channels are damaged at the PZT deposition stage because of bad (as deposited) PZT quality.

After fabrication is completed, FFC integration brings another challenge. Too much or too little glue, and asymmetry while vacuuming the chip and FFC might result in no electrical connection. About 80% of the channels work properly without being short or not connected when checked at this stage (by measuring capacitance and acoustic pressure as explained before).

After imaging trials, electrodes are found to be getting corroded and parylene looks swollen. This has not been usual during hydrophone measurements in water with sinewave excitation of a single channel. This means that the ultrasound gel reaches through the sealing to the electrodes when all channels are fired during SLT using a square wave excitation. This could be related to parylene encapsulation as this is not observed for the rigid PMUTs encapsulated with polyimide and epoxy.

Additionally, it is worth noting a tradeoff between sensitivity and robust packaging at this moment. Typically, thicker encapsulation would result in robust waterproof sealing. However, this adds to damping, reducing the sensitivity.

To summarize, the high-level solutions would be:

1) Material level: Developing [100] oriented PZT with better piezo-electric properties and reducing PZT defects to have more working channels and sustain 20 V operational voltage

2) Device level: Adding more channels to the array and also improving acoustic pressure per channel with, for instance, hexagonal arrangement with more channel aperture and fill factor [92] and secondly, improving single PMUT sensitivity by reducing damping. This could, for instance, involve optimizing the material stack.

3) Integration and packaging level: A more robust FFC integration process should be developed and the polyimide-epoxy encapsulation process can be developed for the flexible PMUTs, with minimal effects on the transducer performance.

7.7 Conclusion

The rigid RC PMUT arrays achieved imaging depths of up to 3-5 cm at voltages as low as 10 V_{DC} + 10 V_{AC}. The results showed that plane wave compounding (PWC) provided the best image quality for the device on the SOI wafer where the pitch is 0.84 λ. Imaging at a similar voltage is reported here for the first time with RC PMUTs on conventional silicon wafers with polyimide membranes with single-line transmission (SLT) where the pitch is 0.36 λ. However, the transducer performance needs to be improved significantly for medical imaging. Unfortunately, flexible PMUT arrays with sensitivities about 10 dB lower than that of rigid PMUTs face significant challenges in performing any imaging. The lower sensitivity can be partially countered with an improved array design. The design along with an efficient encapsulation strategy will be implemented in the future.

Chapter 8

Summary and Future Work

8.1 Key Contributions

8.1.1 PZT Material Developemnt

A novel in-house lead-zirconate-titanate (PZT) solution and a sol-gel thin film process is developed and characterized elaborately. Moreover, it is used to fabricate various PMUT arrays. PZT quality is evidenced by the imaging results obtained with rigid arrays.

The PZT sol-gel preparation and deposition methods are successfully developed, with methanol identified as the optimal solvent for solution stability and desired coating properties. A single-layer coating thickness of 160-170 nm is obtained with 0.4 M solution concentration. An excess lead addition of 15% has minimized the pyrochlore phase. By tuning the PVP porogen concentration to 0.05 gm/mM of PZT, stress is further reduced, resulting in a stable 1 µm PZT crack-free film after six coating layers. XRD analysis has confirmed the preferred [111] orientation, due to the highly oriented [111] Pt seed layer, 200 nm in thickness. DBLI measurements have revealed a coercive field of approximately 7 V/µm (or 70 kV/cm), a remnant polarization of about 15 µC/cm^2, a $d_{33,f}$ of 60 pm/V, a breakdown voltage of 100 V, and a dielectric constant of 1000. FOM for the developed material with these values is about 2.5-3 GPa. A comparison with the state of the art suggests there is a scope of 2-3 times improvement of piezoelectric coefficients (5-10 times FOM at material level) which in turn suggests a need for [100]-oriented PZT development.

These optimized PZT thin films address the critical challenges of obtaining crack-free oriented films with thickness control and demonstrating strong potential for applications in piezo-MEMS, sensors, and actuators. The quality is evidenced by ultrasound imaging performed with PMUTs having the PZT film. This work provides a foundation for future research on enhancing PZT performance and exploring scalability for broader piezo-MEMS applications.

8.1.2 Rigid and Flexible Fully Addressed Arrays

Rigid and fully flexible PMUTs are fabricated with polyimide membranes in 8x8 fully addressed array format. A rigid 11x11 fully addressed array is being developed.

Low-cost, SOI-free technology for PZT-based fully addressed PMUT arrays, with its innovative interconnect design, fabrication strategy, and detailed characterization is presented in this thesis. The use of a polyimide membrane as the passive layer allows for tunable resonance frequencies, achieved by adjusting polyimide thickness. The PMUT membranes are fabricated using backside DRIE with an oxide etch stop. The potential of the technology for imaging applications is suggested by a 70% fractional bandwidth centered around the primary frequency.

Expanding on this platform and with the same interconnect design, bendable PMUTs are developed using a substrate-last method, with polymer substrates such as polyimide and SU8 offering flexibility. A temporary silicon carrier enables flexible PMUT arrays with a 1 µm PZT and 6 µm polyimide in the membrane. The sidewall cavities are defined by RIE or photolithography. Testing reveals that polyimide-based PMUTs offer better bendability. On the other hand, for the PMUT on SU8, it turns out that residual stresses in SU8 influence device performance, and an in-depth study is required on this aspect which is part of future work. Nevertheless, a PMUT on the SU8 substrate is fabricated for the first time and the novel fabrication flow of PZT-based flexible PMUTs on polyimide is established.

8.1.3 Imaging with Rigid Row-Column (RC) Addressed PMUT on a Conventional Silicon Substrate

For the first time, a rigid 50x20 RC addressed PMUT array is developed with polyimide membranes on a silicon substrate without SOI wafers, and its imaging capability is demonstrated.

The rigid RC-addressed 2D PMUT arrays, with configurations of 50x20 channels, are fabricated on both conventional silicon and SOI wafers, leveraging a unique sol-gel PZT process on patterned platinum electrodes and an innovative interconnect design with vias. These rigid PMUTs have demonstrated comparable sensitivities of 0.5–0.6 m/s/V in air whereas the resonance frequency has varied based on substrate type- PMUTs with polyimide membranes on silicon wafers at 1.8 MHz, while those on SOI wafers at 4.2 MHz, underwater. Ultrasound imaging has been performed with both PMUTs at an imaging depth of 3-5 cm at voltages as low as $10V_{DC} + 10V_{AC}$. The devices on SOI substrate with 0.84 λ pitch have shown the best ultrasound image quality using pulse-wave compounding (PWC). Most interestingly, for the first time in literature, PMUTs on conventional silicon wafers with polyimide membranes have demonstrated ultrasound imaging results. The PMUTs with 0.36 λ pitch have demonstrated the best image quality with the single line transmit (SLT) technique, at similar voltage levels. While there is a promise for imaging, further performance enhancements are needed to meet medical imaging standards.

8.1.4 PZT-based Flexible Row-Column Addressed PMUT

A PZT-based flexible RC PMUT is fabricated for the first time and characterized underwater as a transmitter and receiver. The waterproof packaging and connections to a transceiver are established.

A flexible PZT-based 30x12 RC addressed array is fabricated using a top-down approach on a polymer (polyimide) substrate, for the first time, with a similar fabrication strategy as one used for a fully addressed array. With the recent design having 160 µm wide membranes with 1 µm PZT film and a 14 µm polyimide passive layer, the flexible PMUTs have a resonance frequency of 1.9 MHz and 24 mm/s/V sensitivity in-air. The array is bonded to a pitch-matched FFC using anisotropic conductive glue and the chip with the FFC is sealed with 3 µm Parylene-C. The other end of the FFC can further be plugged into the FFC connector soldered on a rigid PCB for further electronics integration. The PMUT channels have indicated underwater pressures of 80–120 Pa/V at 5 mm and receive a sensitivity of 0.03 mV/kPa, at 1.3 MHz resonance frequency. Characterizations under bent conditions have confirmed that the underwater sensitivity is unaffected at an 8 mm bending radius. Due to lower sensitivity (10 times lower FOM than rigid PMUTs) and integration-packaging concerns, ultrasound imaging has not yet been successfully performed with these PMUTs. This suggests the need for further optimization for potential wearable applications in shallow-depth regions, which brings us to future work directions.

8.2 Future Work Directions

8.2.1 Modeling and Simulations of Flexible PMUT

The piezoelectric material properties play a significant role in determining the transducer's performance characteristics and hence, in this thesis, piezoelectric material properties are characterized and incorporated into the simulation model. However, understanding and controlling residual stresses are also paramount to ensure device reliability and performance consistency. Also, residual stress development in the multilayer fabrication and release process can be investigated and incorporated in design and simulations for more accurate modeling and understanding of the device, its resonances, and sensitivities. Crosstalk as well as substrate vibrations in flexible PMUTs can be studied for desired array operation. Also, this calls for in-depth modeling and simulations at the array level.

A starting step in this direction is lumped electrical modeling. For this, electrical characterization of the arrays can be carried out using impedance analysis. Solving the electrical model helps in two ways- 1) Gives an in-depth perspective about the device. 2) This would help optimal circuit development and improvement of SNR from the circuit side.

8.2.2 Quality Assessment and Improvement to Enable Imaging with Flexible PMUT

The thesis demonstrates an in-depth characterization of flexible PMUTs (resonance frequency, sensitivity, etc.) and gives insights into yield and reproducibility assessment. Moreover, other important challenges related to scalability, and reliability are briefly mentioned. However, there is a scope to take these aspects forward and get improved results.

Sensitivity Low sensitivity is the most critical reason which hinders demonstrating ultrasound imaging POC.

Developing [100] oriented PZT with 2-3 better piezo-electric properties (5-10 times FOM at the material level) is a fundamental step towards sensitivity improvement.

Moreover, There is a scope for improvement on the design-fabrication side- 1) Adding more channels to the array and also improving acoustic pressure per channel with, for instance, hexagonal arrangement with more channel aperture

and fill factor [92]. 2) Improving single PMUT sensitivity by reducing damping. This could, for instance, involve optimizing the material stack.

Also, during packaging, the polyimide-epoxy encapsulation process can be developed for the flexible PMUTs, where care needs to be taken to have minimal effects on the transducer sensitivity.

Yield Yield focuses on the percentage of functional devices produced during fabrication. It is affected by defects or failures at specific stages of the manufacturing process. This is as such assessed in the thesis in various chapters (e.g., LDV testing, random electrical tests on Pads after FFC integration, capacitance, impedance, and hydrophone measurements, to check the percentage of functional channels). The critical challenges in the context of yield are summarized below which guides further process improvements.

Defects in PZT thin films: Already some of the array channels are damaged at the PZT deposition stage because of bad (as deposited) PZT quality. If one PMUT element is shorted (meaning PZT below a single circular electrode breaks down), the entire channel containing that element becomes unusable. These defects hence directly reduce the fabrication yield. Improving film deposition quality and reducing contamination are critical to addressing this issue.

Errors in chip-to-FFC integration: Integration problems such as misalignment, insufficient or excessive adhesive, or poor vacuum bonding can cause electrical disconnections, leading to non-functional channels. These issues directly impact the yield during the assembly stage. Optimized bonding processes are necessary to ensure high-yield integration.

Reproducibility Reproducibility tests focus on ensuring repeatable measurements during fabrication processes and characterization results as discussed in previous chapters (e.g., thickness measurement, microscope inspections, electrical conductivity checks, PZT wafer maps, capacitance, and hydrophone measurements response within a certain tolerance). The processes developed in the thesis are by and large, reproducible. However, some challenges can be identified related to the variability within the batch which can affect the reproducibility:

Variability in PZT properties: Inconsistent PZT deposition results in variations in piezoelectric properties across the wafer, affecting performance metrics like sensitivity and voltage tolerance. Ensuring uniform film deposition quality and reducing contamination are critical to addressing this issue. Using in-line characterization techniques ensures uniformity across batches.

Polyimide etching and top electrode deposition variability: The top electrode deposition and hence interconnect resistance is non-uniform because of non-

uniformity in the polyimide interlayer etching. Etched via slope varies and exposed PZT surface, sometimes unclean. Standardized processes can reduce this variability and improve reproducibility.

Reliability Reliability is concerned with the long-term operational performance and durability during tests and under real-world conditions. Flexible PMUTs tend to fail over time when subjected to prolonged multi-channel operation, particularly under square wave excitation and DC bias. The reliability issues can be broken down into three parts.

Waterproof sealing failures: Failures in waterproof encapsulation cause electrode corrosion during use and deteriorates the device's reliability. Transitioning to more robust materials like polyimide-epoxy and hence refining the encapsulation process can address this issue.

Electromigration: Electromigration is another possible cause for unreliable performance in flexible PMUTs, as their thin-film metal interconnects are highly susceptible to atomic migration under high current densities. The problem is exacerbated due to the additional mechanical stresses from bending (even while testing under 'flat' conditions, the device is not maintained perfectly flat). Combined with high-frequency operation, the thermal and electrical stresses further enhance electromigration, leading to resistance change, open circuits, or short circuits in the interconnects. To improve electromigration reliability in flexible PMUTs, strategies like optimizing interconnect geometry, and reducing operating current densities, are the way forward.

PZT breakdown at high-frequency operation with DC bias: PZT can break down at high frequencies with DC bias, even at standard operating voltages of 10–12 Volts. The breakdown risk increases due to the combined effects of static and dynamic stresses. The AC component induces periodic polarization and mechanical strain. Rapid oscillations induce mechanical fatigue, while resonance effects amplify stress and vibration. While the DC component creates a constant electric field that aligns dipoles improving piezo-electric properties, it also accelerates degradation due to heating caused increased leakage currents. Additionally, the DC bias exacerbates field concentration around material defects, making the PZT more susceptible to dielectric breakdown. To improve reliability in such conditions, strategies like optimizing the DC and AC voltages, minimizing defect density, and enhancing thermal management are essential.

To have a better perspective on reliability,

1) Device-level characterizations: Stress testing under realistic operational conditions with temperature monitoring can play a critical role in identifying thermal buildup. Additionally, rigorous testing during continuous operation under both flat and bending conditions can provide valuable insights into the

effects of mechanical stress from bending on device performance.

2) System-level characterizations: SNR and power consumption are two critical FOMs at the system level. The depth characterization of these aspects is an important step towards developing a reliable system.

Scalability Scalability refers to the ability to maintain performance, yield, and reliability when transitioning to larger arrays. It also focuses on system and application-level challenges beyond the scope of individual device fabrication. The scalability aspects can be summarized as follows:

Bending radius: Experiments to determine minimum radius-of-curvature should be carried out. This would help scale the design in future iterations to make it suitable for applications with more stringent bending radius requirements, such as IVUS.

Voltage handling capacity of PZT: The current PZT films break down beyond 10-12 V, possibly due to material defects, limiting their usability in higher-voltage scenarios. Note that the breakdown of PZT at individual PMUT elements renders entire channels non-functional. To scale to larger arrays with higher operational demands, PZT materials need to handle up to 20 V without failure. This requires advancements in material development and deposition techniques.

Challenges of multi-channel operation from ultrasound system and interconnects: Dense arrays with a large number of elements offer finer control over the ultrasound beam, thereby holding significant potential to enhance imaging quality. However, current research systems are typically limited to handling up to 1024 channels, restricting fully addressed matrix arrays to a maximum size of 32×32 elements. Realizing such devices also presents significant challenges, particularly in interconnect layouts. An RC addressed arrays can overcome these limitations, and provide a scalable alternative, enabling arrays as large as 512×512 elements with the same 1024-channel configuration. This array size is generally sufficient for most ultrasound imaging applications. Looking ahead, the development of a 64×64 RC addressed array is currently underway as part of future work (see Fig. 8.1).

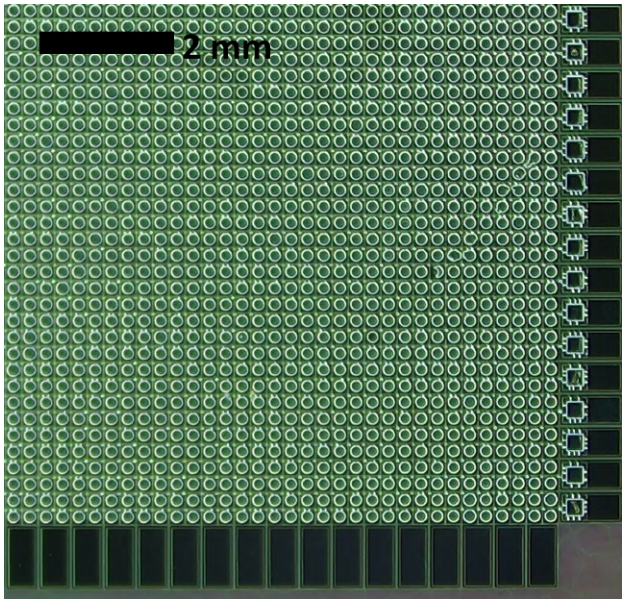

Figure 8.1: Part of 64 x 64 row-column addressed PMUT array.

8.2.3 3D Imaging with Rigid PMUT

Towards 3D imaging, another interesting direction could be scaling the fully addressed rigid 2D array. The main challenge in an 8 × 8 array with 0.3 mm pitch (Chapter 3) is the insufficient aperture required for imaging applications. The total aperture is about 2.4 mm × 2.4 mm which along with about 10% fill factor cannot generate high pressures required for imaging. Hence, as an optimization run, an 11×11 array is designed with a 0.5 mm pitch and 25% fill factor. This is achieved with the arrangement that each element of the 11 × 11 array is composed of 7 cells connected in parallel and 6 of them are placed on a hexagon with one at the center to generate higher pressure. Moreover, the membrane diameter is increased to 0.11 mm to decrease the resonance frequency as well as increase the acoustic pressure because of the higher active area. Additionally, the design is further improved with the introduction of a polyimide interlayer (similar to the one explained in row-column addressed rigid PMUT explained in chapter 5) to decrease the parasitic capacitance due to interconnects. Without the interlayer, the parasitic capacitance is around 5-10 nf and is quite large in comparison with the PMUT capacitance of 1-2

nF. Fabrication and characterization of the array are underway. Fig. 8.2 shows the design of the array. Note that, such designs have limited scaling capability considering challenges to layout interconnects as evidenced in the figure.

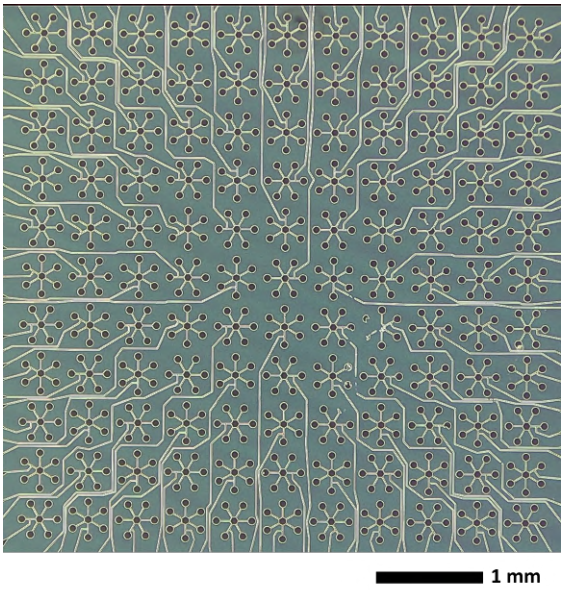

Figure 8.2: Design of the 11 x 11 fully addressed PMUT array.

8.2.4 Circuit Development and Optimzation

While the row-column PMUT transducer itself is integral to imaging, the accompanying electronics play a crucial role in realizing its full potential. Row-column PMUT, for 3D imaging, uses orthogonal elements during transmit and receive. For instance, a row transmits ultrasound and the echo is received along a column. To implement such a scheme, all columns need to be grounded during transmit, and rows during receive phases. These ground-switching capabilities are not readily integrated into current prototype ultrasound systems, but they can be developed and connected externally.

Another challenging circuit design task is to explore the integration of all electronics, including batteries, microcontrollers, and wireless data transfer units, into a patch with the transducer. Patch integration simplifies device usage and enhances portability, opening up new possibilities for medical imaging applications, for instance, continuous monitoring of cardiac activity [17].

8.2.5 Biocompatible and Environmentally-Sustainable Material Development

Focusing on environmental sustainability and biocompatibility aspects, an interesting research direction could be to investigate lead-free alternatives such as KNN, Al-ScN ceramics, and PVDF polymers with comparable performance: Currently, the sol-gel PZT process is established. However, the material contains lead questioning its environmental viability. Considering the experience of sol-gel processing, developing the KNN sol-gel deposition and patterning process is attempted. Some preliminary steps are explained next.

KNN sol-gel process is a slightly adapted version of the process described in [145]. As metal precursors sodium acetate (Sigma Aldrich), potassium acetate (Sigma Aldrich), and niobium ethoxide (Fisher Scientific) are selected. Methanol (Sigma Aldrich) is again chosen as a solvent. 1,3 propanediol and acetylacetone (Sigma Aldrich) are used as stabilizers. The preparation begins by dissolving sodium and potassium acetate with a 20% excess (5 times the mM of KNN) in 1,3-propanediol, at 90°C, for about 10-15 minutes. This excess compensates for the loss of alkali elements during thermal treatment. Next, a stoichiometric quantity of niobium ethoxide is stabilized by adding acetylacetone (again, 5 times the mM of KNN). The two solutions are then combined and stirred at 90°C for 30 minutes. Finally, the sol concentration is adjusted to 0.4 M by adding methanol. Finally, 1 hr stirring after PVP addition and filtering made the stock solution ready. The stock is stable while observed for a month.

Similar to PZT, the KNN solution is deposited on the wafer by spin coating at 3000 RPM, followed by pyrolyzing at 360°C for 1 min, and RTA at 700°C. Thickness is found to be around 150-200 nm per layer. The film is not cracked however, the reflectivity is not as good as PZT thin film. Further development is underway.

In parallel, another more fundamental area that could be explored is biodegradable piezoelectric materials like peptides, cellulose, and gelatin for improved biocompatibility and environmental sustainability. Biocompatibility is essential for medical applications, and biodegradable materials offer additional advantages in certain scenarios such as implantable applications. These have piezoelectric properties similar to PVDF but are more biocompatible and safer.

8.3 A Concluding Perspective

The flexible PMUTs developed in this thesis still face challenges concerning sensitivity and waterproofing, which need to be addressed to fully realize their

potential for ultrasound imaging. Nevertheless, this work advances the state-of-the-art for flexible PMUTs in several aspects in the context of imaging applications- 1) Unlike most reports with a sub-MHz resonance frequency, this work demonstrates flexible PMUTs with MHz frequency. 2) It is the first flexible 2D PMUT array with an RC addressing scheme. 3) This research takes the first step towards the rigorous characterization of flexible PMUT sensitivities as is done for rigid MUTs or conventional transducers developed for imaging [35,134].

Beyond an ultrasound transducer, the potential of the flexible PMUT fabrication, release, and packaging process described in the thesis is worth exploring. Here, the fabrication process demonstrates the incorporation of PZT piezoceramics in polymer-based devices which is usually challenging. This opens the possibility to use other piezoceramics in this process flow. Other polymer-based piezoelectric materials can also easily be incorporated as they do not present challenges such as cracking experienced in this work. Moreover, considering the environmental impact and potential biocompatibility concerns with PZT, one may use other biocompatible piezoceramic or polymer material in this process flow in the context of implantable medical applications, enhancing the overall viability of the technology [18]. Piezoelectric sensors for a different application, such as pressure sensors, could use a similar platform. Besides piezo-MEMS, the release platform can be used in other sensing schemes, such as in capacitive devices or piezo-resistive devices.

In comparison with conventional approaches, here, the MEMS processing allows power-efficient and high-density arrays with finer pitches in a cost-effective process. The flexible RC PMUTs described in this thesis are separated by 250 µm (even lower pitch is possible as the lateral dimensions are not at the critical limits). The advantage over rigid MUTs is the bendability of thin polyimide devices without being fragile. The lightweight and conformable nature of the transducer could lead to the development of wearable ultrasound imaging and sensing systems after performance improvements. The user-friendly technology could have significant implications for remote patient monitoring, home healthcare, and telemedicine, enabling real-time imaging and diagnostics without bulky equipment and mechanical scanning.

However, achieving such pioneering goals requires addressing technical limitations, such as those outlined in this thesis. To achieve this, further investment in R&D on flexible PMUT-based technologies is required. In the recent research domain of flexible ultrasound transducers, flexible piezoelectric transducers dominate [2, 17, 117] whereas flexible CMUTs are emerging [50]. Flexible PMUTs remain the most recent one with significant optimization challenges. With sustained research, flexible PMUTs could close the gap with flexible CMUTs and unlock new opportunities in wearable biomedical imaging and sensing to aid diagnostics and disease prevention.

Bibliography

[1] Sanjog Vilas Joshi, Sina Sadeghpour, Nadezda Kuznetsova, Chen Wang, and Michael Kraft. Flexible micromachined ultrasound transducers (MUTs) for biomedical applications. *Microsystems & Nanoengineering*, 11(1):1–21, January 2025. Publisher: Nature Publishing Group.

[2] Chonghe Wang, Xiaoyu Chen, Liu Wang, Mitsutoshi Makihata, Hsiao-Chuan Liu, Tao Zhou, and Xuanhe Zhao. Bioadhesive ultrasound for long-term continuous imaging of diverse organs. *Science*, 377(6605):517–523, July 2022.

[3] X. Zhuang, D. Lin, Ö Oralkan, and B. T. Khuri-Yakub. Fabrication of Flexible Transducer Arrays With Through-Wafer Electrical Interconnects Based on Trench Refilling With PDMS. *Journal of Microelectromechanical Systems*, 17(2):446–452, 2008.

[4] Muhammad A. Alam and Satish Kumar. Flexible Electronics. In Bharat Bhushan, editor, *Encyclopedia of Nanotechnology*, pages 860–865. Springer Netherlands, Dordrecht, 2012.

[5] I-Chun Cheng and Sigurd Wagner. Overview of Flexible Electronics Technology. In William S. Wong and Alberto Salleo, editors, *Flexible Electronics: Materials and Applications*, pages 1–28. Springer US, Boston, MA, 2009.

[6] Mingzhi Zou, Yue Ma, Xin Yuan, Yi Hu, Jie Liu, and Zhong Jin. Flexible devices: from materials, architectures to applications. *Journal of Semiconductors*, 39(1):011010, January 2018. Publisher: IOP Publishing.

[7] Júlio C. Costa, Filippo Spina, Pasindu Lugoda, Leonardo Garcia-Garcia, Daniel Roggen, and Niko Münzenrieder. Flexible Sensors—From Materials to Applications. *Technologies*, 7(2), 2019.

[8] A. Nathan, A. Ahnood, M. T. Cole, S. Lee, Y. Suzuki, P. Hiralal, F. Bonaccorso, T. Hasan, L. Garcia-Gancedo, A. Dyadyusha, S. Haque, P. Andrew, S. Hofmann, J. Moultrie, D. Chu, A. J. Flewitt, A. C. Ferrari, M. J. Kelly, J. Robertson, G. A. J. Amaratunga, and W. I. Milne. Flexible Electronics: The Next Ubiquitous Platform. *Proceedings of the IEEE*, 100(Special Centennial Issue):1486–1517, 2012.

[9] Bruce W. Drinkwater and Paul D. Wilcox. Ultrasonic arrays for non-destructive evaluation: A review. *NDT & E International*, 39(7):525 – 541, 2006.

[10] Timothy J. Mason. Ultrasonic cleaning: An historical perspective. *Ultrasonics Sonochemistry*, 29:519–523, March 2016.

[11] Sina Sadeghpour, Sebastian Meyers, Jean Pierre Kruth, Jozef Vleugels, Michael Kraft, and Robert Puers. Resonating shell: A spherical-omnidirectional ultrasound transducer for underwater sensor networks. *Sensors (Switzerland)*, 19(4):1–18, 2019.

[12] Yongqiang Qiu, Han Wang, Christine E. M. Demore, David A. Hughes, Peter Glynne-Jones, Sylvia Gebhardt, Aleksandrs Bolhovitins, Romans Poltarjonoks, Kees Weijer, Andreas Schönecker, Martyn Hill, and Sandy Cochran. Acoustic devices for particle and cell manipulation and sensing. *Sensors (Basel, Switzerland)*, 14(8):14806–14838, August 2014. Publisher: MDPI.

[13] P. Kleinschmidt and V. Magori. Ultrasonic remote sensors for noncontact object detection. *Siemens Forschungs und Entwicklungsberichte*, 10(2):110–118, January 1981.

[14] Lei Zhao and Yipeng Lu. Piezoelectric Micromachined Ultrasonic Transducers for Consumer Electronics Applications. In *2023 7th IEEE Electron Devices Technology & Manufacturing Conference (EDTM)*, pages 1–3, March 2023.

[15] Hongjie Hu, Xuan Zhu, Chonghe Wang, Lin Zhang, Xiaoshi Li, Seunghyun Lee, Zhenlong Huang, Ruimin Chen, Zeyu Chen, Chunfeng Wang, Yue Gu, Yimu Chen, Yusheng Lei, Tianjiao Zhang, NamHeon Kim, Yuxuan Guo, Yue Teng, Wenbo Zhou, Yang Li, Akihiro Nomoto, Simone Sternini, Qifa Zhou, Matt Pharr, Francesco Lanza di Scalea, and Sheng Xu. Stretchable ultrasonic transducer arrays for three-dimensional imaging on complex surfaces. *Science Advances*, 4(3), 2018. Publisher: American Association for the Advancement of Science _eprint: https://advances.sciencemag.org/content/4/3/eaar3979.full.pdf.

[16] Chonghe Wang, Xiaoshi Li, Hongjie Hu, Lin Zhang, Zhenlong Huang, Muyang Lin, Zhuorui Zhang, Zhenan Yin, Brady Huang, Hua Gong, Shubha Bhaskaran, Yue Gu, Mitsutoshi Makihata, Yuxuan Guo, Yusheng Lei, Yimu Chen, Chunfeng Wang, Yang Li, Tianjiao Zhang, Zeyu Chen, Albert P. Pisano, Liangfang Zhang, Qifa Zhou, and Sheng Xu. Monitoring of the central blood pressure waveform via a conformal ultrasonic device. *Nature Biomedical Engineering*, 2(9):687–695, September 2018.

[17] Muyang Lin, Ziyang Zhang, Xiaoxiang Gao, Yizhou Bian, Ray S. Wu, Geonho Park, Zhiyuan Lou, Zhuorui Zhang, Xiangchen Xu, Xiangjun Chen, Andrea Kang, Xinyi Yang, Wentong Yue, Lu Yin, Chonghe Wang, Baiyan Qi, Sai Zhou, Hongjie Hu, Hao Huang, Mohan Li, Yue Gu, Jing Mu, Albert Yang, Amer Yaghi, Yimu Chen, Yusheng Lei, Chengchangfeng Lu, Ruotao Wang, Joseph Wang, Shu Xiang, Erik B. Kistler, Nuno Vasconcelos, and Sheng Xu. A fully integrated wearable ultrasound system to monitor deep tissues in moving subjects. *Nature Biotechnology*, pages 1–10, May 2023. Publisher: Nature Publishing Group.

[18] Laiming Jiang, Yang Yang, Ruimin Chen, Gengxi Lu, Runze Li, Jie Xing, K. Kirk Shung, Mark S. Humayun, Jianguo Zhu, Yong Chen, and Qifa Zhou. Ultrasound-Induced Wireless Energy Harvesting for Potential Retinal Electrical Stimulation Application. *Advanced Functional Materials*, 29(33):1902522, 2019. _eprint: https://onlinelibrary.wiley.com/doi/pdf/10.1002/adfm.201902522.

[19] Paul Hamelmann, Massimo Mischi, Alexander F. Kolen, Judith O. E. H. van Laar, Rik Vullings, and Jan W. M. Bergmans. Fetal Heart Rate Monitoring Implemented by Dynamic Adaptation of Transmission Power of a Flexible Ultrasound Transducer Array. *Sensors*, 19(5), 2019.

[20] R. S. Singh, S. Natarajan, M. Lee, A. E. Dann, B. P. Cox, D. B. Bennett, E. R. Brown, H. Lee, W. S. Grundfest, and M. O. Culjat. Development of an ultrasound imaging system for needle guidance. In *2009 IEEE International Ultrasonics Symposium*, pages 1852–1855, 2009.

[21] Fu Li, Umberto Villa, Nebojsa Duric, and Mark A. Anastasio. A Forward Model Incorporating Elevation-Focused Transducer Properties for 3-D Full-Waveform Inversion in Ultrasound Computed Tomography. *IEEE transactions on ultrasonics, ferroelectrics, and frequency control*, 70(10):1339–1354, October 2023.

[22] V. Pashaei, A. Roman, and S. Mandal. Conformal Ultrasound Transducer Array for Image-Guided Neural Therapy. In *2018 IEEE Biomedical Circuits and Systems Conference (BioCAS)*, pages 1–4, 2018.

[23] W. Liu, C. Zhu, D. Wu, and T. Yu. Flexible Piezoelectric Micro Ultrasonic Transducer Based on a Laser Processed Substrate. In *2020 IEEE International Ultrasonics Symposium (IUS)*, pages 1–4, 2020.

[24] Tom Carter, Sue Seah, Ben Long, Bruce Drinkwater, and Sriram Subramanian. UltraHaptics: Multi-point mid-air haptic feedback for touch surfaces. In *UIST 2013 - Proceedings of the 26th Annual ACM Symposium on User Interface Software and Technology*, pages 505–514, October 2013.

[25] Haptic feedback: the next step in smart interfacing, Available at https://www.imec-int.com/en/imec-magazine/imec-magazine-june-2020/haptic-feedback-the-next-step-in-smart-interfacing.

[26] Amr Gamal, Javed Ahmed, and Gary Mintz. Coronary Intravascular Ultrasound (IVUS). page 37. September 2017.

[27] M. O. Culjat, A. E. Dann, M. Lee, D. B. Bennett, P. G. Schulam, H. Lee, W. S. Grundfes, and R. S. Singh. Transurethral ultrasound catheter-based transducer with flexible polyimide joints. In *2009 IEEE International Ultrasonics Symposium*, pages 2209–2212, 2009.

[28] K. Nakamura. *Ultrasonic Transducers: Materials and Design for Sensors, Actuators and Medical Applications*. Woodhead Publishing Series in Electronic and Optical Materials. Elsevier Science, 2012.

[29] K. K. Shung and M. Zippuro. Ultrasonic transducers and arrays. *IEEE Engineering in Medicine and Biology Magazine*, 15(6):20–30, 1996.

[30] Jiaqi Wang, Zhou Zheng, Jasmine Chan, and John T. W. Yeow. Capacitive micromachined ultrasound transducers for intravascular ultrasound imaging. *Microsystems & Nanoengineering*, 6(1):73, August 2020.

[31] Yoon Young Kim and Young Eui Kwon. Review of magnetostrictive patch transducers and applications in ultrasonic nondestructive testing of waveguides. *Ultrasonics*, 62:3 – 19, 2015.

[32] Nan Wu, Xiaotian Zou, Jingcheng Zhou, and Xingwei Wang. Fiber optic ultrasound transmitters and their applications. *Measurement*, 79:164 – 171, 2016.

[33] R. S. Singh, M. O. Culjat, S. P. Vampola, K. Williams, Z. D. Taylor, H. Lee, W. S. Grundfest, and E. R. Brown. P3D-6 Simulation, Fabrication, and Characterization of a Novel Flexible, Conformal Ultrasound Transducer Array. In *2007 IEEE Ultrasonics Symposium Proceedings*, pages 1824–1827, 2007.

[34] T. R. Meeker. Thickness mode piezoelectric transducers. *Ultrasonics*, 10(1):26–36, 1972.

[35] Sina Sadeghpour, Sanjog Vilas Joshi, Chen Wang, and Michael Kraft. Novel Phased Array Piezoelectric Micromachined Ultrasound Transducers (pMUTs) for Medical Imaging. *IEEE Open Journal of Ultrasonics, Ferroelectrics, and Frequency Control*, 2:194–202, 2022.

[36] Kaustav Roy, Joshua En-Yuan Lee, and Chengkuo Lee. Thin-film PMUTs: a review of over 40 years of research. *Microsystems & Nanoengineering*, 9(1):1–17, July 2023. Number: 1 Publisher: Nature Publishing Group.

[37] Muhammed Sabri Salim, M. F. Abd Malek, R. B. W. Heng, K. M. Juni, and Naseer Sabri. Capacitive Micromachined Ultrasonic Transducers: Technology and Application. *Journal of Medical Ultrasound*, 20(1):8–31, 2012.

[38] Butrus T. Khuri-Yakub and Omer Oralkan. Capacitive micromachined ultrasonic transducers for medical imaging and therapy. *Journal of micromechanics and microengineering : structures, devices, and systems*, 21(5):54004–54014, May 2011.

[39] Chang Beom Eom and Susan Trolier-McKinstry. Thin-fi lm piezoelectric MEMS. *MRS Bulletin*, 37(11):1007–1017, 2012.

[40] Dragan Damjanovic. Lead-Based Piezoelectric Materials. In Ahmad Safari and E. Koray Akdoğan, editors, *Piezoelectric and Acoustic Materials for Transducer Applications*, pages 59–79. Springer US, Boston, MA, 2008.

[41] Meysam T. Chorsi, Eli J. Curry, Hamid T. Chorsi, Ritopa Das, Jeffrey Baroody, Prashant K. Purohit, Horea Ilies, and Thanh D. Nguyen. Piezoelectric Biomaterials for Sensors and Actuators. *Advanced Materials*, 31(1):1802084, 2019. _eprint: https://onlinelibrary.wiley.com/doi/pdf/10.1002/adma.201802084.

[42] Peter Eccardt and Kurt Niederer. Micromachined ultrasound transducers with improved coupling factors from a CMOS compatible process. *Ultrasonics*, 38:774–80, April 2000.

[43] T. Liu, J. N. Kim, S. E. Trolier-McKinstry, and T. N. Jackson. Flexible Thin-Film PZT Ultrasonic Transducers. In *2018 76th Device Research Conference (DRC)*, pages 1–2, 2018.

[44] Paul Suetens. *Fundamentals of Medical Imaging*. Cambridge University Press, 2 edition, 2009.

[45] Nimrod M. Tole. Basic physics of ultrasonographic imaging, https://www.who.int/publications/i/item/9241592990.

[46] Ramona Luca, Leonardo Forzoni, Francesca Gelli, and Jeffrey Bamber. An educational overview of ultrasound probe types and their fields of application. *Archives of Acoustics*, 46:3–15, March 2021.

[47] Wonseok Lee and Yongrae Roh. Ultrasonic transducers for medical diagnostic imaging. *Biomedical Engineering Letters*, 7, March 2017.

[48] O. Casula, C. Poidevin, G. Cattiaux, and Ph. Dumas. Control of Complex Components with Smart Flexible Phased Arrays. *AIP Conference Proceedings*, 820(1):829–836, 2006. _eprint: https://aip.scitation.org/doi/pdf/10.1063/1.2184612.

[49] K. A. Wong, S. Panda, and I. Ladabaum. Curved micromachined ultrasonic transducers. In *IEEE Symposium on Ultrasonics, 2003*, volume 1, pages 572–576 Vol.1, 2003.

[50] Amirhossein Omidvar, Edmond Cretu, Robert Rohling, Mark Cresswell, and Antony J. Hodgson. Flexible PolyCMUTs: Fabrication and Characterization of a Flexible Polymer-Based Capacitive Micromachined Ultrasonic Array for Conformal Ultrasonography. *Advanced Materials Technologies*, 8(5):2201316, 2023. _eprint: https://onlinelibrary.wiley.com/doi/pdf/10.1002/admt.202201316.

[51] Chang Peng, Huaiyu Wu, Seungsoo Kim, Xuming Dai, and Xiaoning Jiang. Recent Advances in Transducers for Intravascular Ultrasound (IVUS) Imaging. *Sensors*, 21(10), 2021.

[52] A. Caronti, A. Coppa, A. Savoia, C. Longo, P. Gatta, B. Mauti, A. Corbo, B. Calabrese, G. Bollino, A. Paz, G. Caliano, and M. Pappalardo. Curvilinear capacitive micromachined ultrasonic transducer (CMUT) array fabricated using a reverse process. In *2008 IEEE Ultrasonics Symposium*, pages 2092–2095, 2008.

[53] Jin Hyung Lee, Il Joo Cho, Kyungmin Ko, Eui Sung Yoon, Hyung Ho Park, and Tae Song Kim. Flexible piezoelectric micromachined ultrasonic transducer (pMUT) for application in brain stimulation. *Microsystem Technologies*, 23(7):2321–2328, 2017. Publisher: Springer Berlin Heidelberg.

[54] Sina Sadeghpour, Bram Lips, Michael Kraft, and Robert Puers. Bendable Piezoelectric Micromachined Ultrasound Transducer (PMUT) Arrays Based on Silicon-On-Insulator (SOI) Technology. *Journal of Microelectromechanical Systems*, 29(3):378–386, 2020. Publisher: IEEE.

[55] Alexandre Halbach, Pieter Gijsenbergh, Yongbin Jeong, Wouter Devriese, Hang Gao, Margo Billen, Guilherme B Torri, Christopher Chare, David Cheyns, Xavier Rottenberg, and Veronique Rochus. Display Compatible PMUT Array for Mid-Air Haptic Feedback. *2019 20th International Conference on Solid-State Sensors, Actuators and Microsystems and Eurosensors XXXIII, TRANSDUCERS 2019 and EUROSENSORS XXXIII*, (June):158–161, 2019. ISBN: 9781728120072 Publisher: IEEE.

[56] Christopher Chare, Pieter Gijsenbergh, Yongbin Jeong, Paul Heremans, Jan Genoe, and David Cheyns. High performance large-area polymeric PMUT phased arrays in air. In *2022 IEEE International Ultrasonics Symposium (IUS)*, pages 1–4, 2022.

[57] Pieter Gijsenbergh, Alexandre Halbach, Yongbin Jeong, Guilherme Brondani Torri, Margo Billen, Libertario Demi, Chih-Hsien Huang, David Cheyns, Xavier Rottenberg, and Veronique Rochus. Characterization of polymer-based piezoelectric micromachined ultrasound transducers for short-range gesture recognition applications. *Journal of Micromechanics and Microengineering*, 29(7):074001, July 2019.

[58] Joseph Blackmore, Shamit Shrivastava, Jerome Sallet, Chris R. Butler, and Robin O. Cleveland. Ultrasound Neuromodulation: A Review of Results, Mechanisms and Safety. *Ultrasound in Medicine & Biology*, 45(7):1509 – 1536, 2019.

[59] Jan Kubanek. Neuromodulation with transcranial focused ultrasound. *Neurosurgical Focus*, 44(2):E14, February 2018.

[60] A Halbach, P Gijsenbergh, Y Jeong, M Billen, C Chare, H Gao, G B Torri, D Cheyns, X Rottenberg, and V Rochus. Modelling of display-compatible piezoelectric micromachined ultrasonic transducers for haptic feedback. *2019 20th International Conference on Thermal, Mechanical and Multi-Physics Simulation and Experiments in Microelectronics and Microsystems, EuroSimE 2019*, 2019. ISBN: 9781538680407 Publisher: IEEE.

[61] Joontaek Jung, Wonjun Lee, Woojin Kang, Eunjung Shin, Jungho Ryu, and Hongsoo Choi. Review of piezoelectric micromachined ultrasonic transducers and their applications. *Journal of Micromechanics and Microengineering*, 27(11), 2017. Publisher: IOP Publishing.

[62] S Sadeghpour, M Kraft, and R Puers. Design and fabrication strategy for an efficient lead zirconate titanate based piezoelectric micromachined ultrasound transducer. *Journal of Micromechanics and Microengineering*, 29(12), 2019. Publisher: IOP Publishing.

[63] Xiaoyue Jiang, Yipeng Lu, Hao Yen Tang, Julius M Tsai, Eldwin J Ng, Michael J Daneman, Bernhard E Boser, and David A Horsley. Monolithic ultrasound fingerprint sensor. *Microsystems and Nanoengineering*, 3(July):1–8, 2017. Publisher: The Author(s).

[64] X. Shi, C. Cheng, and J. Peng. A novel stretchable CMUT array using liquid-metal electrodes on a PDMS substrate. In *2012 7th IEEE International Conference on Nano/Micro Engineered and Molecular Systems (NEMS)*, pages 104–107, 2012.

[65] Wei Liu, Chunling Zhu, and Dawei Wu. Flexible piezoelectric micro ultrasonic transducer array integrated on various flexible substrates. *Sensors and Actuators A: Physical*, 317:112476, 2021.

[66] S. Khan, L. Lorenzelli, and R.S. Dahiya. Technologies for printing sensors and electronics over large flexible substrates: A review. *IEEE Sensors Journal*, 15(6):3164–3185, 2015.

[67] Jose Joseph, Bo Ma, and B. T. Khuri-Yakub. Applications of Capacitive Micromachined Ultrasonic Transducers: A Comprehensive Review. *IEEE Transactions on Ultrasonics, Ferroelectrics, and Frequency Control*, 69(2):456–467, February 2022. Conference Name: IEEE Transactions on Ultrasonics, Ferroelectrics, and Frequency Control.

[68] Albert I-Hsiang Chen, Lawrence L. P. Wong, Shuai Na, Zhenhao Li, Mirek Macecek, and John T. W. Yeow. Fabrication of a Curved Row–Column Addressed Capacitive Micromachined Ultrasonic Transducer Array. *Journal of Microelectromechanical Systems*, 25(4):675–682, August 2016. Conference Name: Journal of Microelectromechanical Systems.

[69] Mahyar Ghavami, Afshin Kashani Ilkhechi, and Roger Zemp. Flexible transparent CMUT arrays for photoacoustic tomography. *Optics Express*, 30(10):15877–15894, May 2022.

[70] M. Chang, H. Deng, D. Pang, and M. Chen. 6F-6 A Novel Method for Fabricating Sonic Paper. In *2007 IEEE Ultrasonics Symposium Proceedings*, pages 527–530, 2007.

[71] C. Cheng, Chen Chao, Xiaomei Shi, and W. W. F. Leung. A flexible capacitive micromachined ultrasonic transducer (CMUT) array with increased effective capacitance from concave bottom electrodes for ultrasonic imaging applications. In *2009 IEEE International Ultrasonics Symposium*, pages 996–999, 2009.

[72] Da-Chen Pang and Cheng-Min Chang. Development of a Novel Transparent Flexible Capacitive Micromachined Ultrasonic Transducer. *Sensors*, 17(6), 2017.

[73] I. Lucarini, L. Maiolo, F. Maita, and A. Savoia. Demonstration of PolyimideBased Flexible CMUT Operation on Curved Substrates. In *2021 IEEE International Ultrasonics Symposium (IUS)*, pages 1–3, 2021.

[74] Chloe Halbach, Jeremy Segers, Veronique Rochus, Epimitheas Georgitzikis, Paul Heremans, and David Cheyns. Fabrication and Characterization of Large-Area Flexible Capacitive Micromachined Ultrasound Transducers. In *2024 IEEE 37th International Conference on Micro Electro Mechanical Systems (MEMS)*, pages 943–946, January 2024. ISSN: 2160-1968.

[75] Benjamin Mimoun, Vincent Henneken, Arjen Van Der Horst, and Ronald Dekker. Flex-to-rigid (F2R): A generic platform for the fabrication and assembly of flexible sensors for minimally invasive instruments. *IEEE Sensors Journal*, 13(10):3873–3882, 2013. Publisher: IEEE.

[76] Guo-Lun Luo, Yuri Kusano, and David A. Horsley. Airborne Piezoelectric Micromachined Ultrasonic Transducers for Long-Range Detection. *Journal of Microelectromechanical Systems*, 30(1):81–89, February 2021. Conference Name: Journal of Microelectromechanical Systems.

[77] Lawrence E. Kinsler, Austin R. Frey, Alan B. Coppens, and James V. Sanders. *Fundamentals of Acoustics*. John Wiley & Sons, January 2000. Google-Books-ID: FecSEAAAQBAJ.

[78] Y. Jeong, J. Genoe, P. Gijsenbergh, J. Segers, P. L. Heremans, and D. Cheyns. Fully Flexible PMUT Based on Polymer Materials and Stress Compensation by Adaptive Frequency Driving. *Journal of Microelectromechanical Systems*, 30(1):137–143, 2021.

[79] W. Liu, X. Li, D. Wu, and T. Yu. Design and Fabrication of Flexible and Transparent Piezoelectric Micromachined Ultrasonic Transducer Based on Mica Substrates. In *2019 IEEE International Ultrasonics Symposium (IUS)*, pages 785–787, 2019.

[80] S. Sun, M. Zhang, C. Gao, B. Liu, and W. Pang. Flexible Piezoelectric Micromachined Ultrasonic Transducers Towards New Applications. In *2018 IEEE International Ultrasonics Symposium (IUS)*, pages 1–4, 2018.

[81] Wei Liu and Dawei Wu. Low Temperature Adhesive Bonding-Based Fabrication of an Air-Borne Flexible Piezoelectric Micromachined Ultrasonic Transducer. *Sensors*, 20(11), 2020.

[82] Zhuocheng Yan, Taisong Pan, Miaomiao Xue, Changyong Chen, Yan Cui, Guang Yao, Long Huang, Feiyi Liao, Wei Jing, Hulin Zhang, Min Gao, Daqing Guo, Yang Xia, and Yuan

Lin. Thermal Release Transfer Printing for Stretchable Conformal Bioelectronics. *Advanced Science*, 4(11):1700251, 2017. _eprint: https://onlinelibrary.wiley.com/doi/pdf/10.1002/advs.201700251.

[83] Xin Chen, Xu Han, and Qun-Dong Shen. PVDF-Based Ferroelectric Polymers in Modern Flexible Electronics. *Advanced Electronic Materials*, 3(5):1600460, 2017. _eprint: https://onlinelibrary.wiley.com/doi/pdf/10.1002/aelm.201600460.

[84] Yongqiang Qiu, James V Gigliotti, Margeaux Wallace, Flavio Griggio, Christine E M Demore, Sandy Cochran, and Susan Trolier-McKinstry. Piezoelectric micromachined ultrasound transducer (PMUT) arrays for integrated sensing, actuation and imaging. *Sensors (Switzerland)*, 15(4):8020–8041, 2015. ISBN: 4413823869.

[85] Yiyin Su, Yiwei Zhang, Xiaohui Yang, Yipeng Lu, Liwei Lin, and Xishan Guo. A Curve-Structured Flexible Pmut with Enhanced Acoustic Sensitivity. In *2024 IEEE 37th International Conference on Micro Electro Mechanical Systems (MEMS)*, pages 939–942, January 2024. ISSN: 2160-1968.

[86] L. C. J. M. Peters, R. Ollearo, R. G. F. A. Verbeek, J. L. P. J. van der Steen, H. B. Akkerman, A. W. F. Volker, P. L. M. J. van Neer, and G. H. Gelinck. Low-cost monolithic processing of large-area ultrasound transducer arrays. In *2019 IEEE International Ultrasonics Symposium (IUS)*, pages 60–63, 2019.

[87] W. Liu, C. Zhu, and D. Wu. Flexible and Stretchable Ultrasonic Transducer Array Conformed to Complex Surfaces. *IEEE Electron Device Letters*, 42(2):240–243, 2021.

[88] Tianning Liu, Margeaux Wallace, Susan Trolier-McKinstry, and Thomas N. Jackson. High-temperature crystallized thin-film PZT on thin polyimide substrates. *Journal of Applied Physics*, 122(16):164103, 2017. _eprint: https://doi.org/10.1063/1.4990052.

[89] Félix Dandois, Orçun Taylan, Johan Bellemans, Jan D'hooge, Hilde Vandenneucker, Laura Slane, and Lennart Scheys. Validated Ultrasound Speckle Tracking Method for Measuring Strains of Knee Collateral Ligaments In-Situ during Varus/Valgus Loading. *Sensors*, 21(5):1895, January 2021. Number: 5 Publisher: Multidisciplinary Digital Publishing Institute.

[90] Sina Sadeghpour, Rui Amendoeira, and Michael Kraft. Ultrasound Imaging With a 128 Channels Piezoelectric Micromachined Ultrasound

Transducer (pMUT): Single-Line-Transmission vs. Plane-Wave. In *2023 IEEE International Ultrasonics Symposium (IUS)*, pages 1–4, September 2023. ISSN: 1948-5727.

[91] David E. Dausch, Kristin H. Gilchrist, James B. Carlson, Stephen D. Hall, John B. Castellucci, and Olaf T. von Ramm. In vivo real-time 3-D intracardiac echo using PMUT arrays. *IEEE Transactions on Ultrasonics, Ferroelectrics, and Frequency Control*, 61(10):1754–1764, October 2014. Conference Name: IEEE Transactions on Ultrasonics, Ferroelectrics, and Frequency Control.

[92] Ziyi Liu, Shinya Yoshida, David A. Horsley, and Shuji Tanaka. Fabrication and characterization of row-column addressed pMUT array with monocrystalline PZT thin film toward creating ultrasonic imager. *Sensors and Actuators A: Physical*, 342:113666, August 2022.

[93] N. Izyumskaya, Y.-I. Alivov, S.-J. Cho, H. Morkoç, H. Lee, and Y.-S. Kang. Processing, Structure, Properties, and Applications of PZT Thin Films. *Critical Reviews in Solid State and Materials Sciences*, 32(3-4):111–202, December 2007. Publisher: Taylor & Francis _eprint: https://doi.org/10.1080/10408430701707347.

[94] J. Gardeniers, A. Verholen, N. Tas, and M. Elwenspoek. Direct measurement of piezoelectric properties of Sol-Gel PZT films. *Journal of The Korean Physical Society - J KOREAN PHYS SOC*, 32, February 1998.

[95] Keith G. Brooks, Ian M. Reaney, Radosveta Klissurska, Y. Huang, L. Bursill, and N. Setter. Orientation of rapid thermally annealed lead zirconate titanate thin films on (111) Pt substrates. *Journal of Materials Research*, 9(10):2540–2553, October 1994.

[96] Cyprien Rusu. Calculating Piezoelectric Material Properties from Material Datasheet. *https://support.onscale.com/hc/en-us/articles/360002073378-Calculating-Piezoelectric-Material-Properties-from-Material-Datasheetbasix*, July 2020.

[97] Marc-Alexandre Dubois and Paul Muralt. Measurement of the effective transverse piezoelectric coefficient e31,f of AlN and Pb(Zrx,Ti1x)O3 thin films. *Sensors and Actuators A: Physical*, 77(2):106–112, October 1999.

[98] P Muralt, A Kholkin, M Kohli, and T Maeder. Piezoelectric actuation of PZT thin-film diaphragms at static and resonant conditions. *Sensors and Actuators A: Physical*, 53(1):398–404, May 1996.

[99] S. Trolier-McKinstry and P. Muralt. Thin Film Piezoelectrics for MEMS. *Journal of Electroceramics*, 12(1):7–17, January 2004.

[100] P. Muralt, N. Ledermann, J. Paborowski, A. Barzegar, S. Gentil, B. Belgacem, S. Petitgrand, A. Bosseboeuf, and N. Setter. Piezoelectric micromachined ultrasonic transducers based on PZT thin films. *IEEE Transactions on Ultrasonics, Ferroelectrics, and Frequency Control*, 52(12):2276–2288, December 2005. Conference Name: IEEE Transactions on Ultrasonics, Ferroelectrics, and Frequency Control.

[101] Aiying Wu, Paula M. Vilarinho, Isabel M. Miranda Salvado, and João L. Baptista. Sol–Gel Preparation of Lead Zirconate Titanate Powders and Ceramics: Effect of Alkoxide Stabilizers and Lead Precursors. *Journal of the American Ceramic Society*, 83(6):1379–1385, 2000. _eprint: https://onlinelibrary.wiley.com/doi/pdf/10.1111/j.1151-2916.2000.tb01397.x.

[102] Guanghua Yi and Michael Sayer. An acetic acid/water based sol-gel PZT process I: Modification of Zr and Ti alkoxides with acetic acid. *Journal of Sol-Gel Science and Technology*, 6(1):65–74, January 1996.

[103] D. Seregin, K. Vorotilov, A. Sigov, and N. Kotova. Porous PZT Films Prepared by PVP Assisted Sol-Gel Process. *Ferroelectrics*, 484(1):43–48, August 2015. Publisher: Taylor & Francis _eprint: https://doi.org/10.1080/00150193.2015.1059680.

[104] Ji Yun Jung, Woo Sik Kim, Hyung-Ho Park, and Tae-Song Kim. The effects of solvent on the properties of sol-gel derived PZT thin films. *Ferroelectrics*, 263(1):327–334, January 2001. Publisher: Taylor & Francis _eprint: https://doi.org/10.1080/00150190108225220.

[105] A. S. Sigov, K. A. Vorotilov, and O. M. Zhigalina. Effect of Lead Content on Microstructure of Sol-Gel PZT Structures. *Ferroelectrics*, 433(1):146–157, January 2012. Publisher: Taylor & Francis _eprint: https://doi.org/10.1080/00150193.2012.696434.

[106] Chang Jung Kim, Dae Sung Yoon, Joon Sung Lee, Chaun Gi Choi, and Kwangsoo No. A Study on the Microstructure of Preferred Orientation of Lead Zirconate Titanate (PZT) Thin Films. *Journal of Materials Research*, 12(4):1043–1047, April 1997.

[107] Haoran Wang, Manish Godara, Zhenfang Chen, and Huikai Xie. A one-step residue-free wet etching process of ceramic PZT for piezoelectric transducers. *Sensors and Actuators A: Physical*, 290:130–136, May 2019.

[108] S. Sivaramakrishnan, P. Mardilovich, A. Mason, A. Roelofs, T. Schmitz-Kempen, and S. Tiedke. Electrode size dependence of piezoelectric response of lead zirconate titanate thin films measured by double beam laser interferometry. *Applied Physics Letters*, 103(13):132904, September 2013.

[109] S. Sivaramakrishnan, P. Mardilovich, T. Schmitz-Kempen, and S. Tiedke. Concurrent wafer-level measurement of longitudinal and transverse effective piezoelectric coefficients (d33,f and e31,f) by double beam laser interferometry. *Journal of Applied Physics*, 123(1):014103, January 2018.

[110] Sanjog Vilas Joshi, Sina Sadeghpour, and Michael Kraft. Polyimide-On-Silicon 2D Piezoelectric Micromachined Ultrasound Transducer (PMUT) Array. *Sensors*, 23(10):4826, January 2023. Number: 10 Publisher: Multidisciplinary Digital Publishing Institute.

[111] Zhihong Wang, Weiguang Zhu, Hong Zhu, Jianmin Miao, Chen Chao, Changlei Zhao, and Ooi Kiang Tan. Fabrication and characterization of piezoelectric micromachined ultrasonic transducers with thick composite PZT films. *IEEE Transactions on Ultrasonics, Ferroelectrics, and Frequency Control*, 52(12):2289–2297, December 2005. Conference Name: IEEE Transactions on Ultrasonics, Ferroelectrics, and Frequency Control.

[112] Flavio Griggio, Christine E. M. Demore, Hyunsoo Kim, James Gigliotti, Yongqiang Qiu, Thomas N. Jackson, Kyusun Choi, Rick L. Tutwiler, Sandy Cochran, and Susan Trolier-McKinstry. Micromachined diaphragm transducers for miniaturised ultrasound arrays. In *2012 IEEE International Ultrasonics Symposium*, pages 1–4, October 2012. ISSN: 1051-0117.

[113] Gökhan Perçin, Abdullah Atalar, F. Levent Degertekin, and Butrus T. Khuri-Yakub. Micromachined two-dimensional array piezoelectrically actuated transducers. *Applied Physics Letters*, 72(11):1397–1399, March 1998.

[114] Takuma Sekiguchi, Shinya Yoshida, Yoshiaki Kanamori, and Shuji Tanaka. Epitaxial Pb(Zr,Ti)O3-Based Piezoelectric Micromachined Ultrasonic Transducer Fabricated on Silicon-On-Nothing (SON) Structure. In *2023 IEEE 36th International Conference on Micro Electro Mechanical Systems (MEMS)*, pages 139–142, January 2023. ISSN: 2160-1968.

[115] Eunjung Shin, Hong Goo Yeo, Ara Yeon, Changzhu Jin, Wonki Park, Sung-Chul Lee, and Hongsoo Choi. Development of a High-Density Piezoelectric Micromachined Ultrasonic Transducer Array Based on Patterned Aluminum Nitride Thin Film. *Micromachines*, 11(6):623, June 2020. Number: 6 Publisher: Multidisciplinary Digital Publishing Institute.

[116] Junxiang Cai, Yiyun Wang, Daohuai Jiang, Songsong Zhang, Yuandong Alex Gu, Liang Lou, Fei Gao, and Tao Wu. Beyond fundamental resonance mode: high-order multi-band ALN PMUT for in vivo photoacoustic imaging. *Microsystems & Nanoengineering*, 8(1):1–12, November 2022. Publisher: Nature Publishing Group.

[117] Hongjie Hu, Hao Huang, Mohan Li, Xiaoxiang Gao, Lu Yin, Ruixiang Qi, Ray S. Wu, Xiangjun Chen, Yuxiang Ma, Keren Shi, Chenghai Li, Timothy M. Maus, Brady Huang, Chengchangfeng Lu, Muyang Lin, Sai Zhou, Zhiyuan Lou, Yue Gu, Yimu Chen, Yusheng Lei, Xinyu Wang, Ruotao Wang, Wentong Yue, Xinyi Yang, Yizhou Bian, Jing Mu, Geonho Park, Shu Xiang, Shengqiang Cai, Paul W. Corey, Joseph Wang, and Sheng Xu. A wearable cardiac ultrasound imager. *Nature*, 613(7945):667–675, January 2023. Number: 7945 Publisher: Nature Publishing Group.

[118] Craig K. Abbey, Nghia Q. Nguyen, and Michael F. Insana. Effects of frequency and bandwidth on diagnostic information transfer in ultrasonic B-Mode imaging. *IEEE Transactions on Ultrasonics, Ferroelectrics, and Frequency Control*, 59(6):1115–1126, June 2012. Conference Name: IEEE Transactions on Ultrasonics, Ferroelectrics, and Frequency Control.

[119] Sanjog V. Joshi, Sina Sadeghpour, and Michael Kraft. Bendable Polymer-Based High-Frequency pMUTs on Transparent SU8 and Polyimide Substrates. In *2023 22nd International Conference on Solid-State Sensors, Actuators and Microsystems (Transducers)*, pages 849–852, June 2023. ISSN: 2167-0021.

[120] Guo-Lun Luo, Stephanie Fung, Qi Wang, Yuri Kusano, Jon Lasiter, Donald Kidwell, and David A. Horsley. High fill factor piezoelectric micromachined ultrasonic transducers on transparent substrates. In *2017 19th International Conference on Solid-State Sensors, Actuators and Microsystems (TRANSDUCERS)*, pages 1053–1056, June 2017. ISSN: 2167-0021.

[121] Donghwan Koo, Sungwoo Jung, Jihyung Seo, Gyujeong Jeong, Yunseong Choi, Junghyun Lee, Sang Myeon Lee, Yongjoon Cho, Mingyu Jeong, Jungho Lee, Jiyeon Oh, Changduk Yang, and Hyesung Park. Flexible Organic Solar Cells Over 15% Efficiency with Polyimide-Integrated Graphene Electrodes. *Joule*, 4(5):1021–1034, May 2020.

[122] Rik J. J. van Daal, Jyh-Jang Sun, Frederik Ceyssens, Frédéric Michon, Michael Kraft, Robert Puers, and Fabian Kloosterman. System for recording from multiple flexible polyimide neural probes in freely behaving animals. *Journal of Neural Engineering*, 17(1):016046, February 2020. Publisher: IOP Publishing.

[123] Tianning Liu, Ajay Dangi, Jeong Nyeon Kim, Sri-Rajasekhar Kothapalli, Kyusun Choi, Susan Trolier-McKinstry, and Thomas Jackson. Flexible Thin-Film PZT Ultrasonic Transducers on Polyimide Substrates. *Sensors*, 21(3), 2021.

[124] Patrick Abgrall, Veronique Conedera, Henri Camon, Anne-Marie Gue, and Nam-Trung Nguyen. SU-8 as a structural material for labs-on-chips and microelectromechanical systems. *Electrophoresis*, 28:4539–51, December 2007.

[125] Frederik Ceyssens and Robert Puers. SU-8 Photoresist. In Bharat Bhushan, editor, *Encyclopedia of Nanotechnology*, pages 2530–2543. Springer Netherlands, Dordrecht, 2012.

[126] Carlos D. Gerardo, Edmond Cretu, and Robert Rohling. Fabrication and testing of polymer-based capacitive micromachined ultrasound transducers for medical imaging. *Microsystems & Nanoengineering*, 4(1):1–12, August 2018. Publisher: Nature Publishing Group.

[127] Soonwan Chung and Seungbae Park. Effects of temperature on mechanical properties of SU-8 photoresist material. *Journal of Mechanical Science and Technology*, 27(9):2701–2707, September 2013.

[128] PI-2600 Series- Low Stress Applications, Product Bulletin, HD Microsystems, https://www.yumpu.com/fr/document/read/2032698/pi-2600-series-low-stress-applications-hd-microsystems.

[129] SU-8 2000 Permanent Negative Epoxy Photoresist, https://kayakuam.com/wp-content/uploads/2022/04/KAM-SU-8-2000-2025-2100-Datasheet-4.9.21-final.pdf.

[130] Sanjog Vilas Joshi, Sina Sadeghpour, and Michael Kraft. A 50x20 Row-Column Addressed PMUT Array on Silicon Substrate for Imaging. In *2023 IEEE International Ultrasonics Symposium (IUS)*, pages 1–4, September 2023. ISSN: 1948-5727.

[131] Qinghua Huang and Zhaozheng Zeng. A Review on Real-Time 3D Ultrasound Imaging Technology. *BioMed Research International*, 2017(1):6027029, 2017. _eprint: https://onlinelibrary.wiley.com/doi/pdf/10.1155/2017/6027029.

[132] Piezoelectric Tonpilz Transducer, https://www.comsol.com/model/piezoelectric-tonpilz-transducer-11478.

[133] Sanjog Vilas Joshi, Sina Sadeghpour, and Michael Kraft. Flexible PZT-Based Row-Column Addressed 2-D PMUT Array. *IEEE Transactions*

on Ultrasonics, Ferroelectrics, and Frequency Control, 71(11):1616–1626, November 2024. Conference Name: IEEE Transactions on Ultrasonics, Ferroelectrics, and Frequency Control.

[134] Kaustav Roy, Sumit Agrawal, Ajay Dangi, Tianning Liu, Haoyang Chen, Thomas N. Jackson, Rudra Pratap, and Sri-Rajasekhar Kothapalli. Body Conformal Linear Ultrasound Array for Combined Ultrasound and Photoacoustic Imaging. In *2020 IEEE International Ultrasonics Symposium (IUS)*, pages 1–4, September 2020. ISSN: 1948-5727.

[135] Sanjog Vilas Joshi, Sina Sadeghpour, Rui Amendoeira Esteves, Chen Wang, and Michael Kraft. Imaging with a Row-Column (RC) Addressed PMUT Array. In *2024 IEEE Ultrasonics, Ferroelectrics, and Frequency Control Joint Symposium (UFFC-JS)*, pages 1–4, September 2024. ISSN: 2375-0448.

[136] Jørgen Arendt Jensen, Mikkel Schou, Lasse Thurmann Jørgensen, Borislav G. Tomov, Matthias Bo Stuart, Marie Sand Traberg, Iman Taghavi, Sigrid Huesebø Øygaard, Martin Lind Ommen, Kitty Steenberg, Erik Vilain Thomsen, Nathalie Sarup Panduro, Michael Bachmann Nielsen, and Charlotte Mehlin Sørensen. Anatomic and Functional Imaging Using Row–Column Arrays. *IEEE Transactions on Ultrasonics, Ferroelectrics, and Frequency Control*, 69(10):2722–2738, October 2022. Conference Name: IEEE Transactions on Ultrasonics, Ferroelectrics, and Frequency Control.

[137] W. A. Hamidzada and E. P. Osuobeni. Agreement between A-mode and B-mode ultrasonography in the measurement of ocular distances. *Veterinary Radiology & Ultrasound: The Official Journal of the American College of Veterinary Radiology and the International Veterinary Radiology Association*, 40(5):502–507, 1999.

[138] Anatoly Fedorov Kukk, Felix Scheling, Rüdiger Panzer, Steffen Emmert, and Bernhard Roth. Combined ultrasound and photoacoustic C-mode imaging system for skin lesion assessment. *Scientific Reports*, 13(1):17947, October 2023. Publisher: Nature Publishing Group.

[139] Giulia Matrone, Alessandro Ramalli, and Piero Tortoli, editors. *Ultrasound B-mode Imaging: Beamforming and Image Formation Techniques*. MDPI - Multidisciplinary Digital Publishing Institute, September 2019.

[140] Ultrasound imaging. In Paul Suetens, editor, *Fundamentals of Medical Imaging*, pages 128–158. Cambridge University Press, Cambridge, 2 edition, 2009.

[141] Steven Hammer. *Engineering a 3D ultrasound system for image-guided vascular modelling*. PhD thesis, January 2009.

[142] Multi-Purpose Multi-Tissue Ultrasound Phantom, https://www.cirsinc.com/products/ultrasound/zerdine-hydrogel/multi-purpose-multi-tisse-ultrasound-phantom/.

[143] Ziyi Liu, Shinya Yoshida, Toshiaki Horie, Shoji Okamoto, Ryoichi Takayama, and Shuji Tanaka. Feasibility study of ultrasonic biometrics based on finger vessel imaging by epitaxial-PZT/Si piezoelectric micromachined ultrasonic transducer. *Sensors and Actuators A: Physical*, 312:112145, September 2020.

[144] Alessandro S. Savoia, Marco Casavola, Enrico Boni, Marco Ferrera, Carlo Prelini, Piero Tortoli, Domenico Giusti, and Fabio Quaglia. Design, Fabrication, Characterization, and System Integration of a 1-D PMUT Array for Medical Ultrasound Imaging. In *2021 IEEE International Ultrasonics Symposium (IUS)*, pages 1–3, September 2021. ISSN: 1948-5727.

[145] Sebastian Wiegand, Stefan Flege, Olaf Baake, and Wolfgang Ensinger. Effect of different calcination temperatures and post annealing on the properties of 1,3 propanediol based Sol–Gel (Na0.5K0.5)NbO3 (NKN) thin films. *Journal of Alloys and Compounds*, 548:38–45, January 2013.

List of Publications

Journal articles

Joshi, S.V., Sadeghpour, S., Kraft, M. (2023). Low-cost piezo-MEMS speaker technology. MICRO AND NANO ENGINEERING, 19, Art.No. ARTN 100213. doi: 10.1016/j.mne.2023.100213

Joshi, S.V., Sadeghpour, S., Kraft, M. (2023). Polyimide-On-Silicon 2D Piezoelectric Micromachined Ultrasound Transducer (PMUT) Array. SENSORS, 23 (10), Art.No. ARTN 4826. doi: 10.3390/s23104826

Sadeghpour Shamsabadi, S., Vilas Joshi, S., Wang, C., Kraft, M. (2022). Novel phased array piezoelectric micromachined ultrasound transducers (PMUTs) for medical imaging. IEEE Transactions On Ultrasonics Ferroelectrics And Frequency Control, 2, 194-202. doi: 10.1109/OJUFFC.2022.3207128.

Sanjog Vilas Joshi, Sina Sadeghpor, Nadia Kuznetzova, Chen Wang, and Michael Kraft. Flexible micromachined ultrasound transducer (MUTs) for biomedical applications. Microsyst Nanoeng 11, 9 (2025).

Sanjog Vilas Joshi, Sina Sadeghpor, and Michael Kraft. Flexible PZT-based Row-Column Addressed 2D PMUT Array. IEEE TUFFC, vol. 71, no. 11, pp. 1616-1626, Nov.2024.

Conference proceedings

Joshi, S.V., Sadeghpour, S., Kraft, M. with Joshi, S.V. (corresp. author) (2023). Fabrication of high-frequency 2D flexible pMUT array. Presented at the 36th IEEE International Conference on Micro Electro Mechanical Systems (MEMS),

GERMANY, Munich, 15 Jan 2023-19 Jan 2023. ISBN: 978-1-6654-9308-6. page 331-334. doi: 10.1109/MEMS49605.2023.10052246

Joshi, S.V., Sadeghpour, S., Kraft, M. (2023). A 50x20 Row-Column Addressed PMUT Array on Silicon Substrate for Imaging. In: 2023 IEEE International Ultrasonics Symposium (IUS), (1-4). Presented at the 2023 IEEE International Ultrasonics Symposium (IUS), Montreal, Canada. ISBN: 979-8-3503-4645-9. doi: 10.1109/IUS51837.2023.10307994

Joshi, S.V., Sadeghpour, S., Kraft, M. (2023). Bendable Polymer-Based High-Frequency pMUTs on Transparent SU8 and Polyimide Substrates. In: Technical Digest, Solid-State Sensors, Actuators and Microsystems. Transducers 2023, proceedings.

Guan, Y.; Torunbalci, M.M.; Joshi, S.V.; Sadeghpour, S.; Quan, A.; Wang, C.; Kraft, M. A Simple Method for Extracting Piezoelectric Coefficient d31 by Fitting Experimental Data with an Analytical Model. Proceedings 2024, 97, 202. https://doi.org/10.3390/proceedings2024097202

Joshi, S.V., Sadeghpour, S., Kraft, M. (2023). Imaging with a Row-Column (RC) Addressed PMUT Array, IEEE UFFC-JS 2024 proceedings.

...



FACULTY OF ENGINEERING SCIENCE
DEPARTMENT OF ELECTRICAL ENGINEERING
ESAT-MNS
Celestijnenlaan 200A box 2402
B-3001 Leuven
sanjogvilas.joshi@kuleuven.be
https://www.kuleuven.be/wieiswie/nl/person/00143201